Science Advances
AAAS

Supplementary Materials for

Ir-Sn pair-site triggers key oxygen radical intermediate for efficient acidic water oxidation

Xiaobo Zheng *et al.*

Corresponding author: Wenping Sun, wenpingsun@zju.edu.cn;
Dingsheng Wang, wangdingsheng@mail.tsinghua.edu.cn; Yadong Li, ydli@mail.tsinghua.edu.cn

Sci. Adv. **9**, eadi8025 (2023)
DOI: 10.1126/sciadv.adi8025

This PDF file includes:

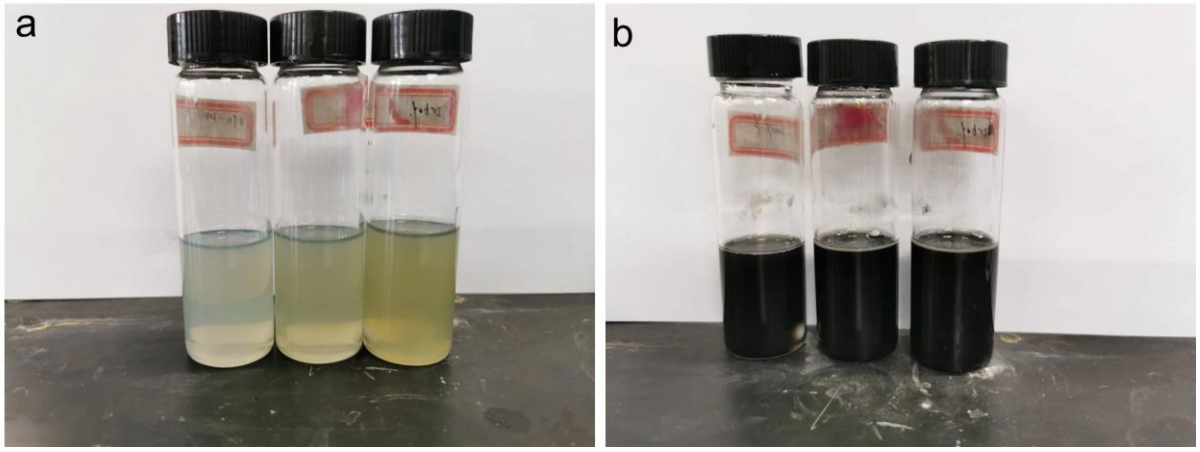

Fig. S1. Digital images of different types of Ir-Sn PSC dispersed in ethylene glycol (EG). (a) before and (b) after reduction. They are 10.2% Ir-Sn PSC, 23.2% Ir-Sn PSC, and 38.3% Ir-Sn PSC from left to right, respectively.

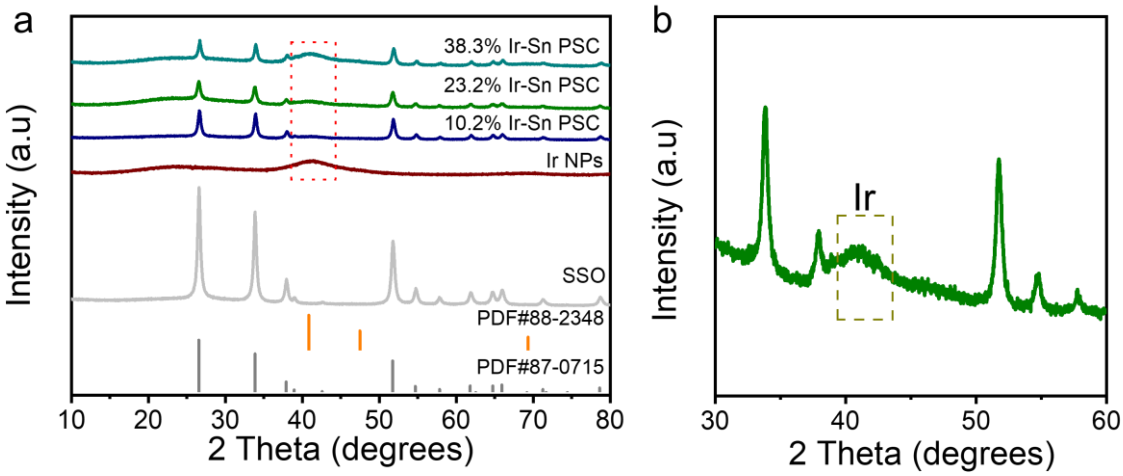

Fig. S2. XRD patterns of all catalysts. (a) XRD patterns of SSO, Ir NPs, 10.2 % Ir-Sn PSC, 23.2 % Ir-Sn PSC, and 38.3 % Ir-Sn PSC. (b) Magnified XRD pattern of 23.2% Ir-Sn PSC.

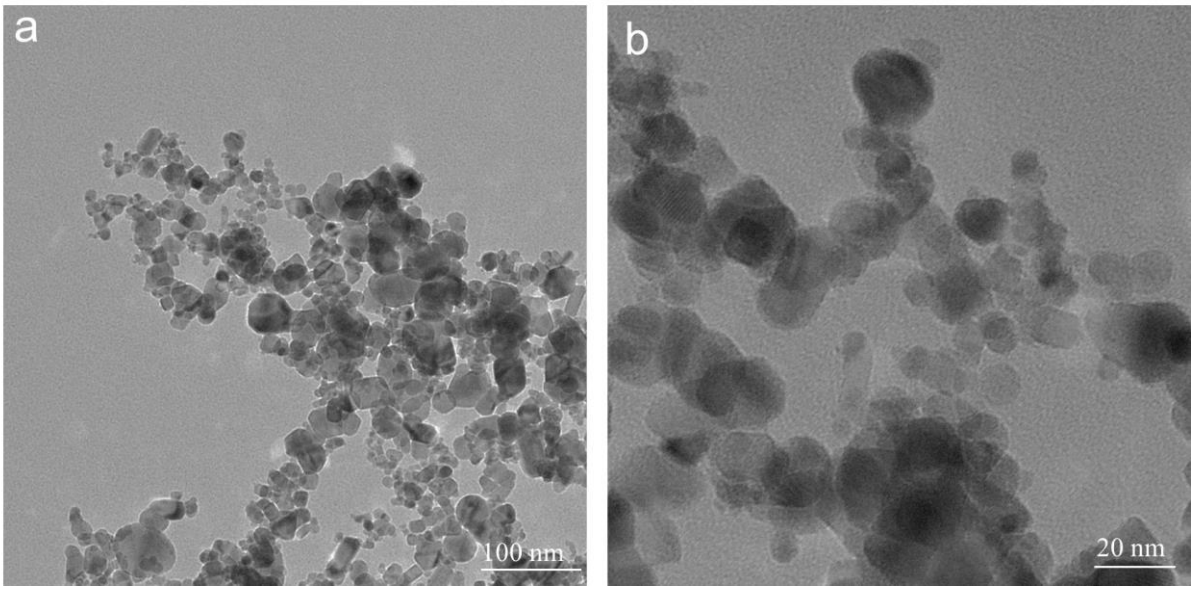

Fig. S3. TEM images. (a-b) TEM images of the SSO at different magnifications.

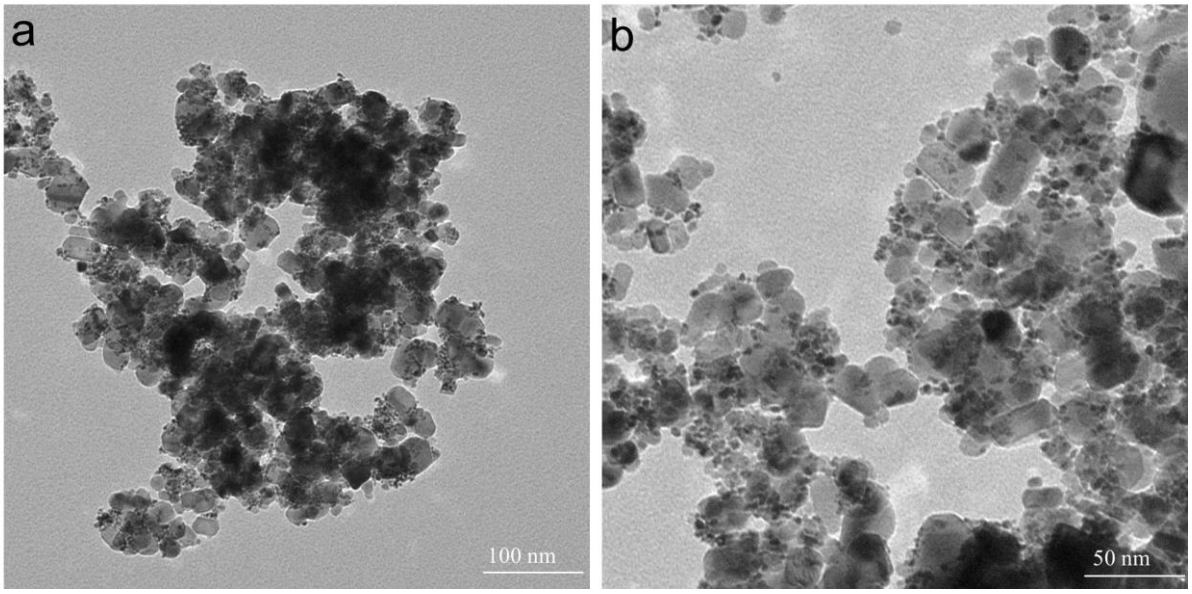

Fig. S4. TEM images. (a-b) TEM images of 10.2 % Ir-Sn PSC at different magnifications.

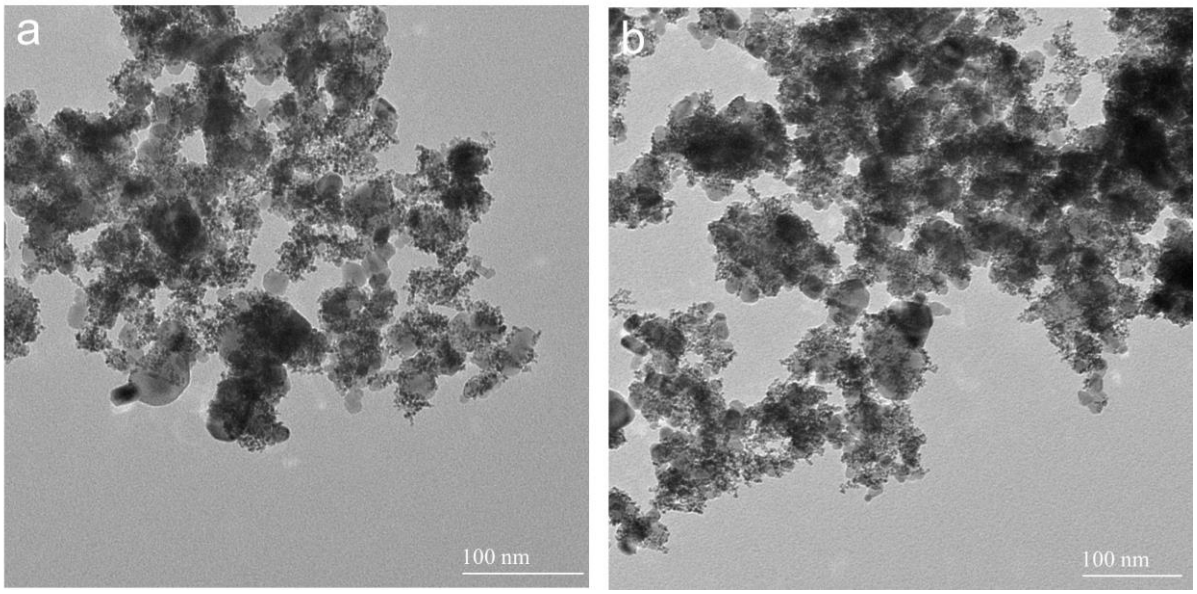

Fig. S5. TEM images. (a-b) TEM images of 23.2% Ir-Sn PSC.

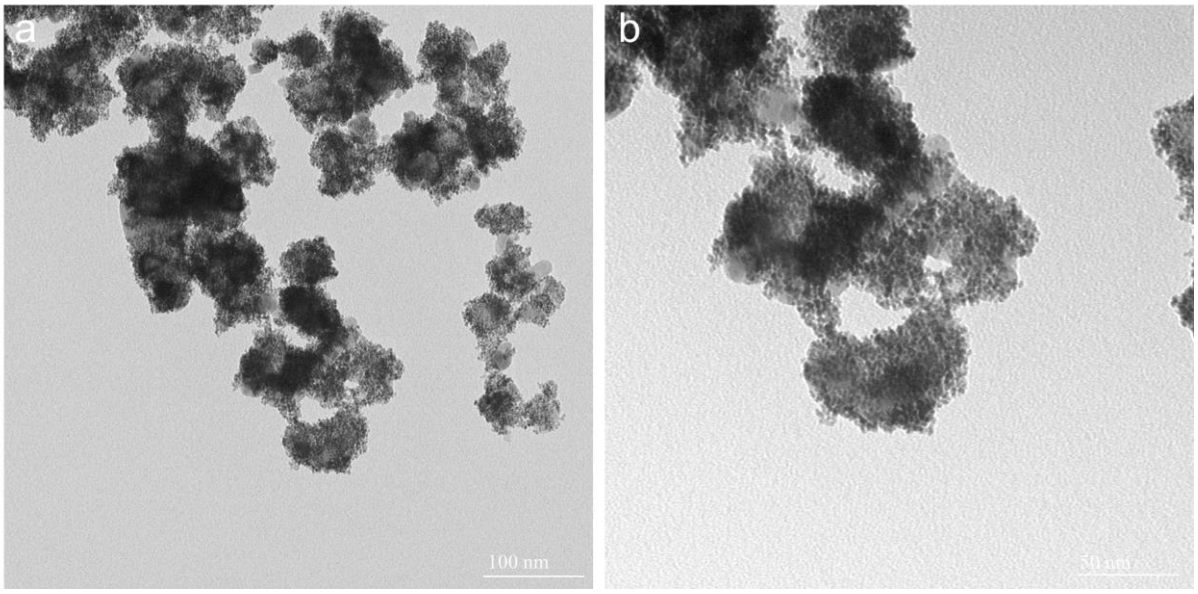

Fig. S6. TEM images. (a-b) TEM images of 38.3% Ir-Sn PSC.

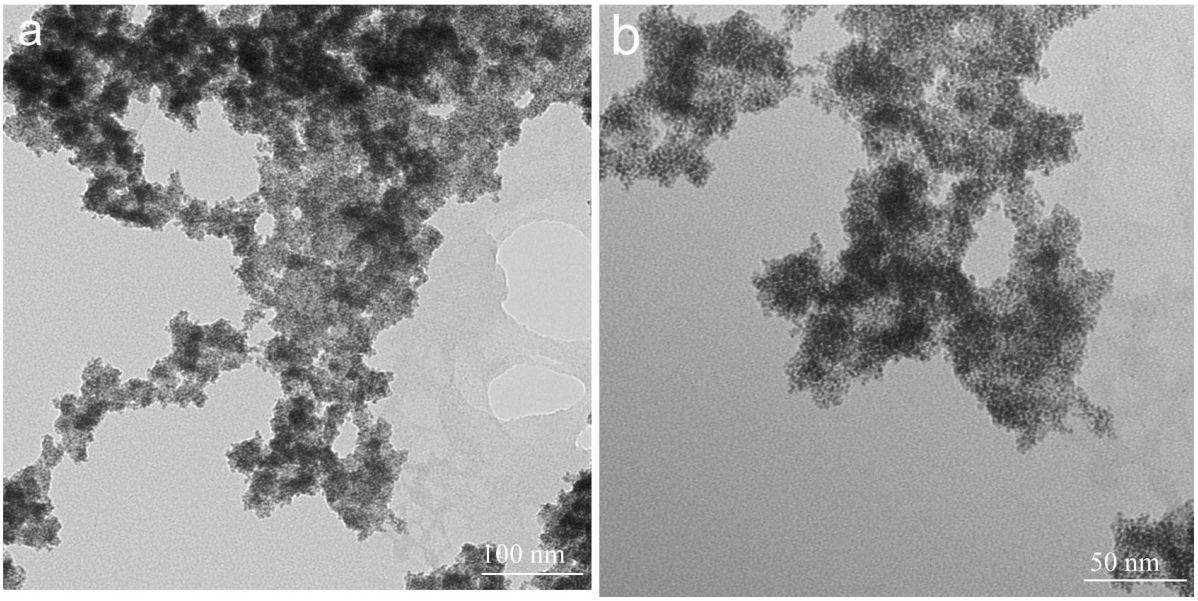

Fig. S7. TEM images. (a-b) TEM images of Ir NPs at different magnifications.

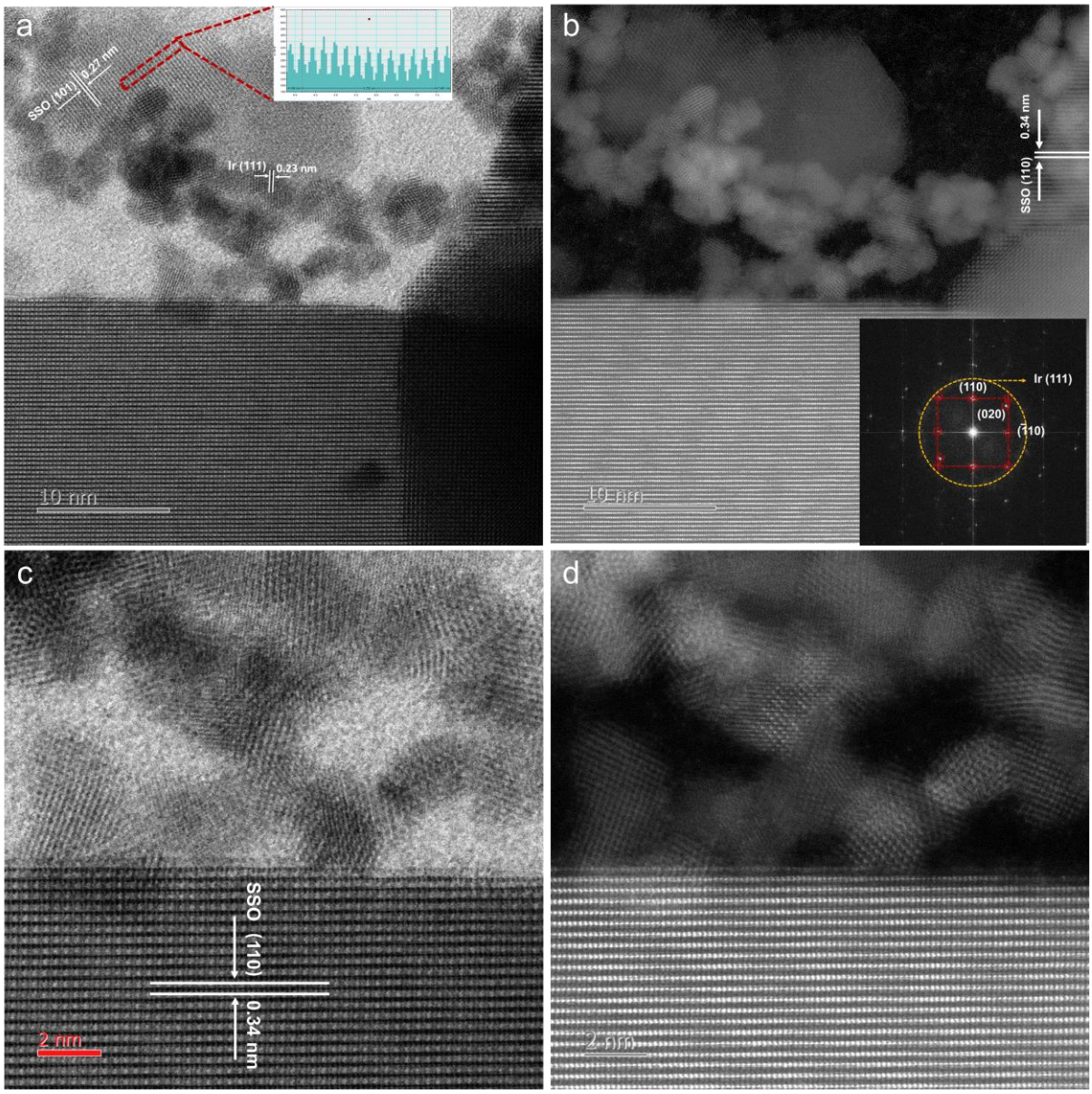

Fig. S8. ABF-STEM and HAADF-STEM images of Ir-Sn PSC. (a) and (c) ABF-STEM images of Ir-Sn PSC. (b) and (d) HAADF-STEM images of Ir-Sn PSC, with the corresponding FFT pattern in the inset of (b).

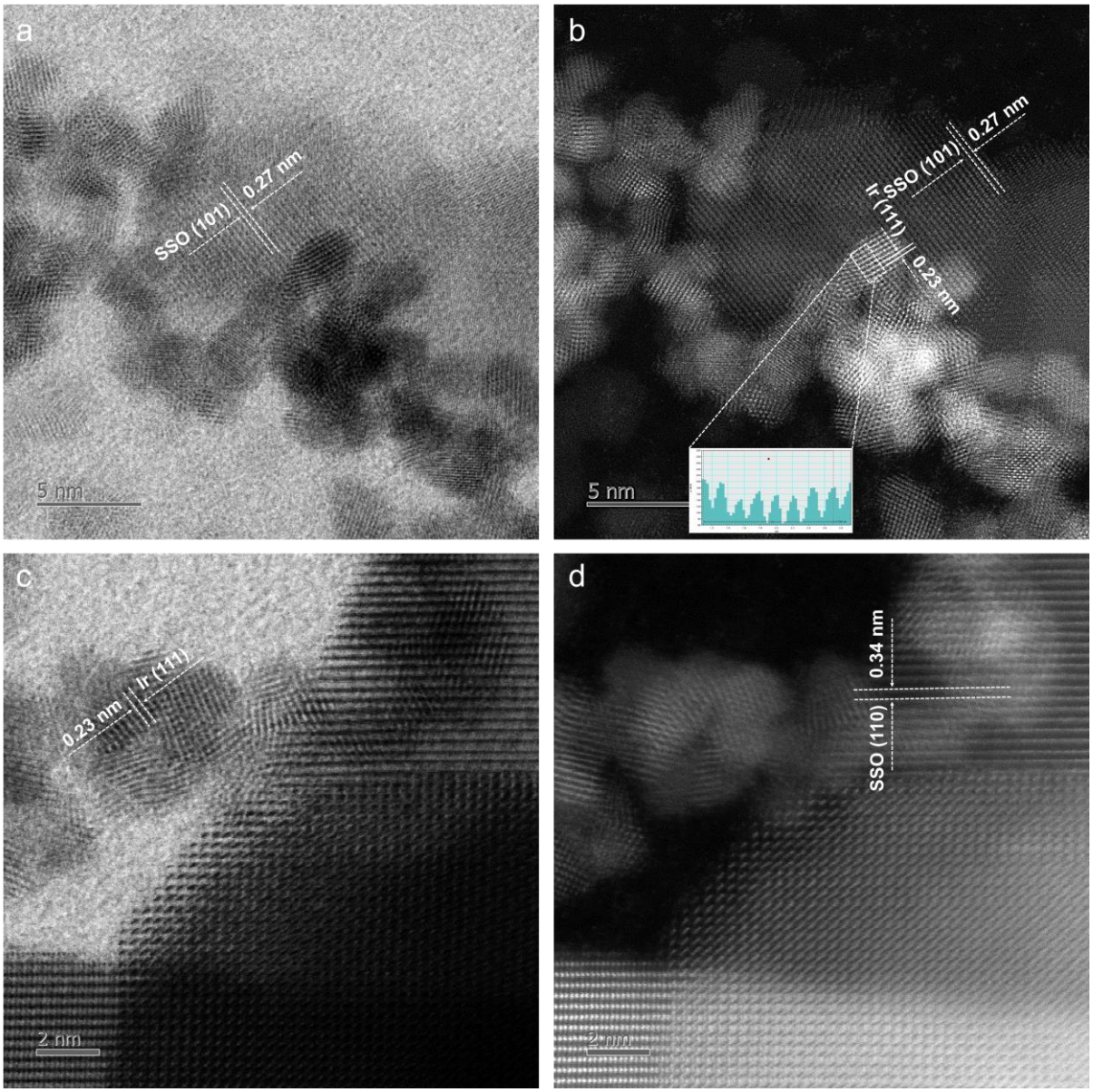

Fig. S9. ABF-STEM and HAADF-STEM images of Ir-Sn PSC. (a) and (c) ABF-STEM images of Ir-Sn PSC. (b) and (d) HAADF-STEM images of Ir-Sn PSC.

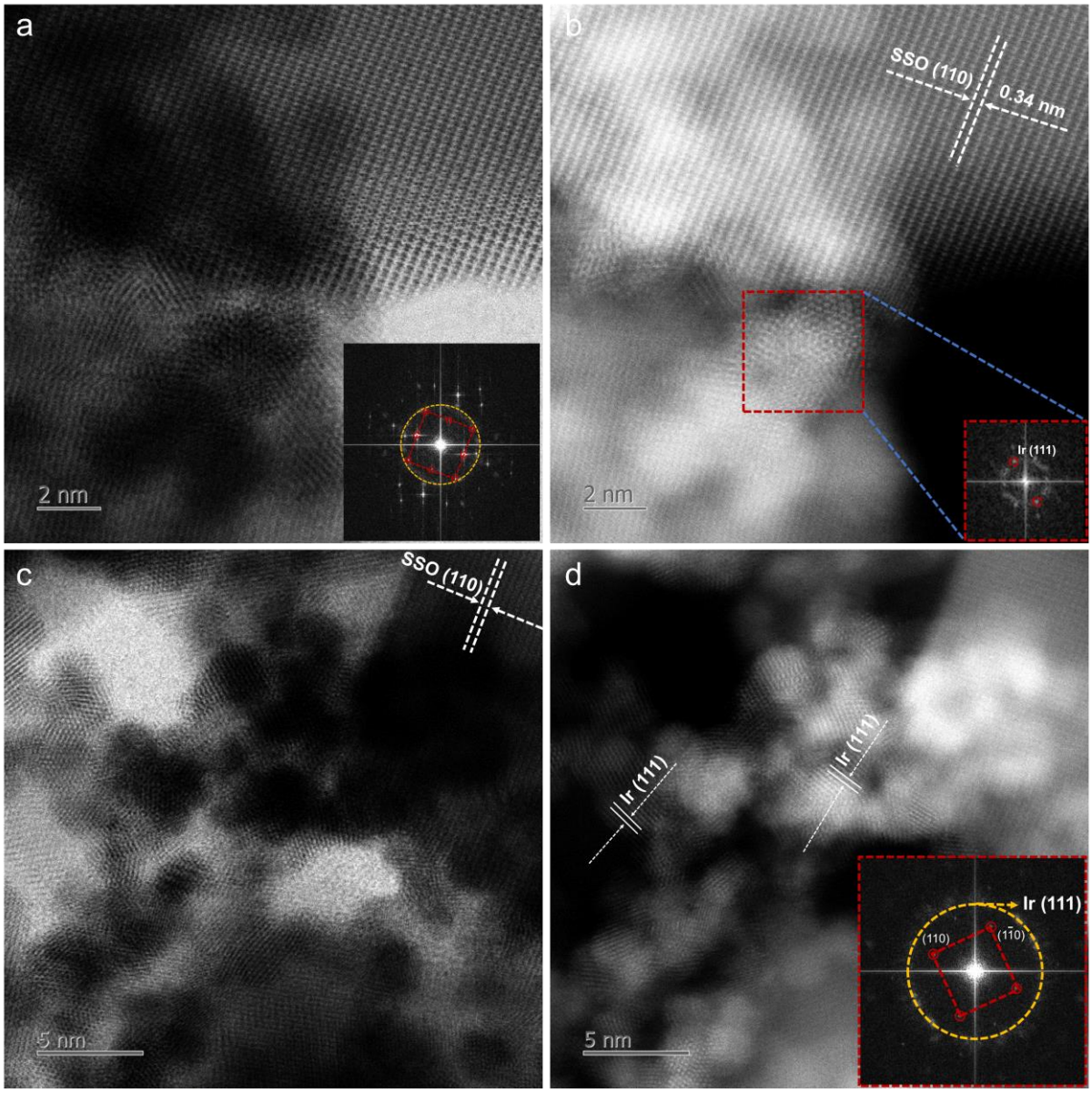

Fig. S10. ABF-STEM and HAADF-STEM images of Ir-Sn PSC. (a) and (c) ABF-STEM images of Ir-Sn PSC. (b) and (d) HAADF-STEM images of Ir-Sn PSC, with the insets showing the corresponding FFT patterns.

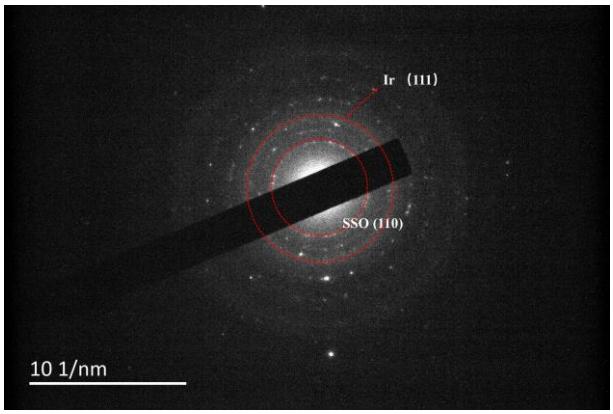

Fig. S11. SAED pattern of Ir-Sn PSC.

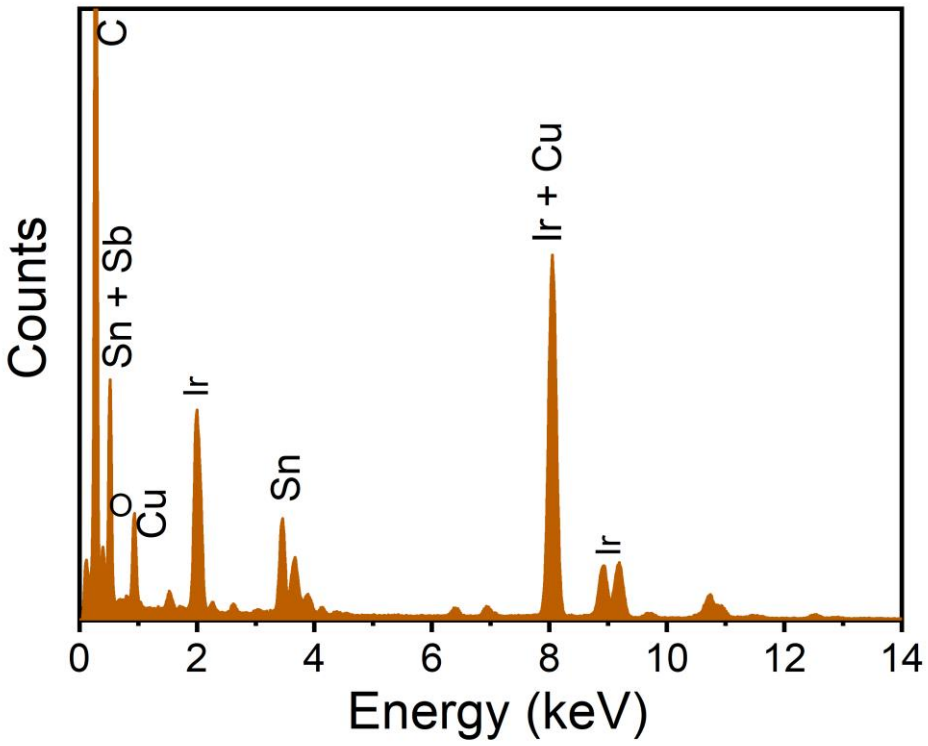

Fig. S12. EDS spectrum of Ir-Sn PSC.

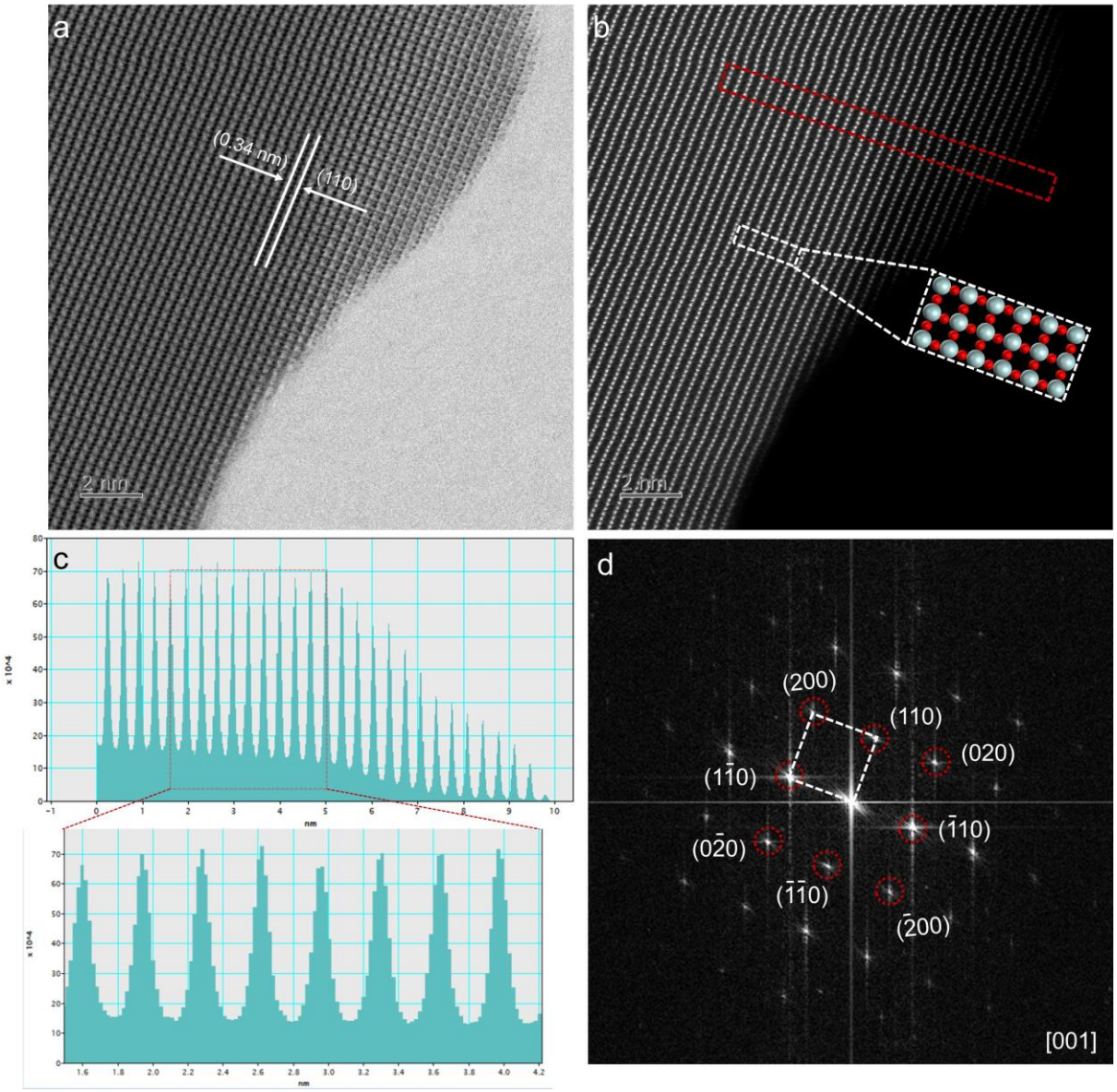

Fig. S13. ABF-STEM and HAADF-STEM images of SSO along with the corresponding FFT pattern. (a) ABF-STEM and (b) HAADF-STEM images of SSO. (c) Intensity profiles of the area marked by the red rectangle (b). (d) The corresponding FFT pattern.

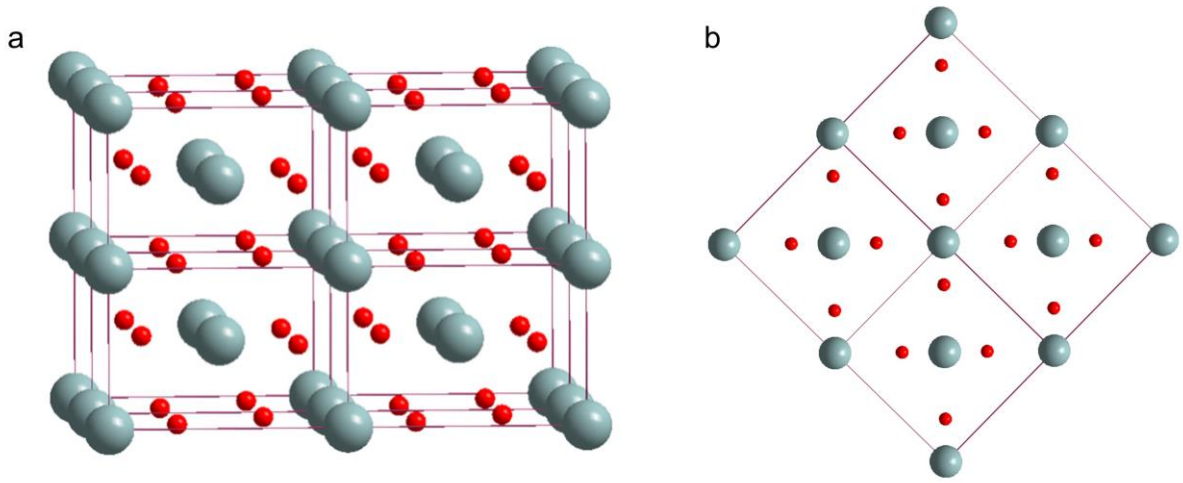

Fig. S14. Crystal structure of SSO. (a) Crystal structure of SSO and (b) the crystal structure viewed from the [001] direction. Red balls represent the oxygen atoms and gray balls the Sn and Sb atoms.

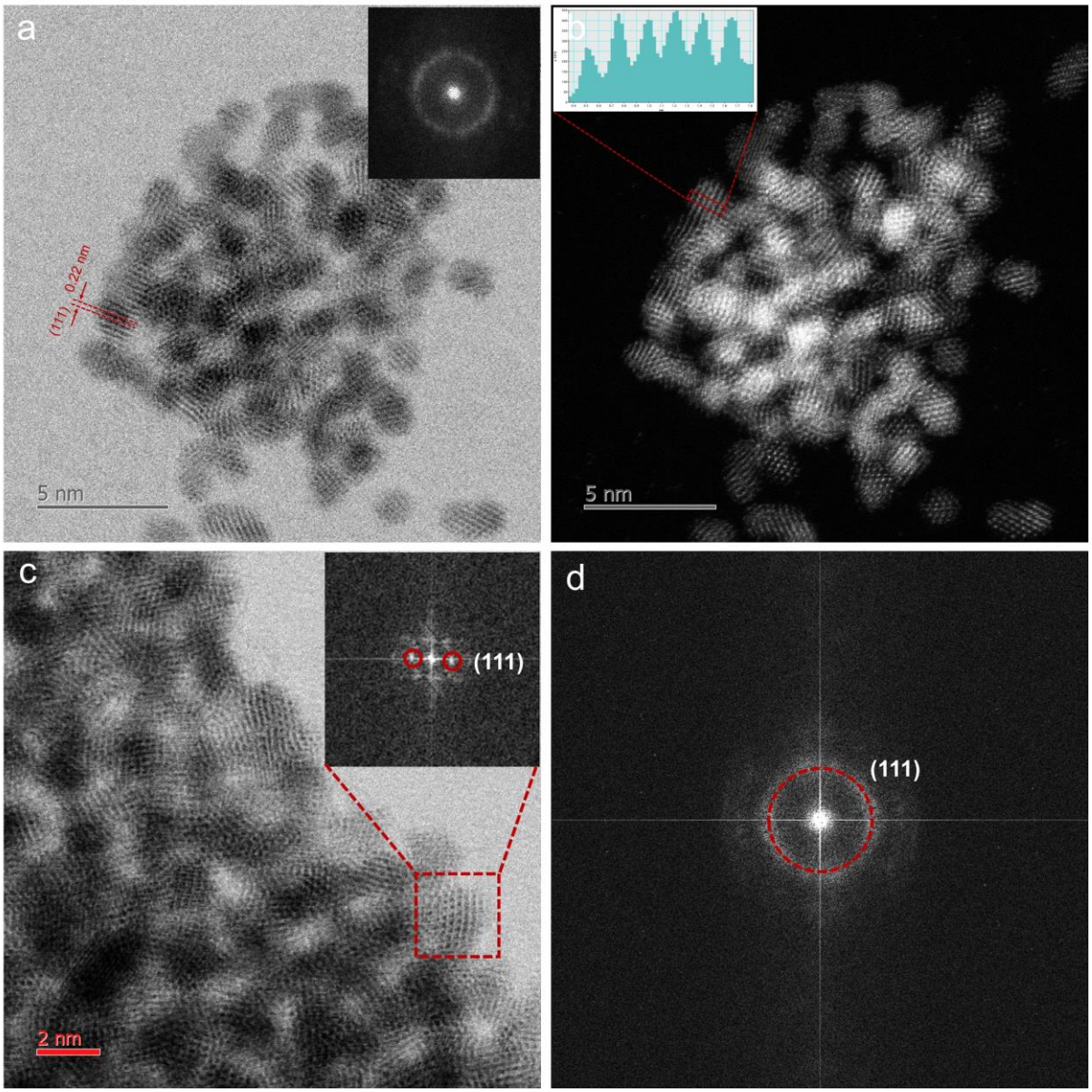

Fig. S15. ABF-STEM and HAADF-STEM images of Ir NPs along with the corresponding FFT pattern. (a) ABF-STEM and (b) HAADF-STEM images of Ir NPs. (c) ABF-STEM image and (d) the corresponding FFT pattern. The presence of characteristic (111) lattice planes suggests the successful synthesis of the cubic phase of Ir (Fm-3M).

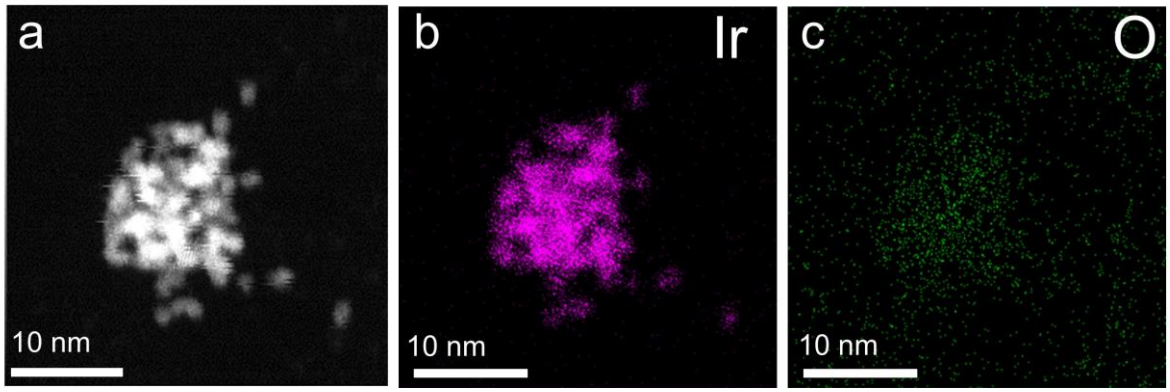

Fig. S16. EDS mapping of Ir and O in Ir NPs.

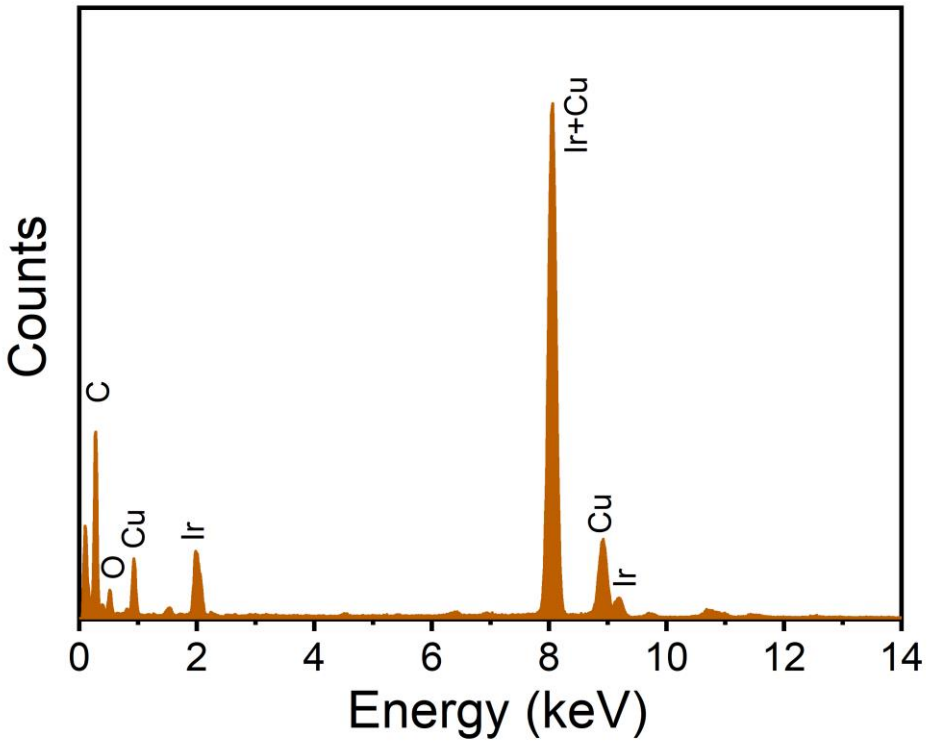

Fig. S17. EDS spectrum of Ir NPs.

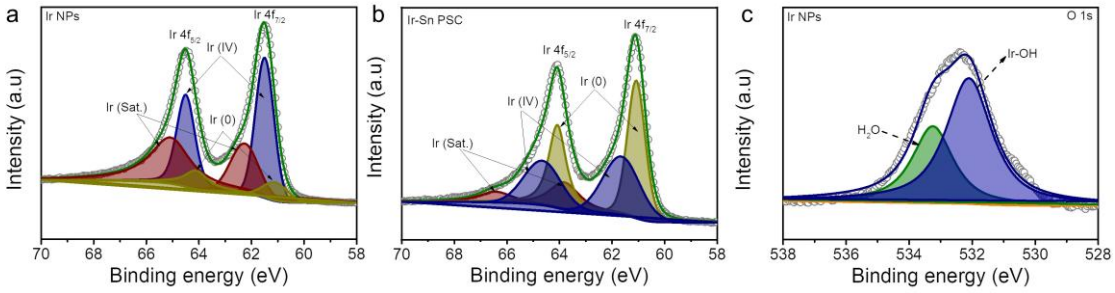

Fig. S18. High-resolution Ir 4f and O1s XPS spectra for Ir-Sn PSC and Ir NPs. High-resolution Ir 4f XPS spectra for (a) Ir NPs and (b) Ir-Sn PSC, and (c) O 1s XPS spectrum for Ir NPs.

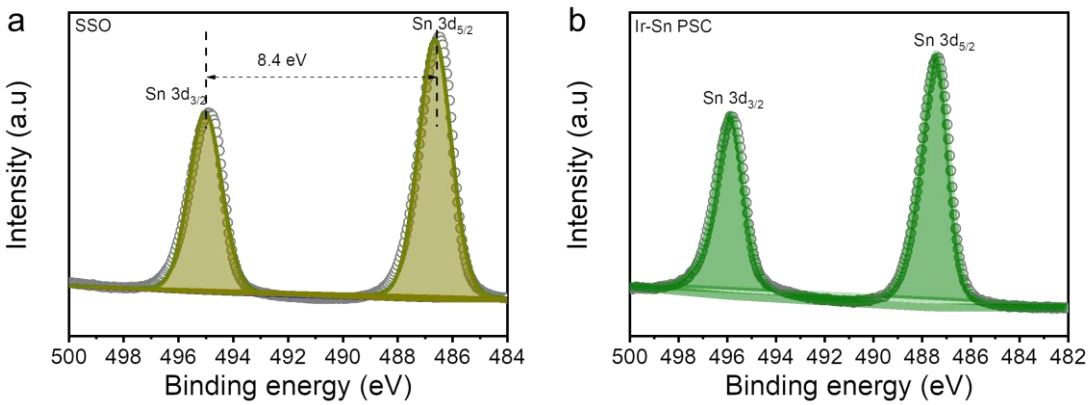

Fig. S19. High-resolution Sn 3d XPS spectra. (a) SSO. (b) Ir-Sn PSC.

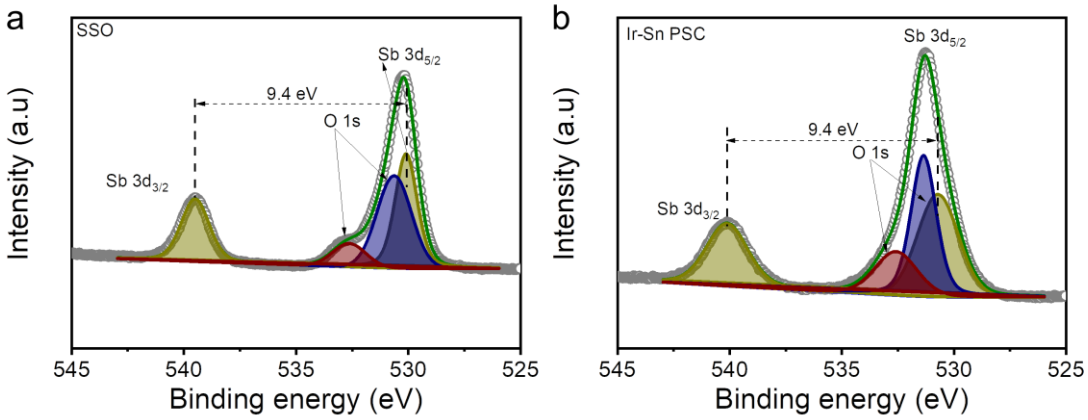

Fig. S20. High-resolution Sb 3d + O 1s XPS spectra. (a) SSO. (b) Ir-Sn PSC.

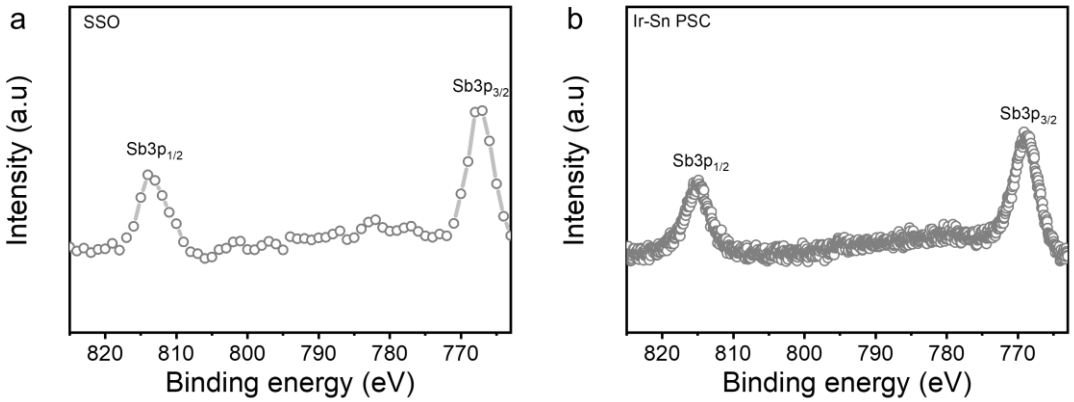

Fig. S21. High-resolution Sb 3p XPS spectra. (a) SSO. (b) Ir-Sn PSC.

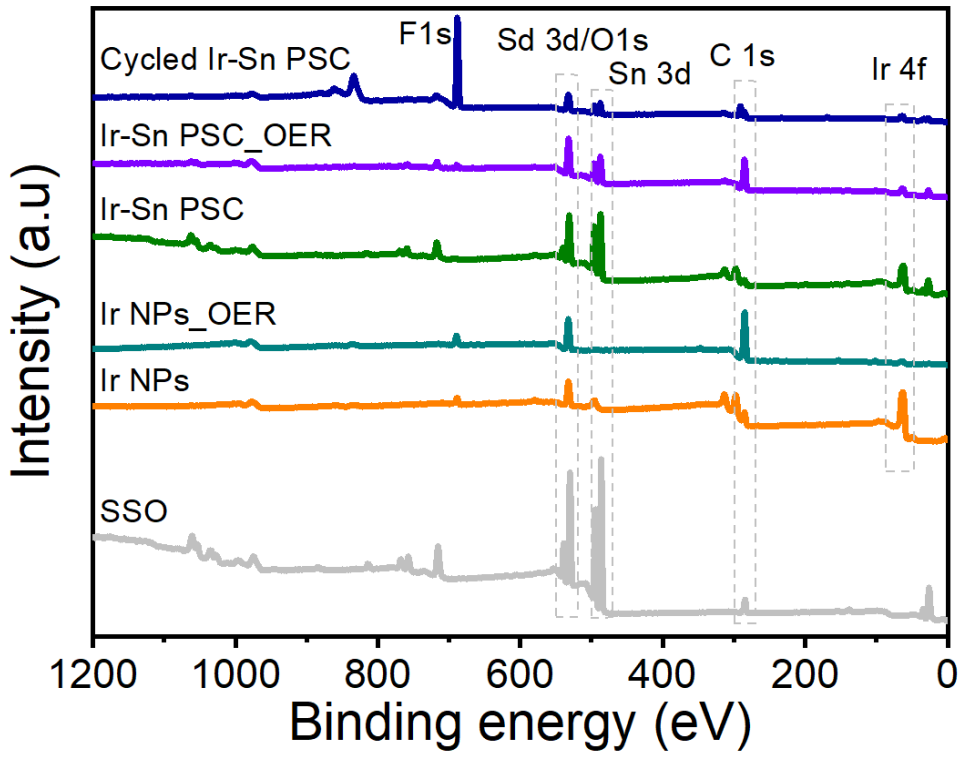

Fig. S22. Survey spectra of SSO, Ir NPs, Ir-Sn PSC, Ir NPs_OER, Ir-Sn PSC_OER, and cycled Ir-Sn PSC.

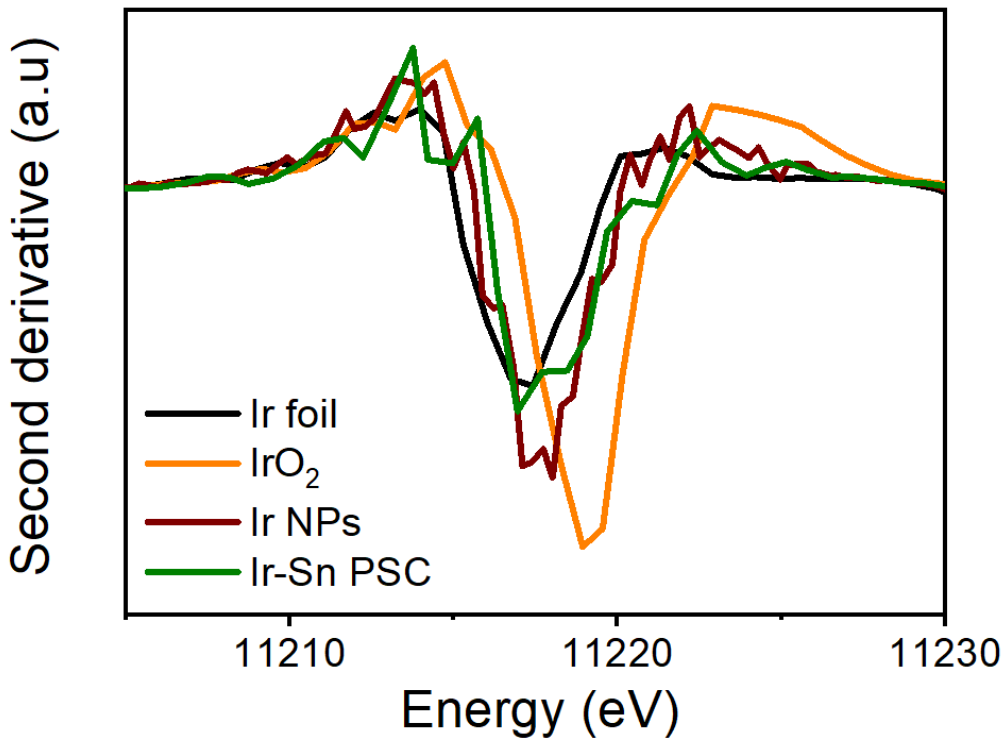

Fig. S23. The second derivative of the Ir L_3-edge XANES spectra for Ir NPs, Ir-Sn PSC, IrO_2, and Ir foil.

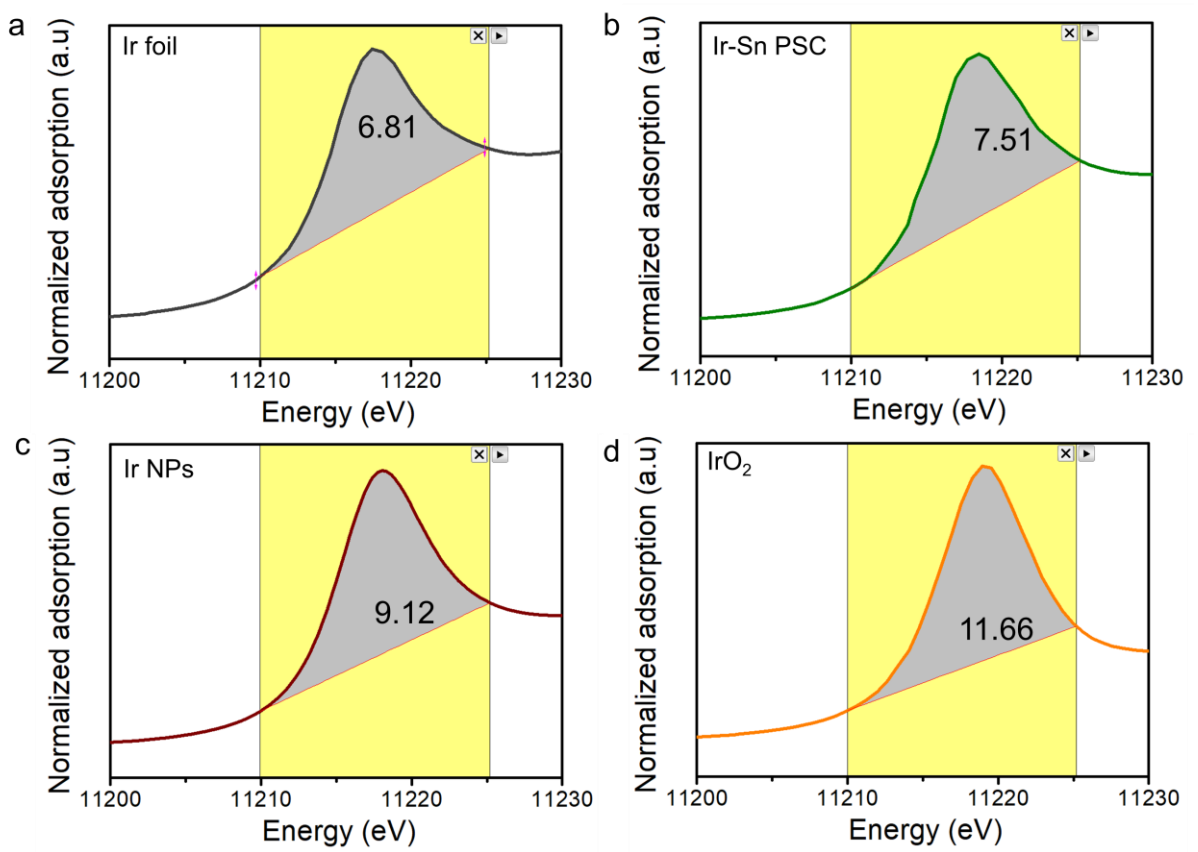

Fig. S24. White line peak area of Ir L_3-edge XANES for all catalysts. (a) Ir foil. (b) Ir-Sn PSC. (c) Ir NPs. (d) IrO_2. To qualitatively determine the average valence states of Ir in Ir NPs and Ir-Sn PSC, we conducted linear fitting based on the white line peak area difference to Ir foil as a function of the formal d-band hole count. The peak area was calculated based on the integral area from the data range of 11210 to 11252.2 eV.

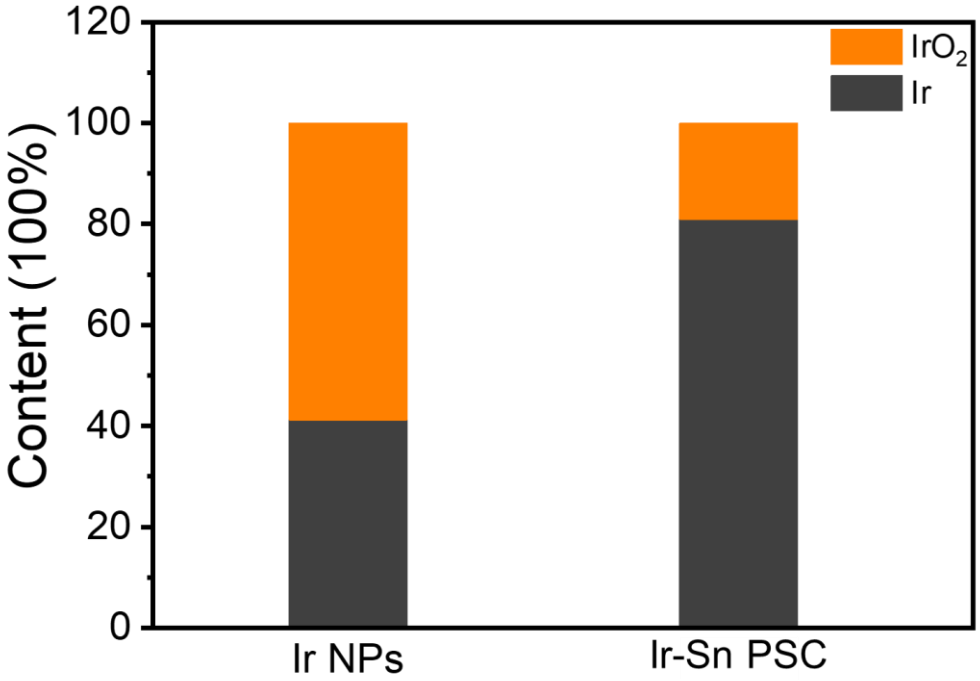

Fig. S25. Ir L_3-edge XANES spectra fitting results for Ir and IrO_2 in the Ir NPs and Ir-Sn PSC.

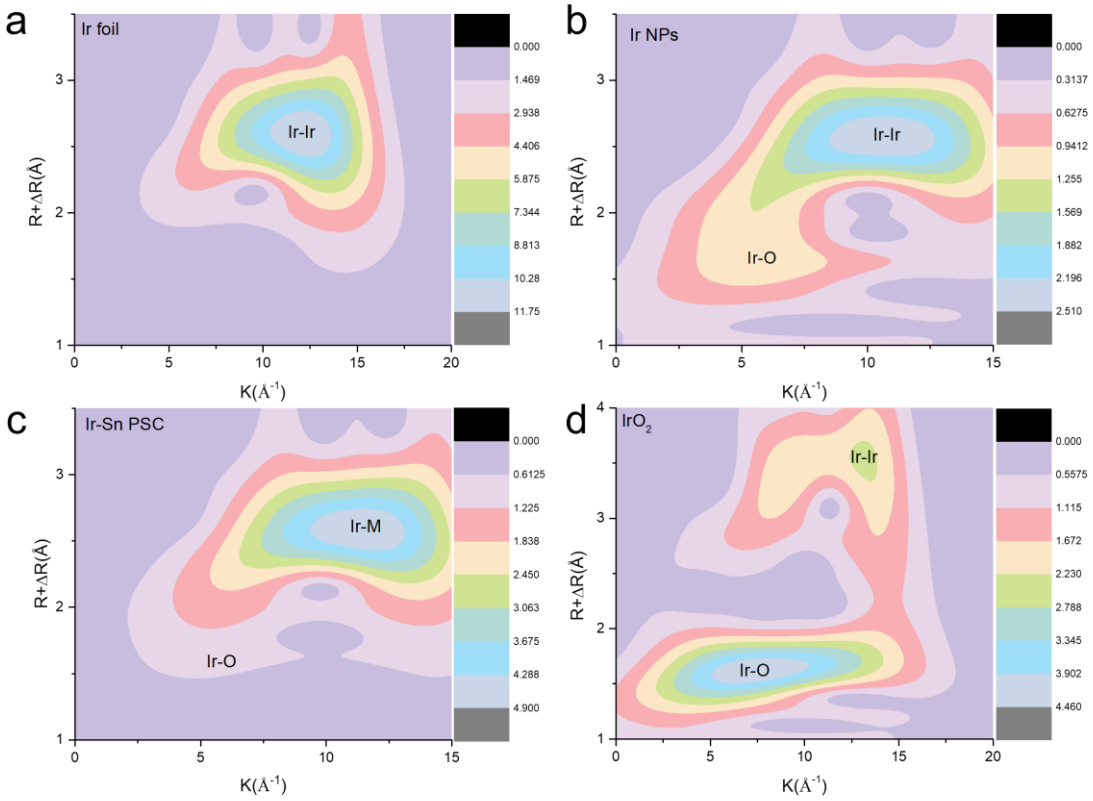

Fig. S26. WT-EXAFS contour maps of the Ir L_3-edge for all catalysts. (a) Ir foil. (b) Ir NPs. (c) Ir-Sn PSC. (d) IrO_2.

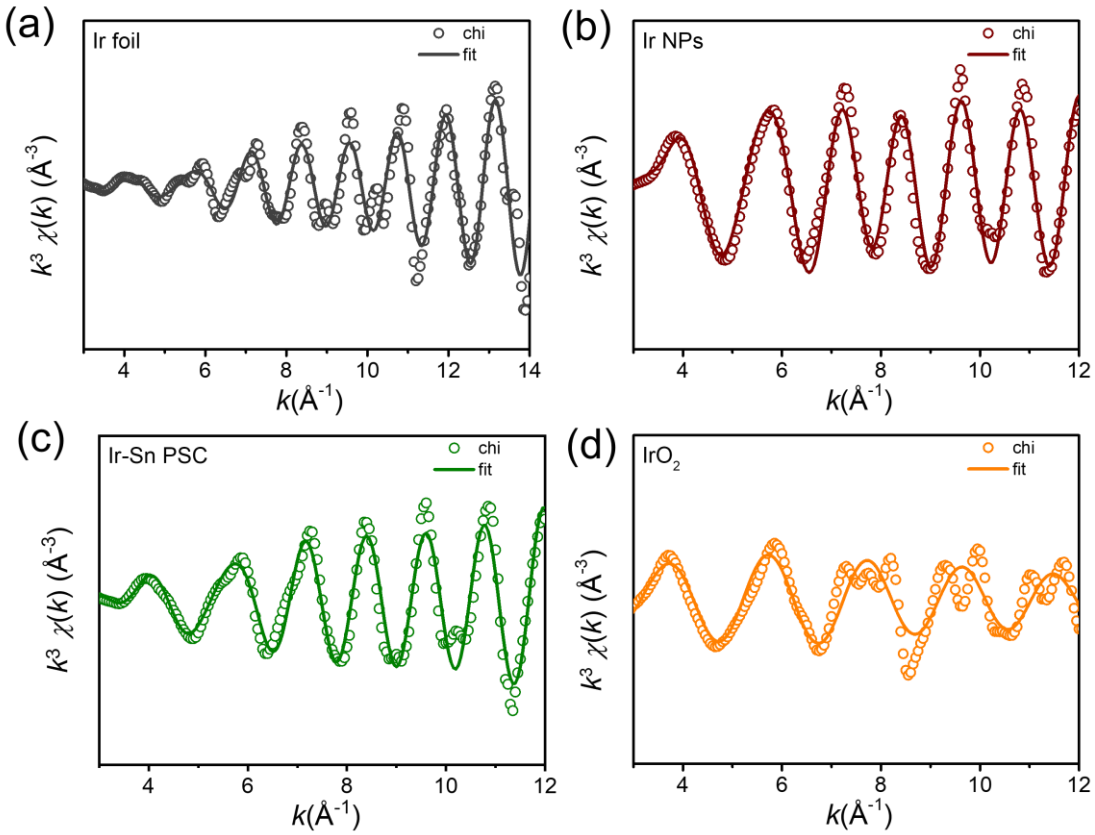

Fig. S27. The Ir L_3-edge EXAFS spectra for all catalysts. Ir foil (a), Ir NPs (b), IrO_2 (c), and Ir-Sn PSC (d), shown in k^3-weighted k-space.

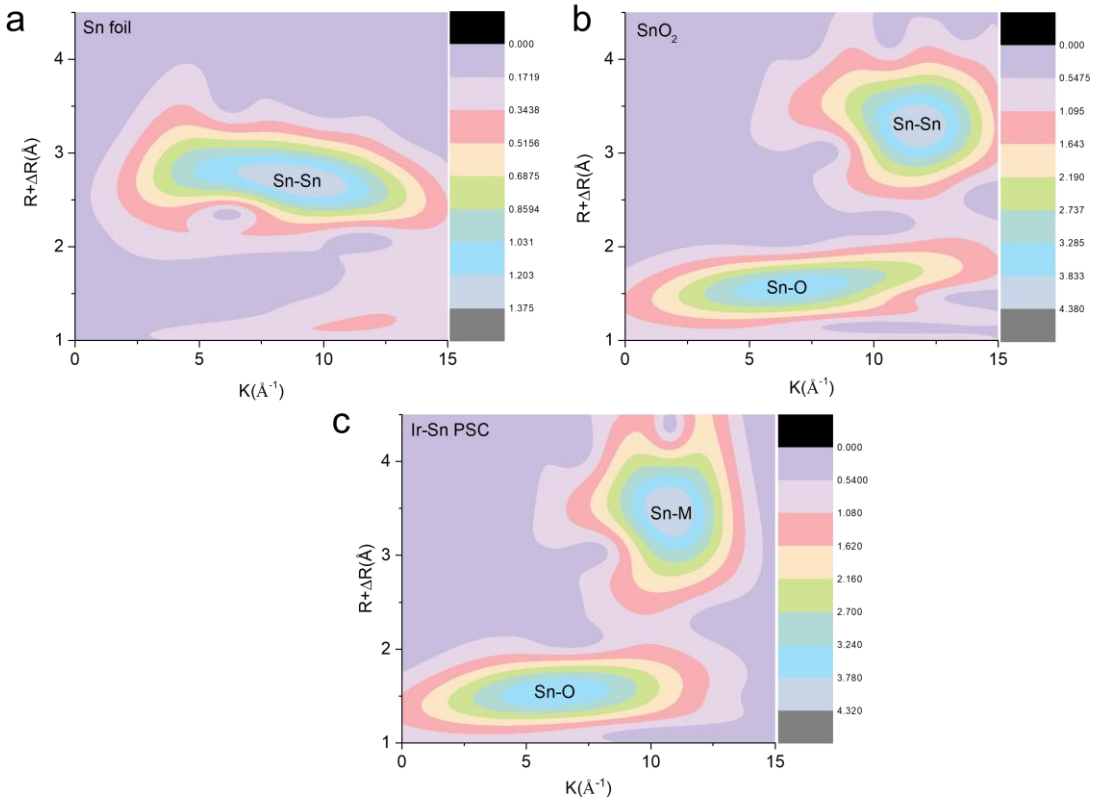

Fig. S28. WT contour maps of the Sn K-edge EXAFS spectra for all catalysts. (a) Sn foil, (b) SnO_2, and (c) Ir-Sn PSC.

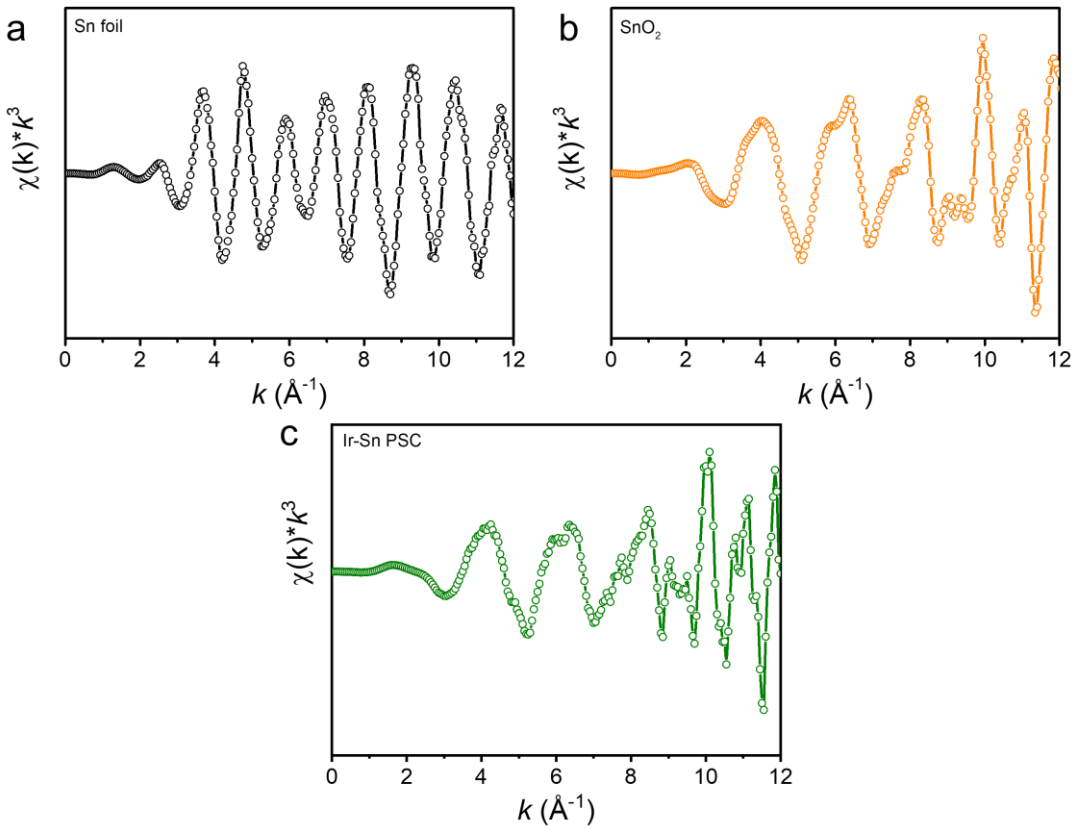

Fig. S29. The Sn K-edge EXAFS spectra for all catalysts. (a) Sn foil, (b) SnO_2, and (b) Ir-Sn PSC, shown in k^3-weighted k-space.

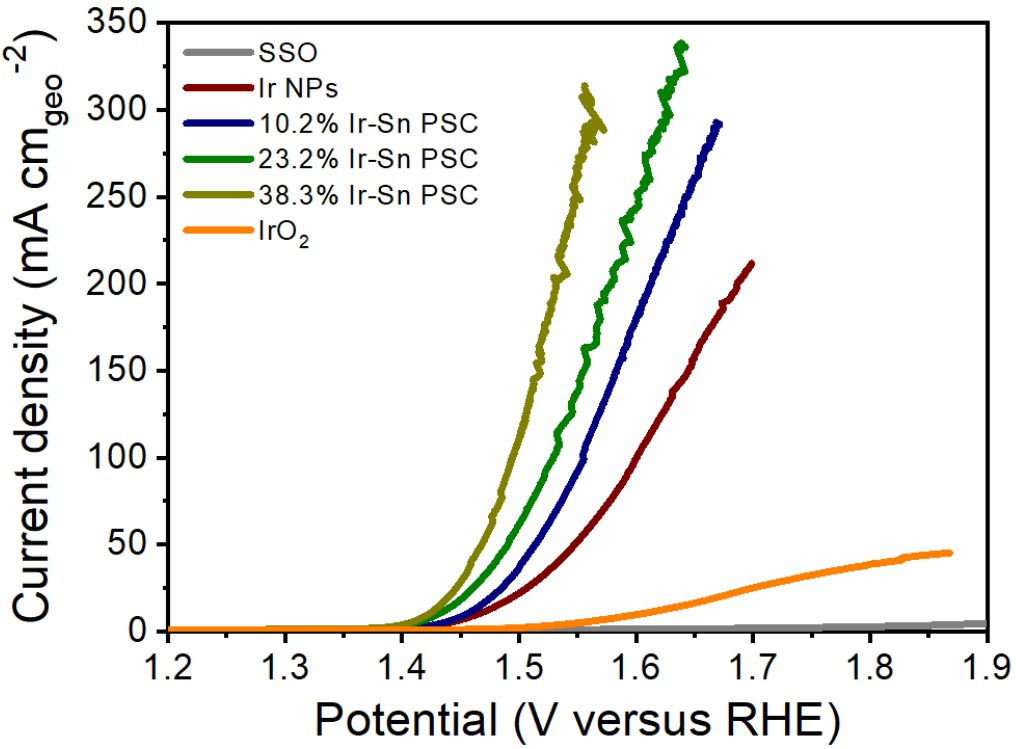

Fig. S30. LSV curves of SSO, Ir NPs, 10.2% Ir-Sn PSC, 23.2% Ir-Sn PSC, 38.5% Ir-Sn PSC, and IrO_2.

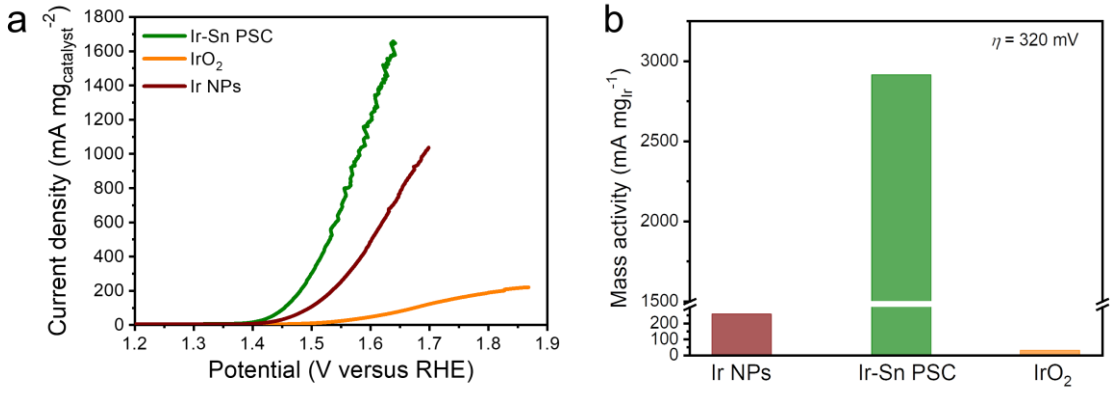

Fig. S31. Mass activity of all catalysts. (a) LSV curves based on the mass activity of Ir-Sn PSC, IrO_2, and Ir NPs. (b) The mass activity of Ir-Sn PSC, IrO_2, and Ir NPs based on their Ir content.

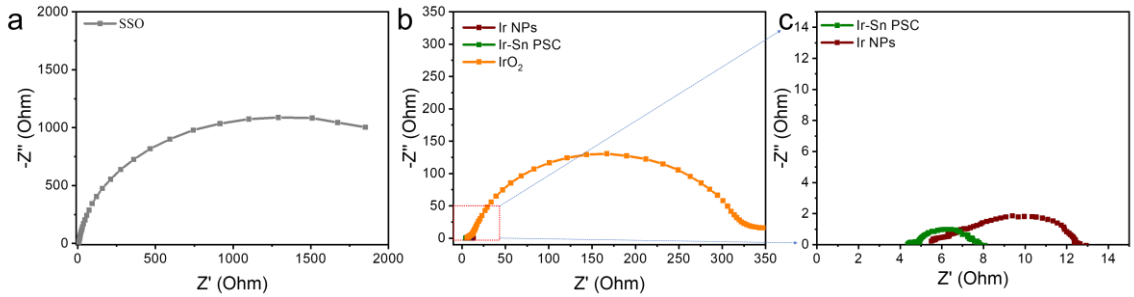

Fig. S32. Electrochemical impedance spectroscopy (EIS) spectra of all catalysts. (a) SSO. (b) Ir NPs, Ir-Sn PSC, and IrO_2. (c) Magnified EIS spectra of Ir NPs and Ir-Sn PSC in (b).

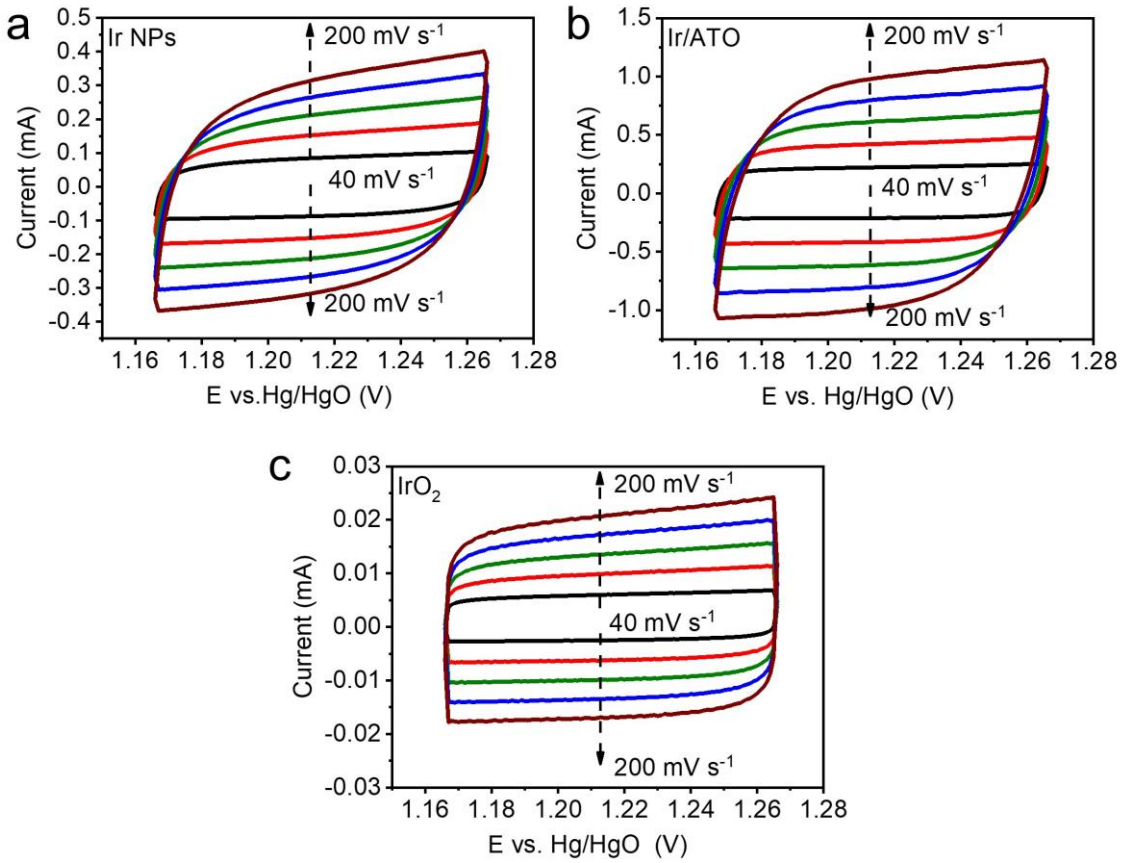

Fig. S33. CV curves. (a) Ir NPs, (b) Ir-Sn PSC, and (c) IrO_2 at different scan rates of 40, 80, 120, 160, and 200 mV s^{-1}, respectively.

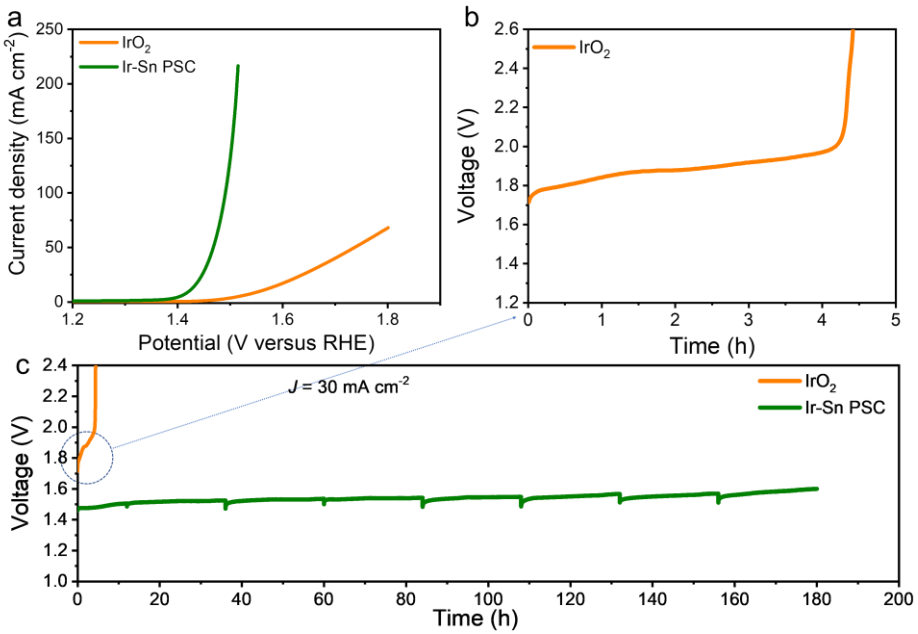

Fig. S34. LSV curves and stability test of IrO_2 and Ir-Sn PSC. (a) LSV curves of IrO_2 and Ir-Sn PSC loaded on carbon paper with mass loading of 1 mg catalyst. (b) Stability test of IrO_2 at 30 mA cm^{-2}. (c) Long-term stability test of Ir-Sn PSC at the current density of 30 mA cm^{-2} for 180 h of operation.

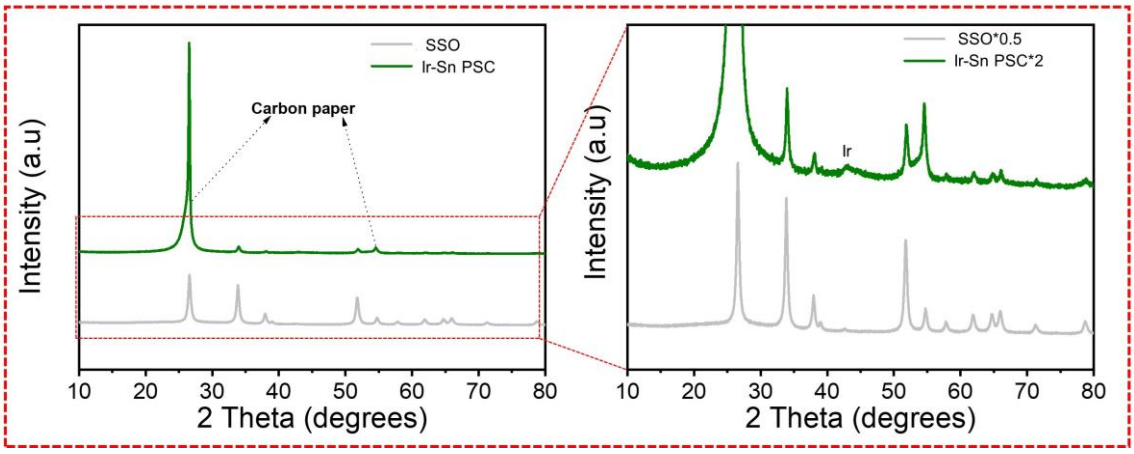

Fig. S35. XRD pattern of Ir-Sn PSC after the long-term stability test at 30 mA cm^{-2} for 180 h.

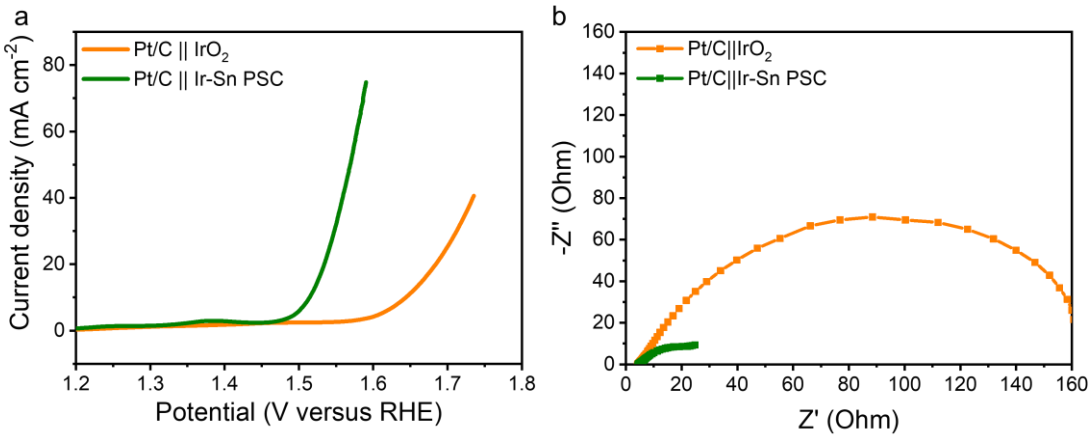

Fig. S36. LSV curves and EIS of Pt/C||IrO_2 and Pt/C||Ir-Sn PSC. (a) LSV curves of Pt/C||IrO_2 and Pt/C||Ir-Sn PSC without *iR* correction. (b) EIS spectra of Pt/C||IrO_2 and Pt/C||Ir-Sn PSC.

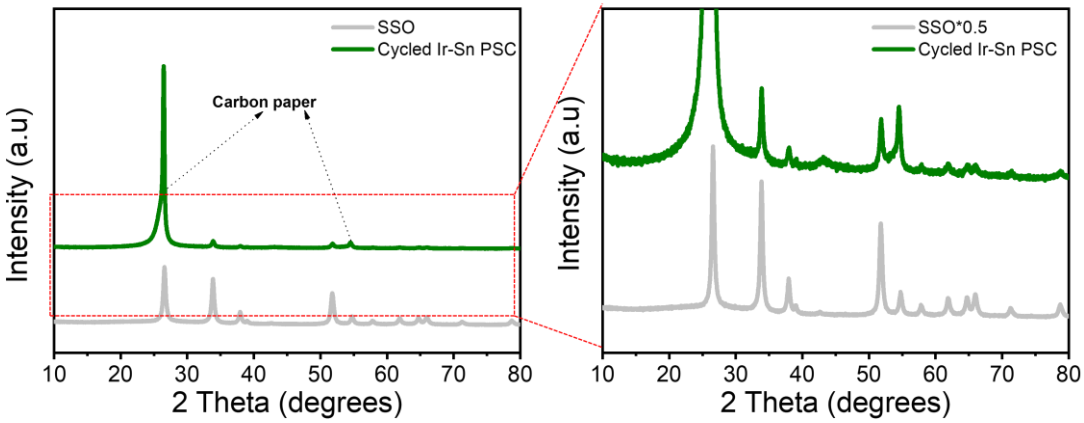

Fig. S37. XRD pattern of Ir-Sn PSC after long-term stability test at 20 mA cm^{-2} for 260 h in water splitting cell.

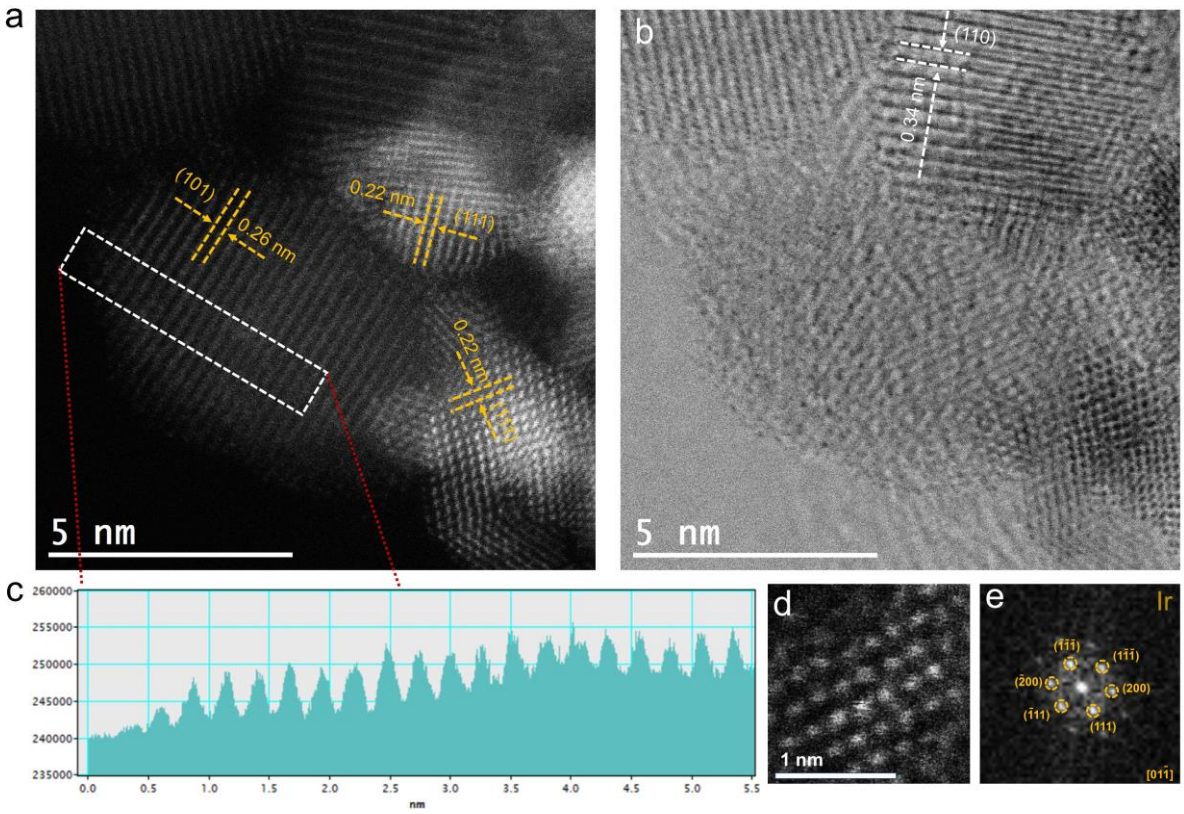

Fig. S38. Microscopic characterizations of cycled Ir-Sn PSC. (a) HAADF-STEM image of cycled Ir-Sn PSC. (b) The corresponding ABF-STEM image. (c) Intensity profile derived from the area in the white rectangle in (a). (d) HAADF-STEM image of Ir NPs on the cycled Ir-Sn PSC. (e) The corresponding FFT pattern.

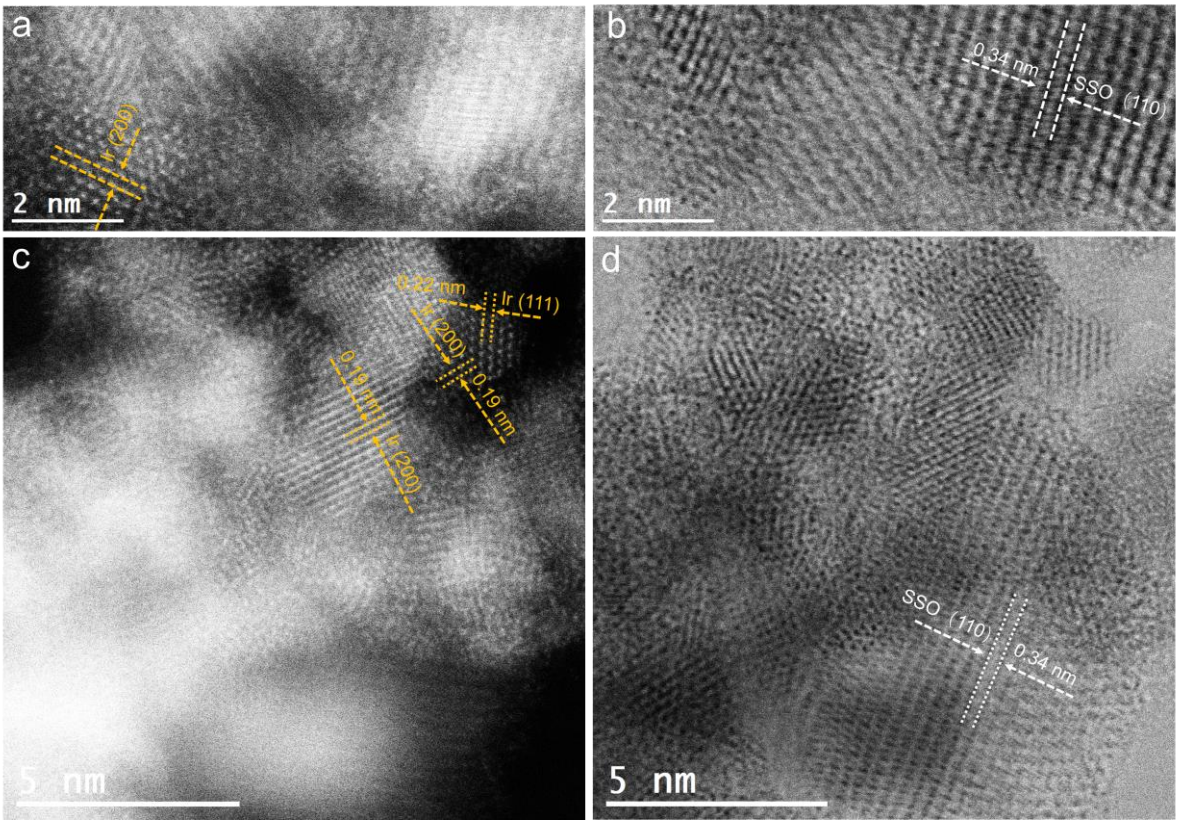

Fig. S39. Microscopic characterizations of cycled Ir-Sn PSC. (a) and (c) HAADF-STEM images. (b) and (d) The corresponding ABF-STEM images.

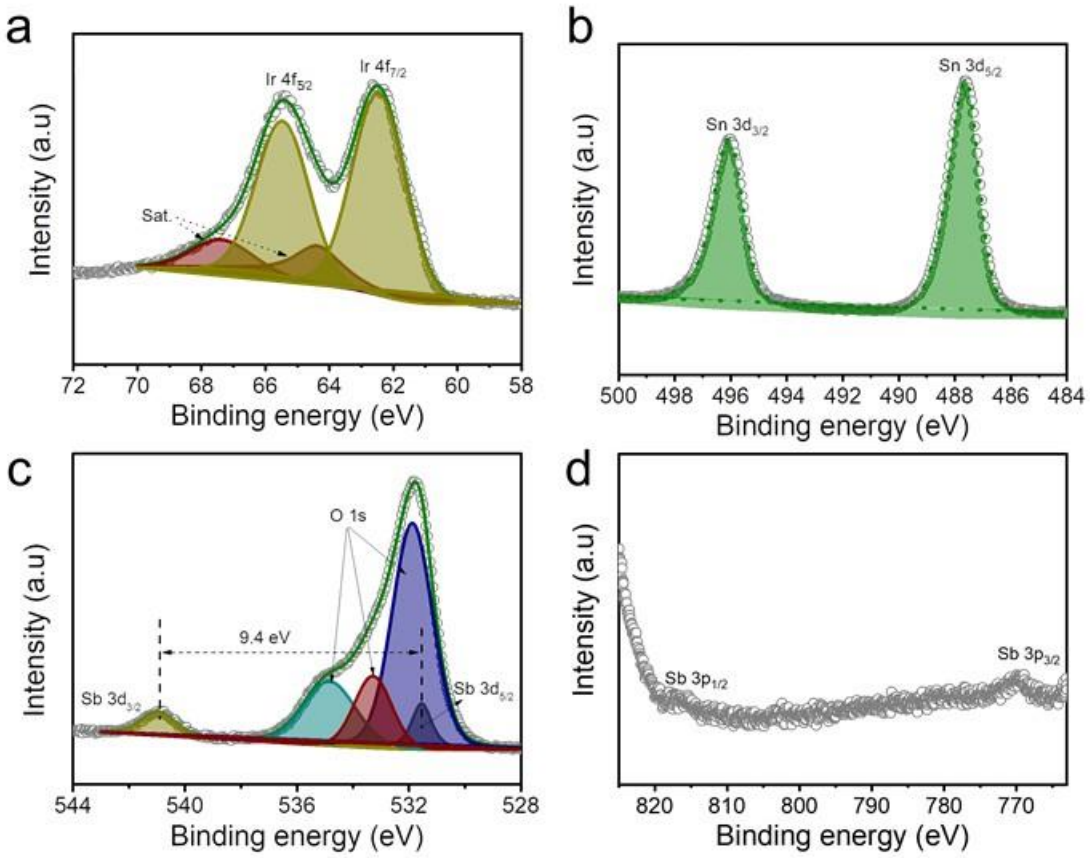

Fig. S40. High-resolution XPS spectra of cycled Ir-Sn PSC after 260 h of operation at 20 mA cm^{-2}. (a) Ir 4f. (b) Sn 3d. (c) Sb 3d + O 1s. (d) Sb 3p. Compared to Ir 4f spectra of Ir-Sn PSC, which feature a mixed-valence state of Ir^0 and Ir^{4+}, the cycled Ir-Sn PSC is shifted to higher binding energy with a set of doublets at 65.5 eV and 62.5 eV, which can be attributed to the Ir^{4+}, elucidating the partial oxidation of surface Ir species from Ir^0 to Ir^{4+} after the long-term stability test. The positive shift of the Ir 4f, Sn 3d, and Sb 3d spectra of cycled Ir-Sn PSC suggest the slight oxidation of Ir, Sn, and Sb after long-term cycling.

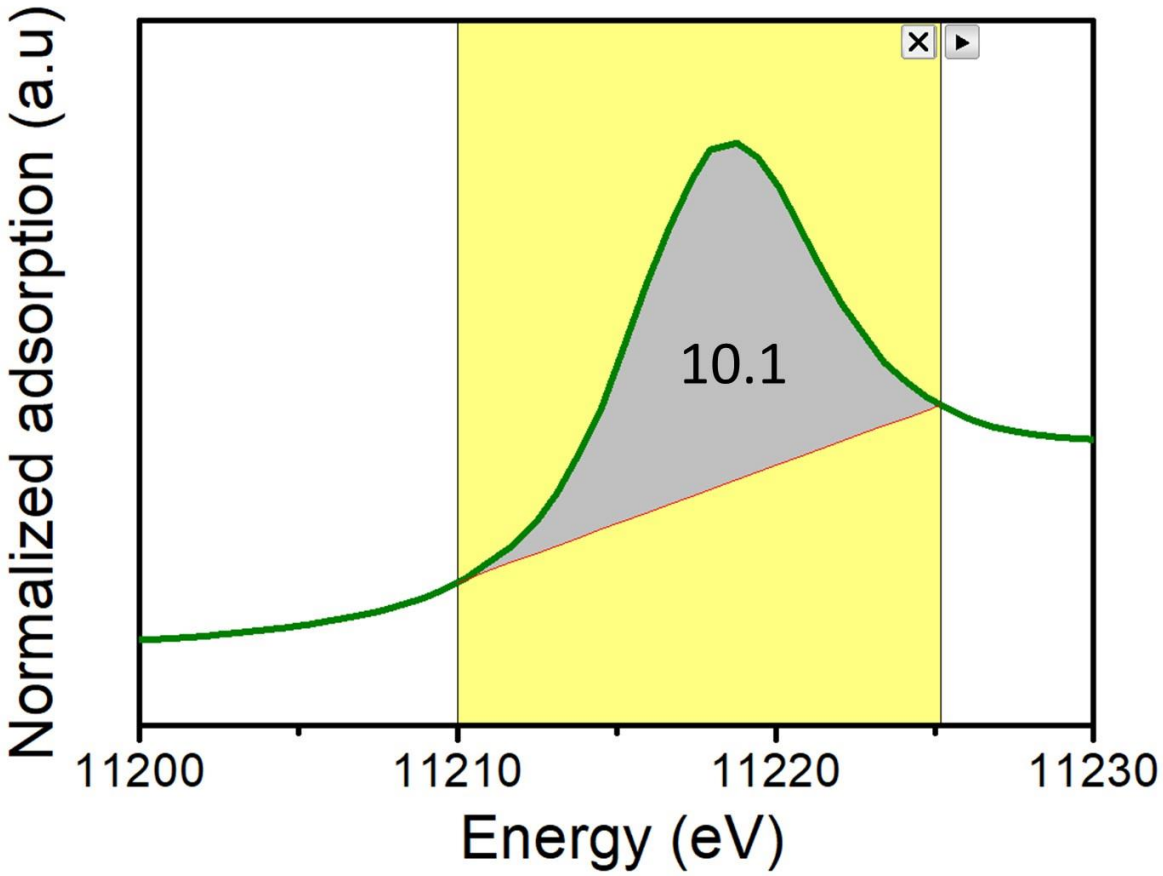

Fig. S41. White line peak area of Ir L_3-edge XANES for cycled Ir-Sn PSC. The peak area was calculated based on the integral area from the data range of 11210 to 11252.2 eV.

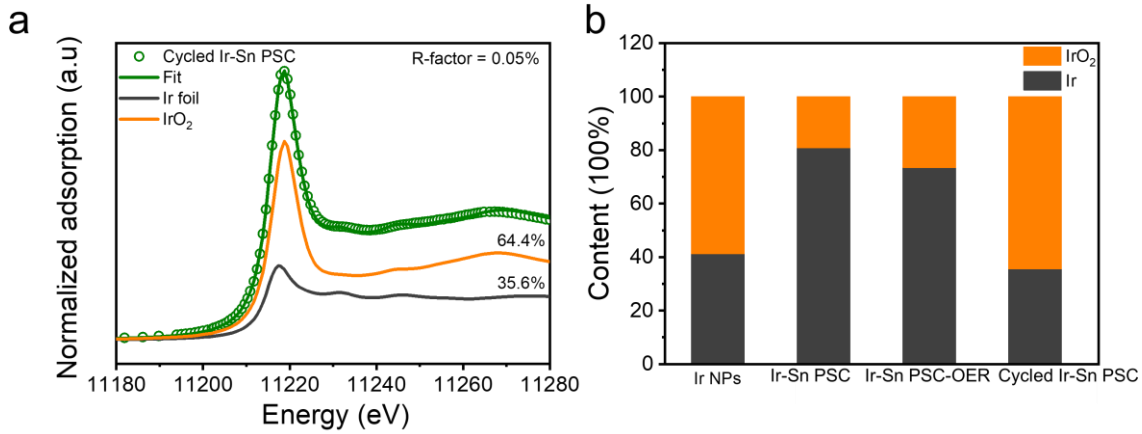

Fig. S42. Ir L_3-edge XANES spectra fitting result. (a) Ir L_3-edge XANES spectra fitting result for cycled Ir-Sn PSC using the spectra of Ir foil and IrO_2. (b) Fitting contents of Ir and IrO_2 in the Ir NPs, Ir-Sn PSC. Ir-Sn PSC_OER, and cycled Ir-Sn PSC.

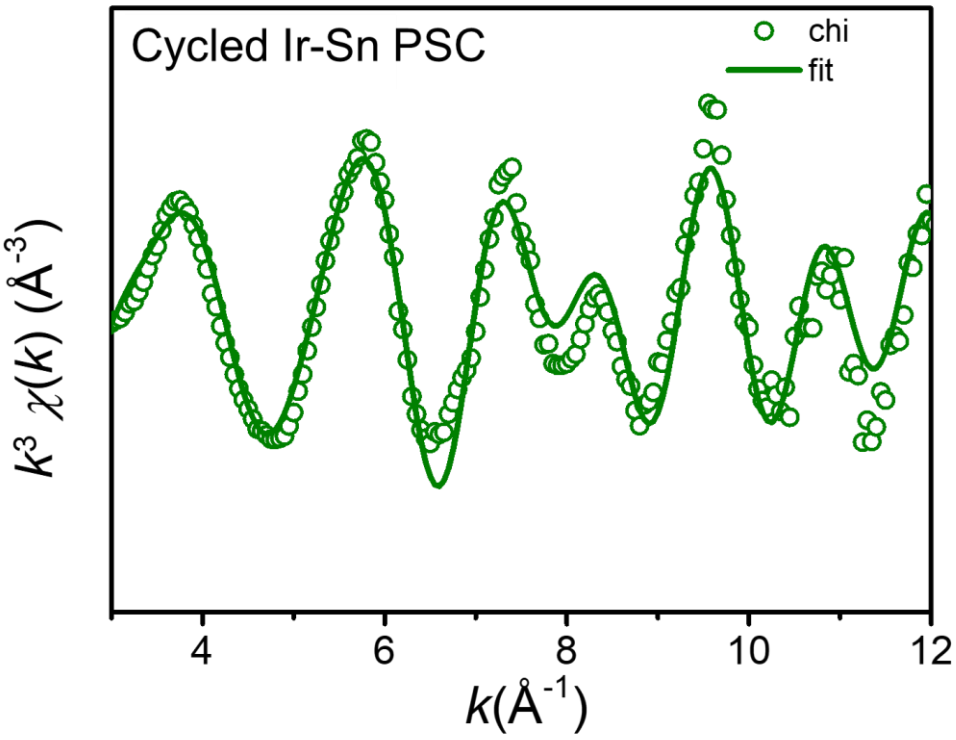

Fig. S43. Ir L_3-edge EXAFS spectrum (points) and curve-fit (line) cycled Ir-Sn PSC, shown in k^3-weighted k space.

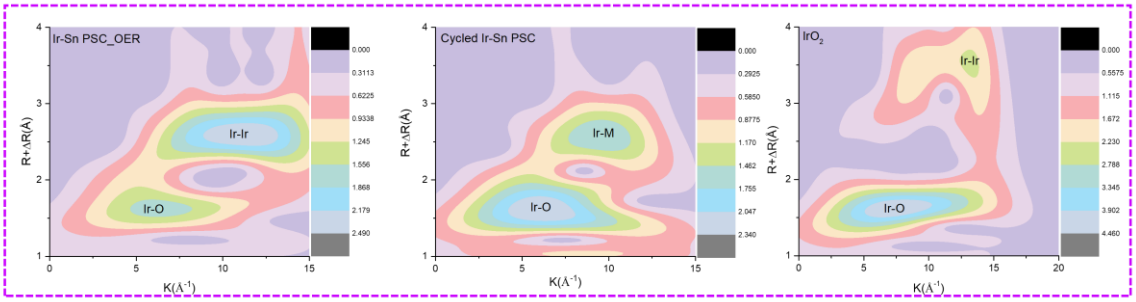

Fig. S44. WT plots for the Ir L_3-edge k^3 weighted EXAFS spectra. WT plots for the Ir L_3-edge k^3 weighted EXAFS spectra of Ir-Sn PSC before (left) and after (middle) long-term stability testing at a current density of 20 mA cm^{-2} for 260 h, along with IrO_2 as a reference (right).

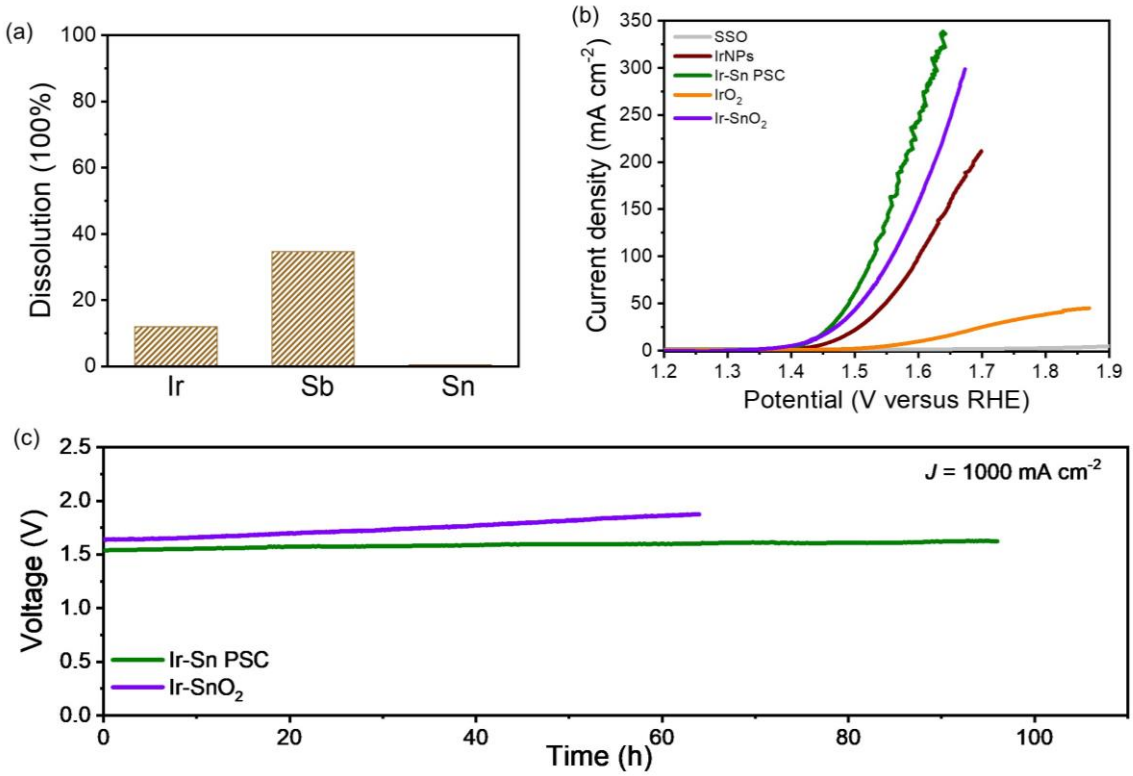

Fig. S45. Metal dissolution and electrochemical performance. (a) The metal dissolution of Ir, Sb, and Sn in Ir-Sn PSC after operation at 30 mA cm^2 for 192 h. (b) Polarization curves of SSO, Ir NPs, Ir-SnO_2, Ir-Sn PSC, and IrO_2. (c) Stability test of PEMWE using Ir-Sn PSC and Ir-SnO_2 operated at 1000 mA cm^{-2}.

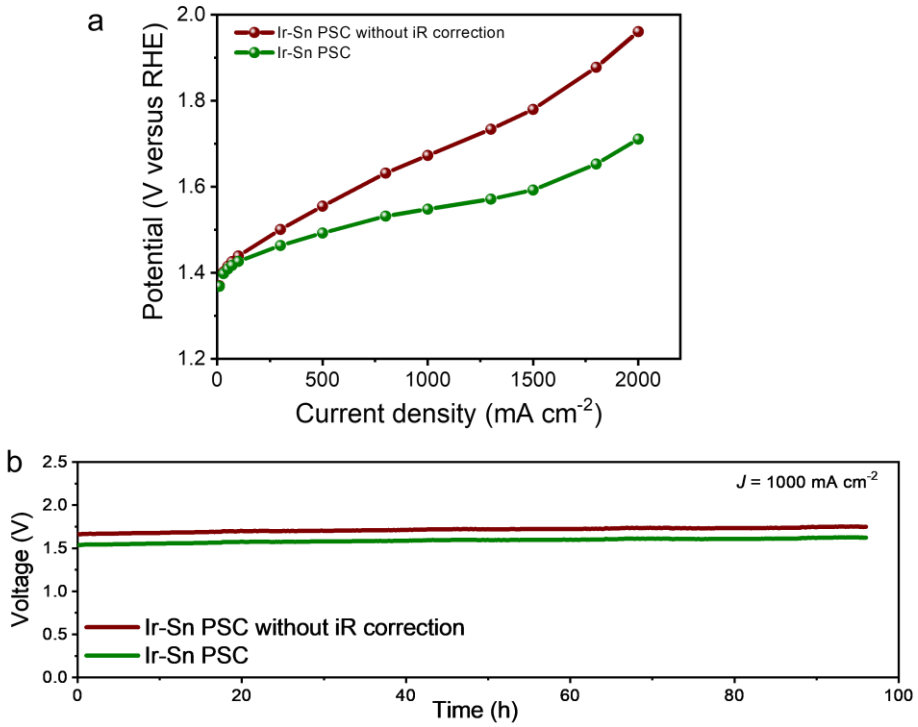

Fig. S46. LSV curves and stability test of PEM electrolyzer using Ir-Sn PSC as the anode catalyst. (a) Polarization curves with and without *iR* correction. (b) CP test operated at 1000 mA cm^{-2} with and without *iR* correction.

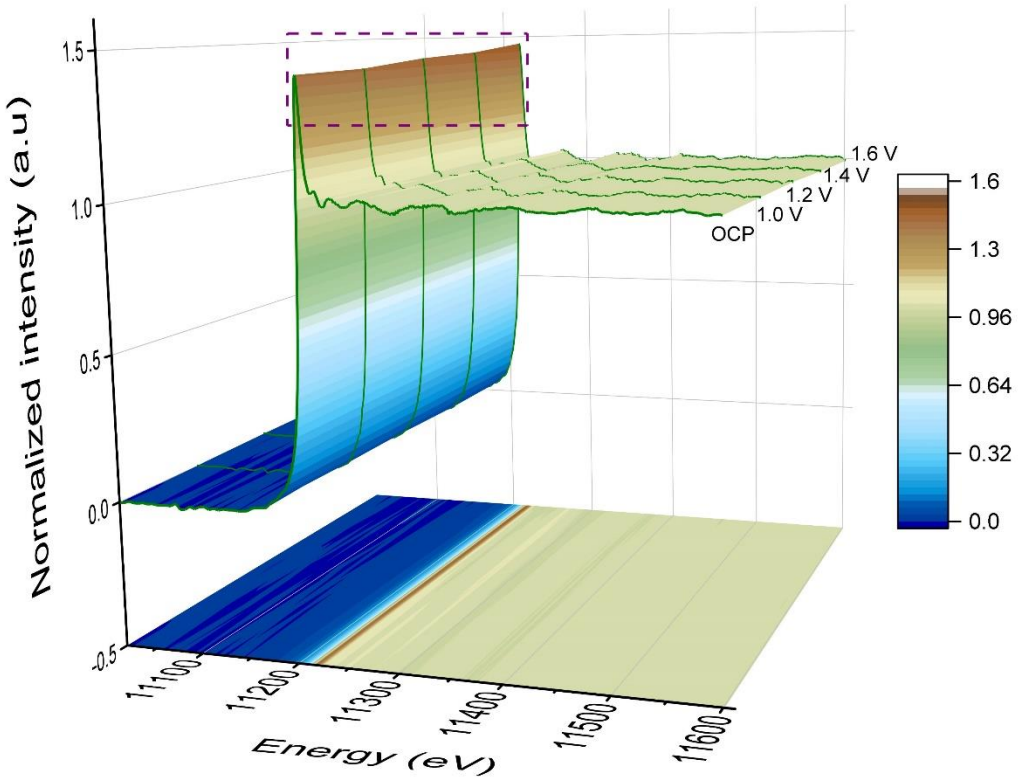

Fig. S47. 3D *Operando* XANES spectra of the Ir L_3-edge for Ir-Sn PSC at different voltages.

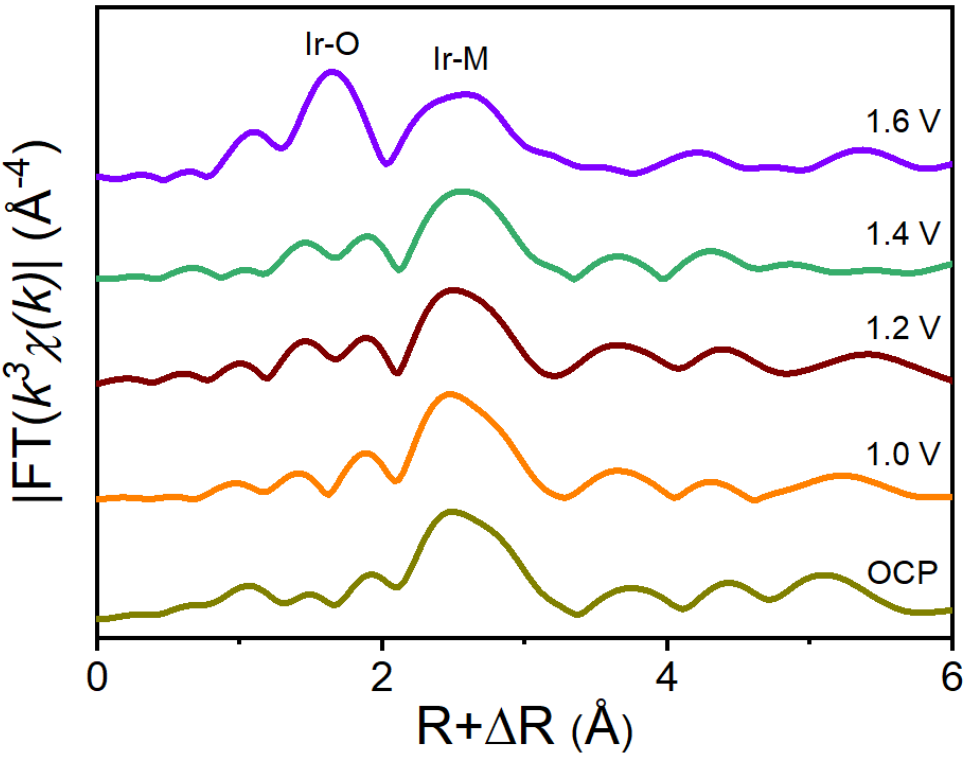

Fig. S48. *In-situ* EXAFS spectra of the Ir L_3-edge for Ir-Sn PSC at different voltages. The data are k^3-weighted and not phase-corrected.

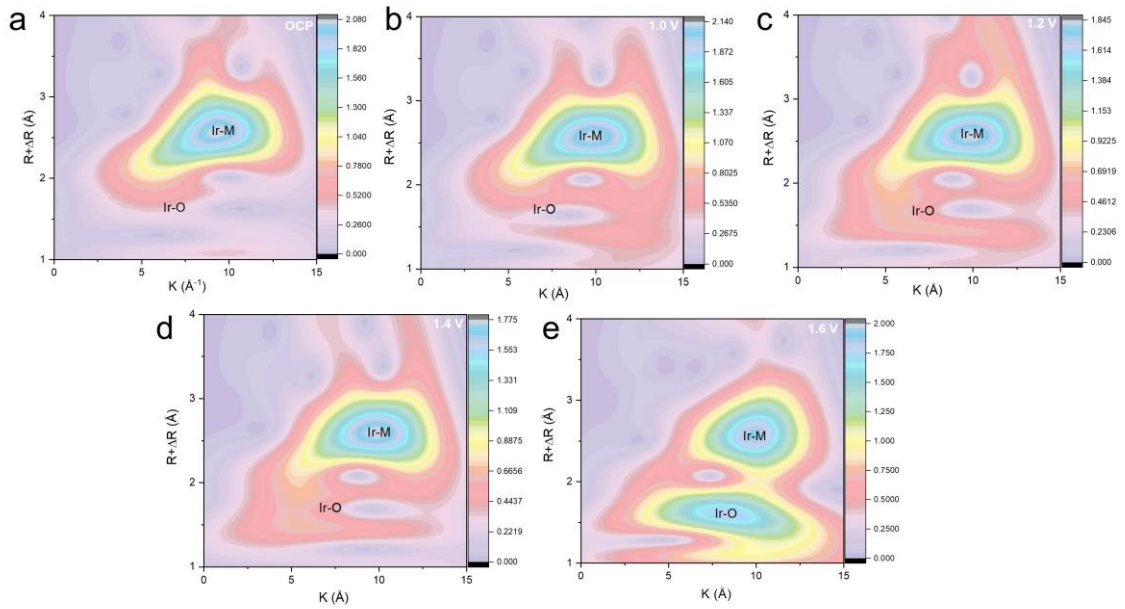

Fig. S49. *In-situ* WT plots for the Ir L_3-edge k^3 weighted EXAFS signal for Ir-Sn PSC at different potentials. (a) OCP. (b) 1.0 V. (c) 1.2 V. (d) 1.4 V. (e) 1.6 V.

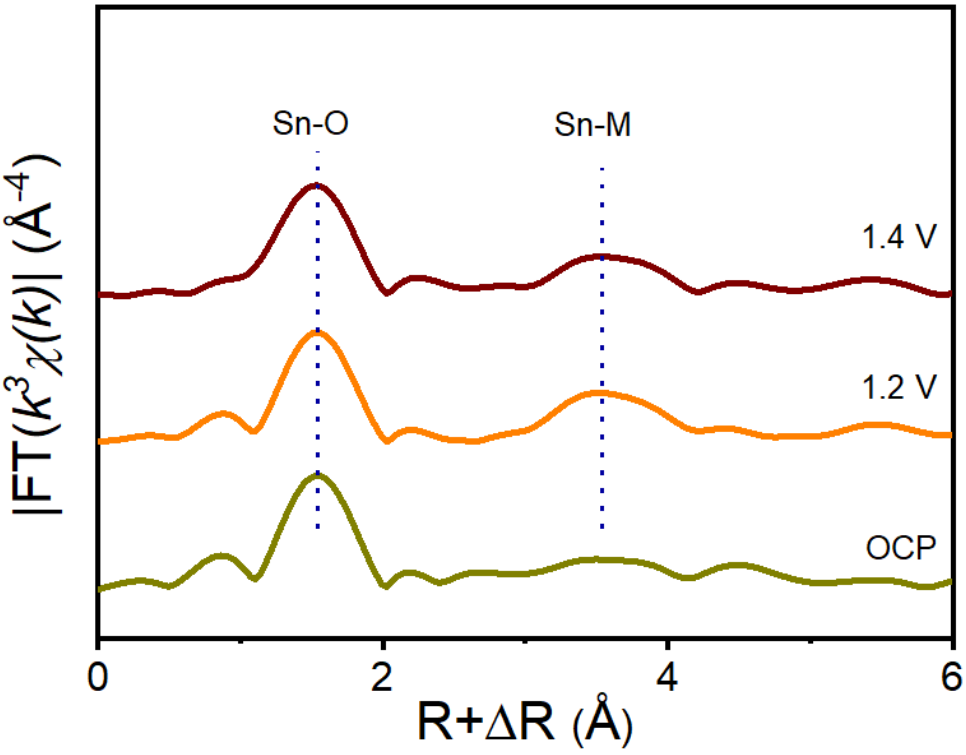

Fig. S50. ***In-situ*** **Sn K-edge FT-EXAFS spectra at the OCP, 1.2 V, and 1.4 V vs. RHE in 0.5 M H_2SO_4 solution.** The data are k^3-weighted and not phase-corrected.

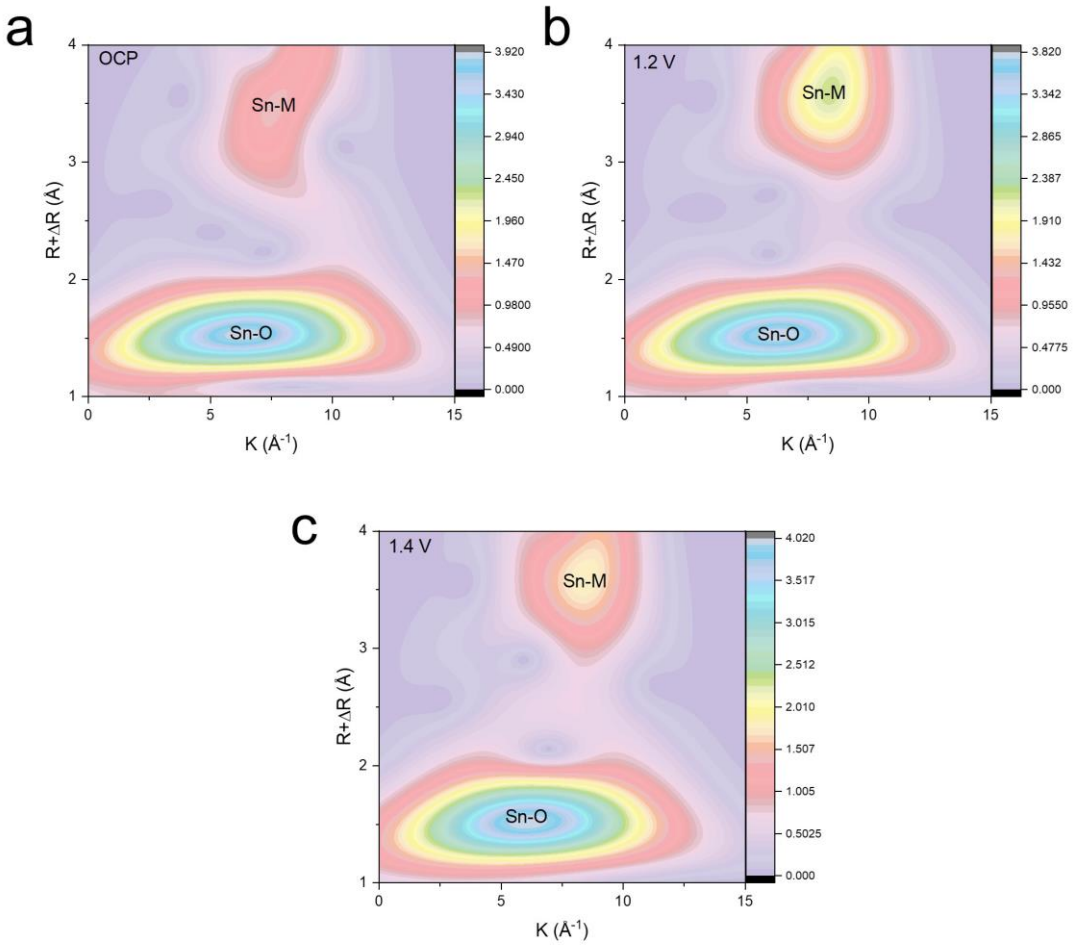

Fig. S51. WT-EXAFS plots of the Sn K-edge for Ir-Sn PSC at different potentials. (a) OCP. (b) 1.2 V. (c) 1.4 V.

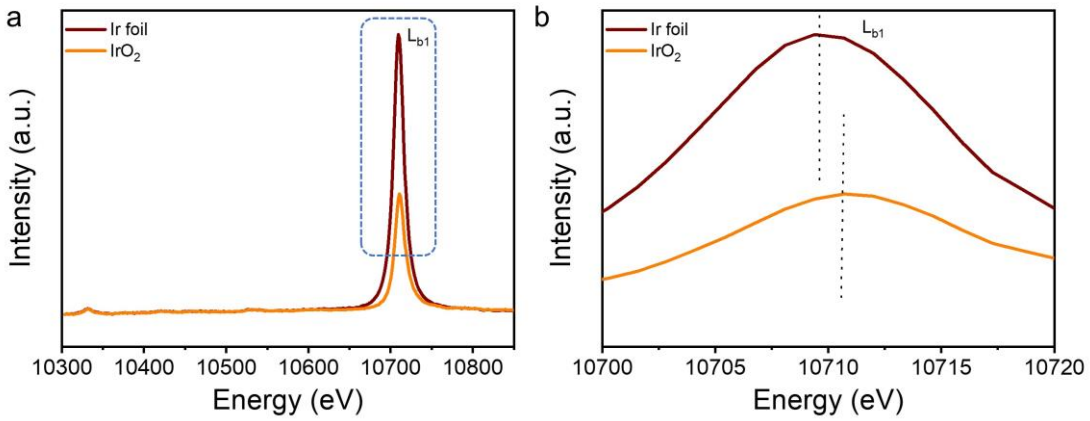

Fig. S52. XES spectra. (a). XES spectra of the Ir foil and IrO_2 reference samples, featuring an L_{b1} main line at ~10.709 keV derives from the L_2 ($3d_{3/2}$)-M_4 ($2p_{1/2}$) transition. (b). Magnification of the indicated area in (a).

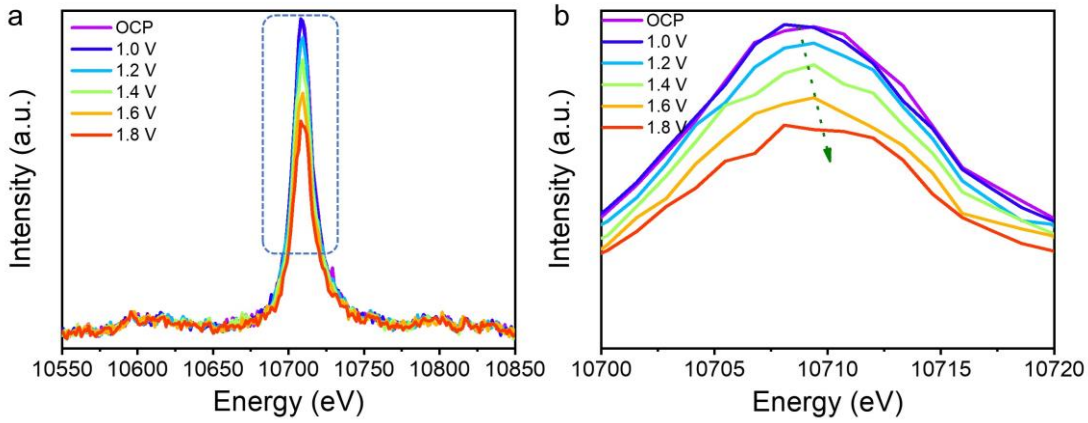

Fig. S53. *In situ* Ir L_{b1} XES spectra. (a). *In situ* Ir L_{b1} XES spectra recorded on Ir-Sn PSC from open circuit potential to 1.8 V vs. RHE. (b). Magnification of the indicated area in (a).

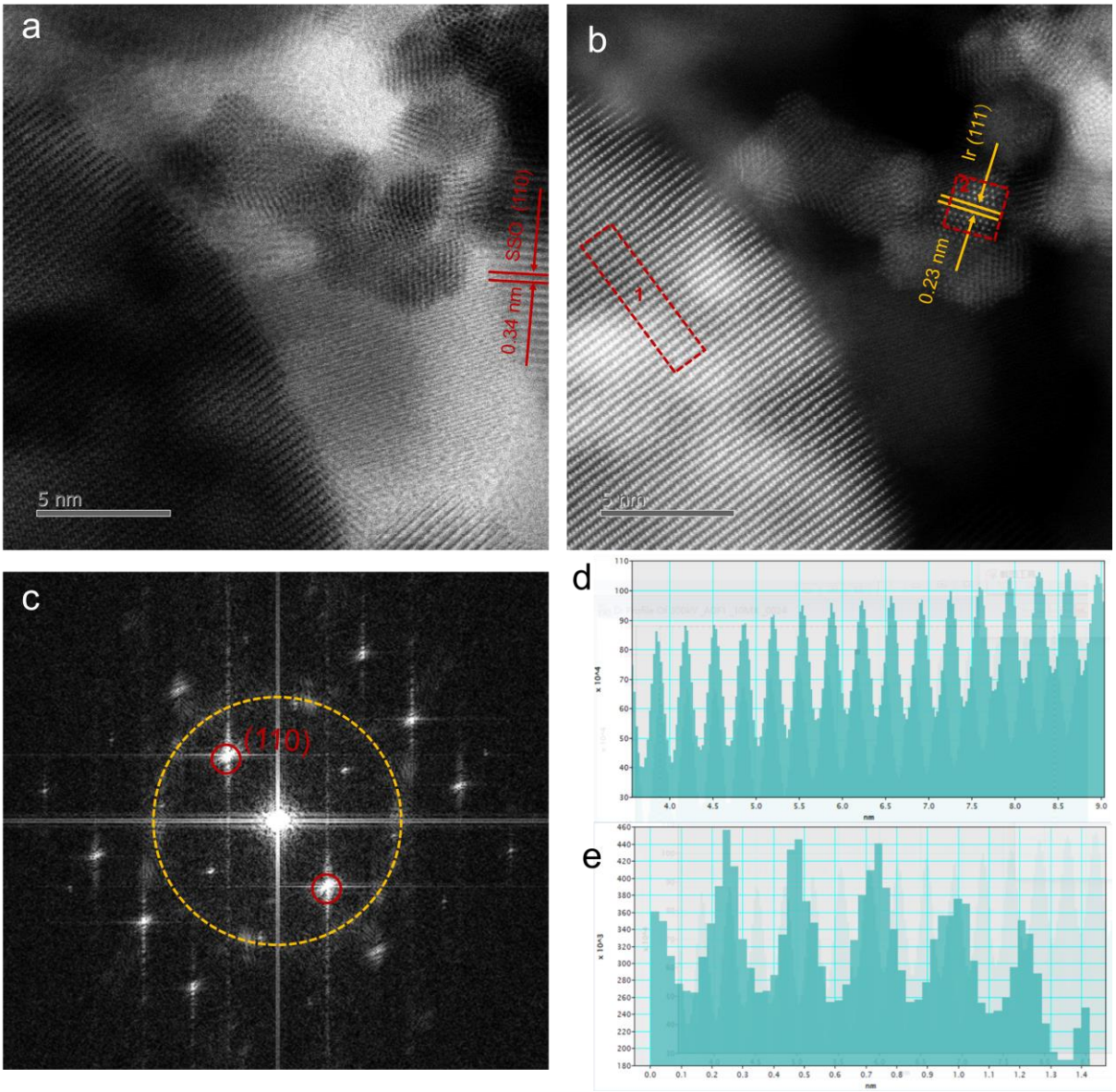

Fig. S54. Microscopic characterizations of Ir-Sn PSC_OER. (a) ABF-STEM and (b) HAADF-STEM images of Ir-Sn PSC_OER. (c) The corresponding FFT pattern. (d) and (e) Intensity profiles for the rectangular areas 1 and 2 in (b), respectively.

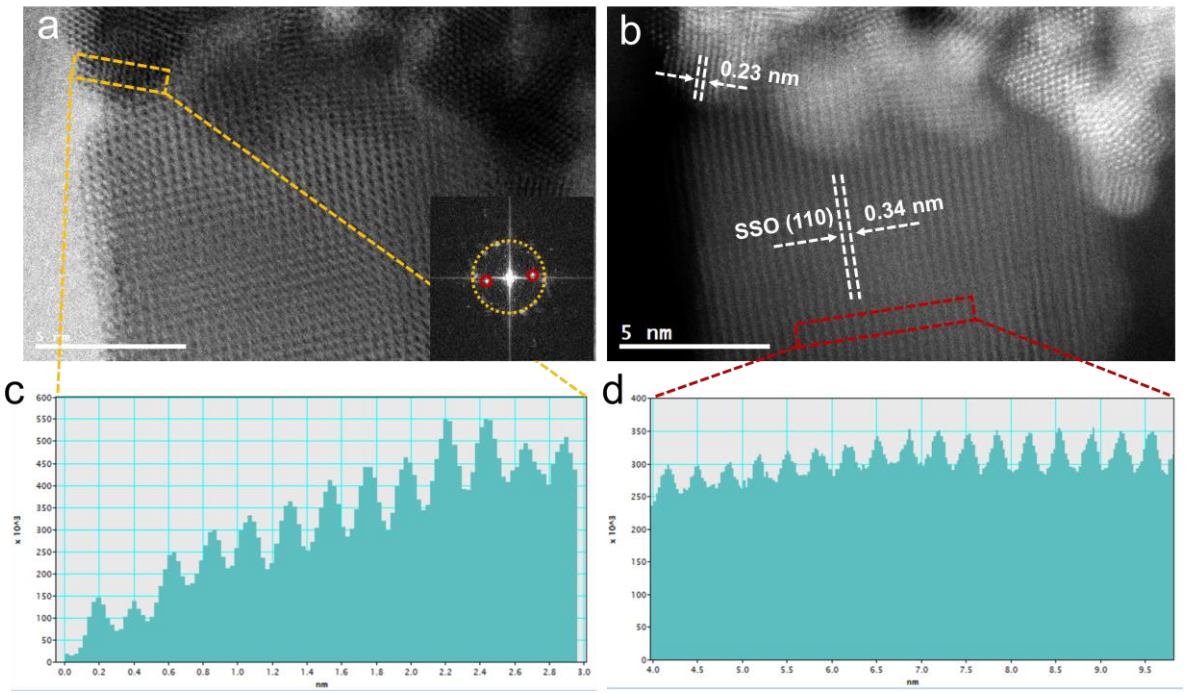

Fig. S55. Microscopic characterizations of Ir-Sn PSC_OER. (a) ABF-STEM amd (b) HAADF-STEM image of Ir-Sn PSC_OER. (c) and (d) Intensity profiles for the rectangular areas in (a) and (b) respectively.

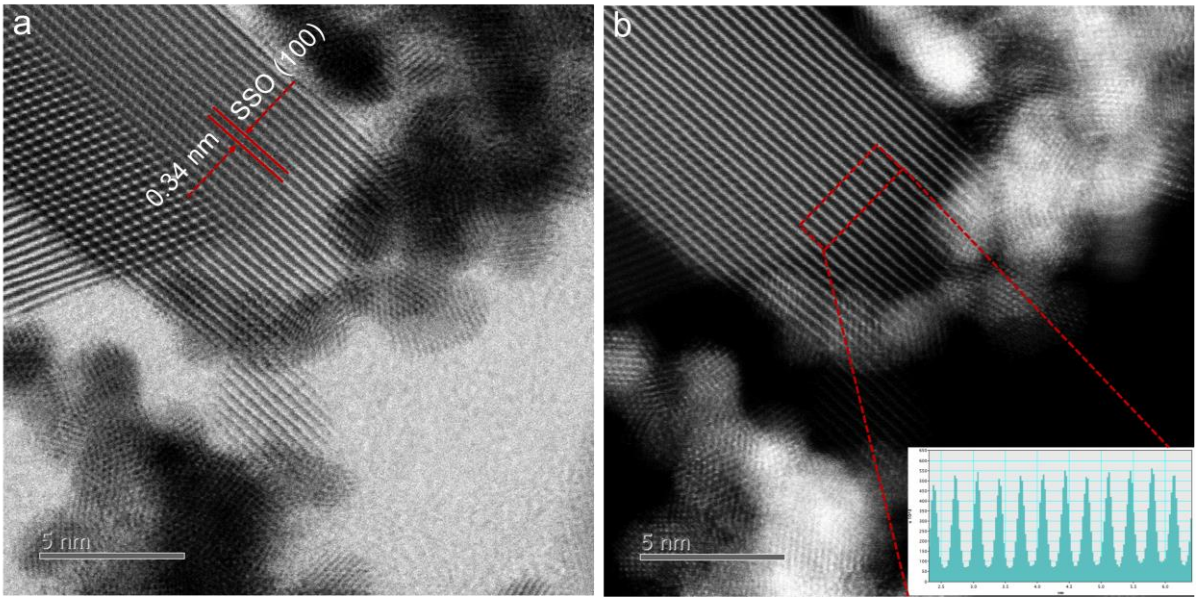

Fig. S56. Representative HAADF-STEM and ABF-STEM images of Ir-Sn PSC_OER. (a) HAADF-STEM image. (b) ABF-STEM image.

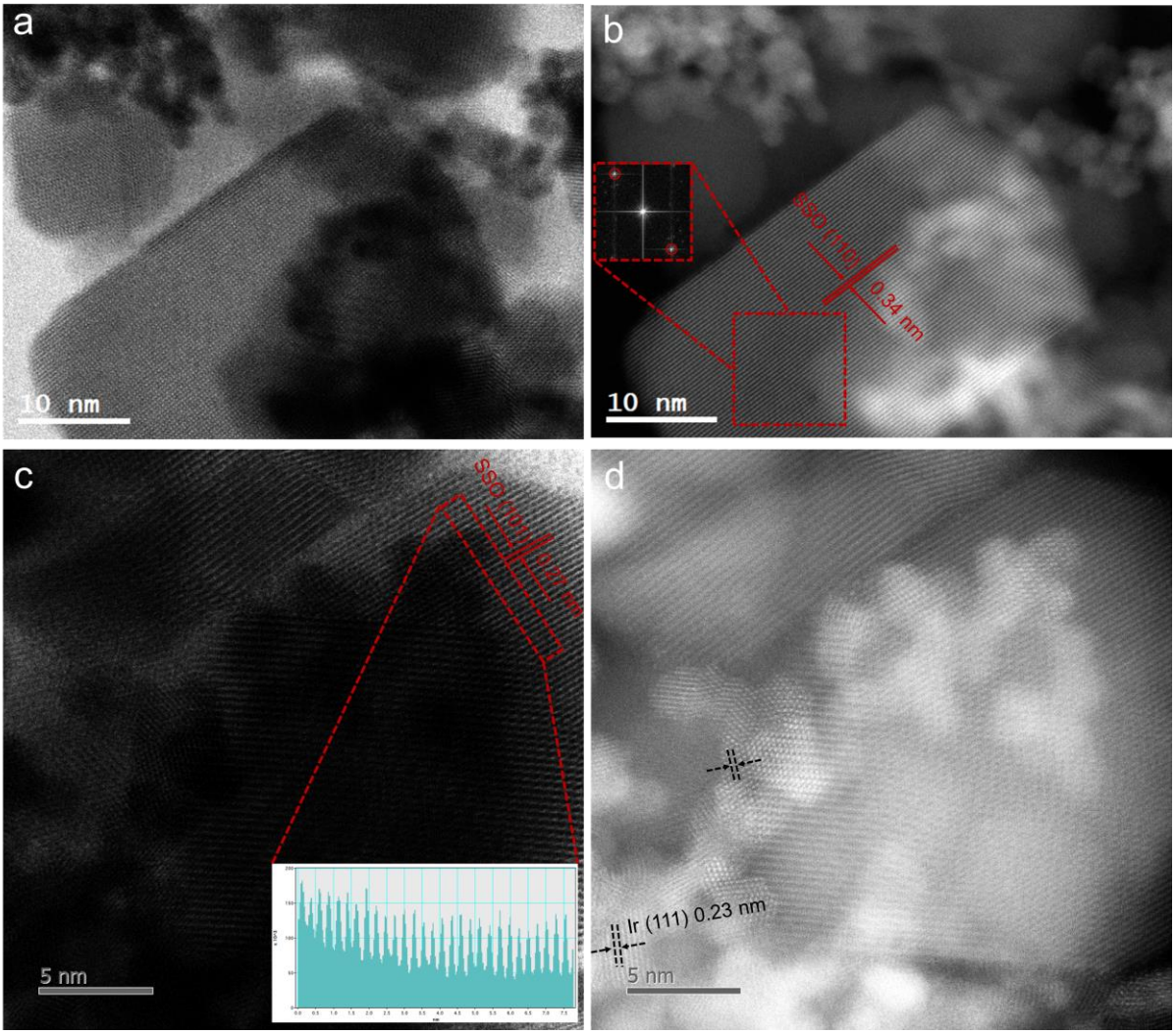

Fig. S57. Representative HAADF-STEM and ABF-STEM images of Ir-Sn PSC_OER. (a) and (c) HAADF-STEM images. (b) and (d) ABF-STEM images.

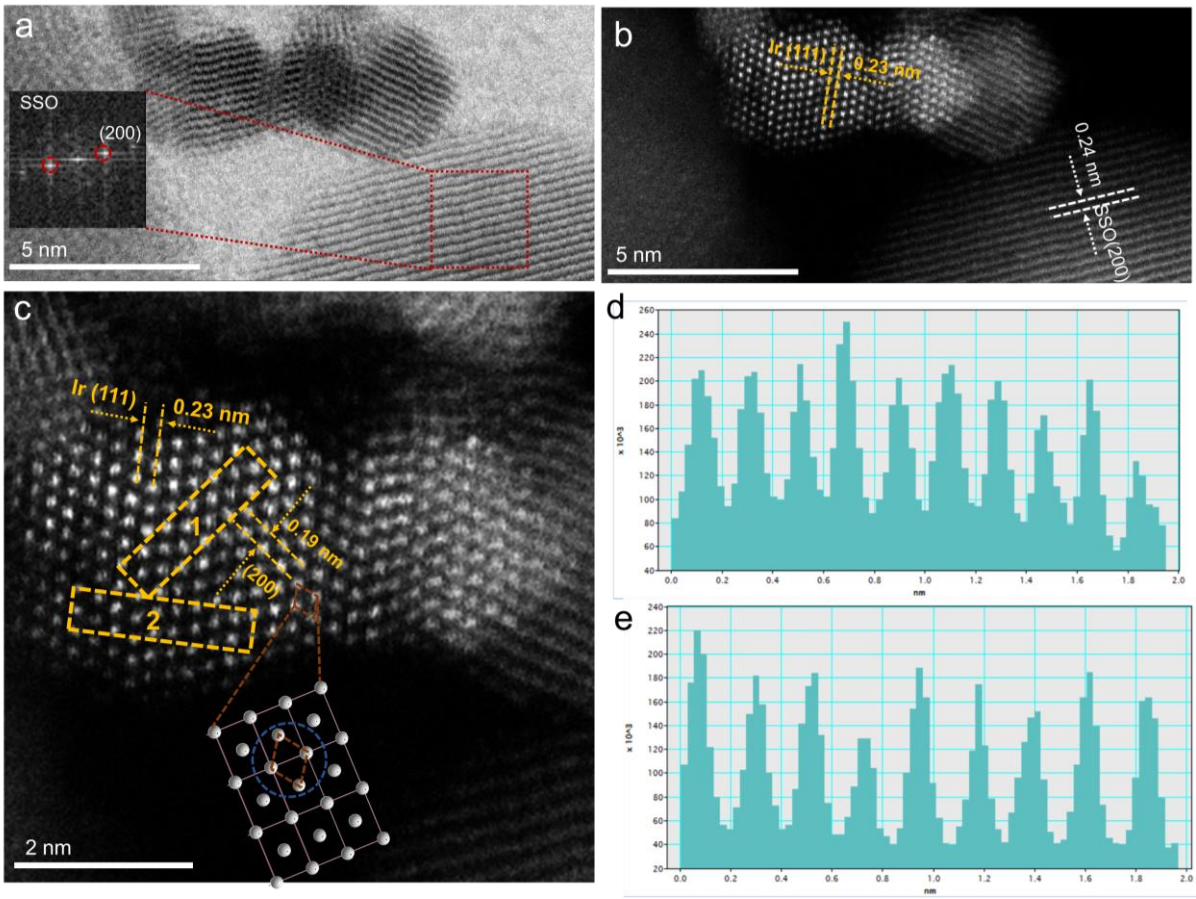

Fig. S58. Microscopic characterizations of Ir-Sn PSC_OER. (a) ABF-STEM image of Ir-Sn PSC_OER. (b) and (c) HAADF-STEM images. (d) and (e) Intensity profiles for the areas in rectangles 1 and 2 in (c), respectively.

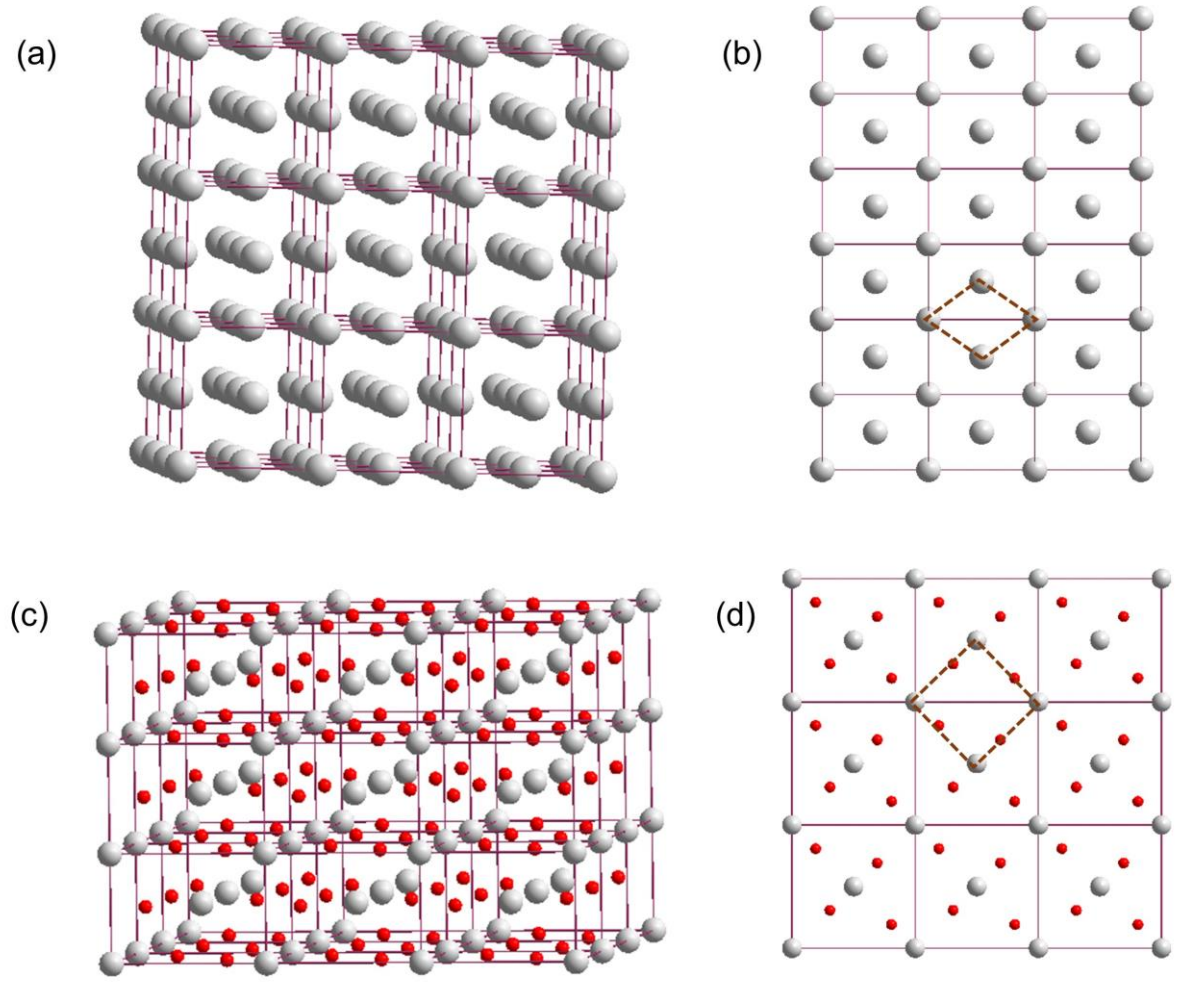

Fig. S59. Crystal structure of Ir and IrO_2. (a) Crystal structure of metallic Ir and (b) viewed from the $[01\bar{1}]$ zone axis. (c) Crystal structure of IrO_2 and (d) viewed from [001] direction.

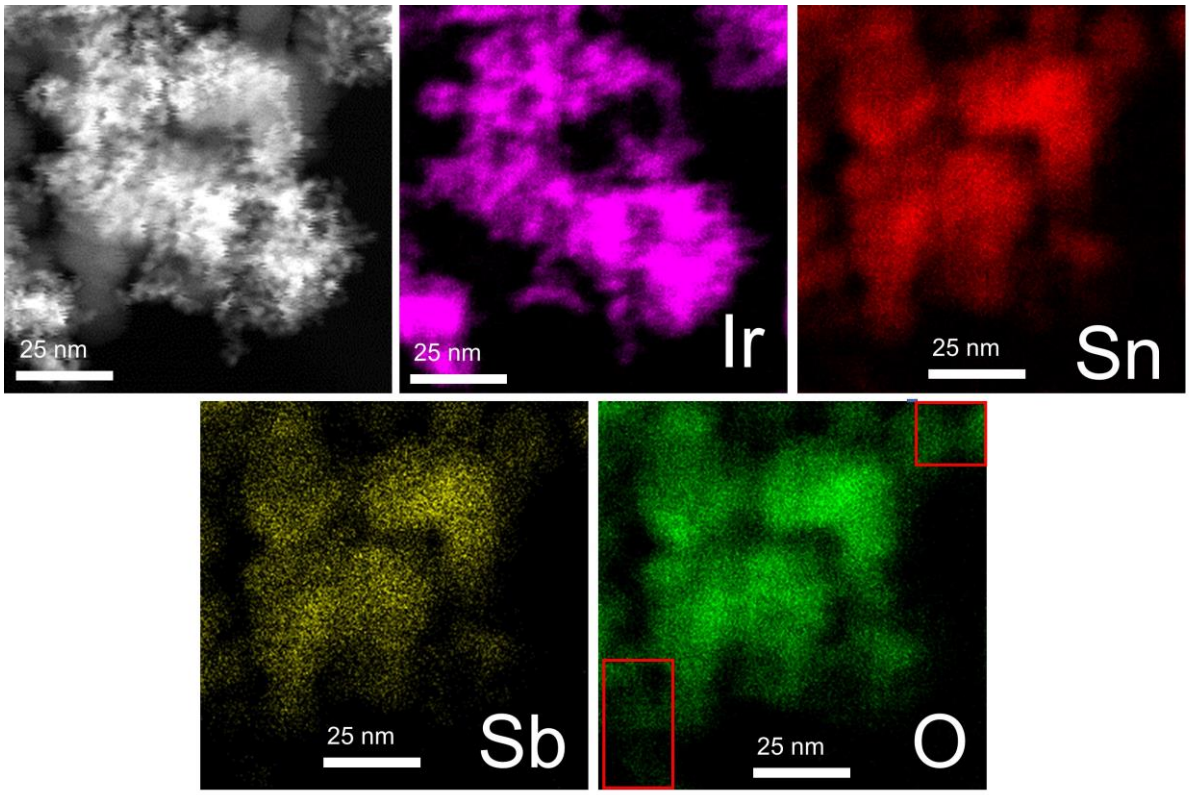

Fig. S60. Elemental mapping of Ir, Sn, Sb, and O in Ir-Sn PSC_OER.

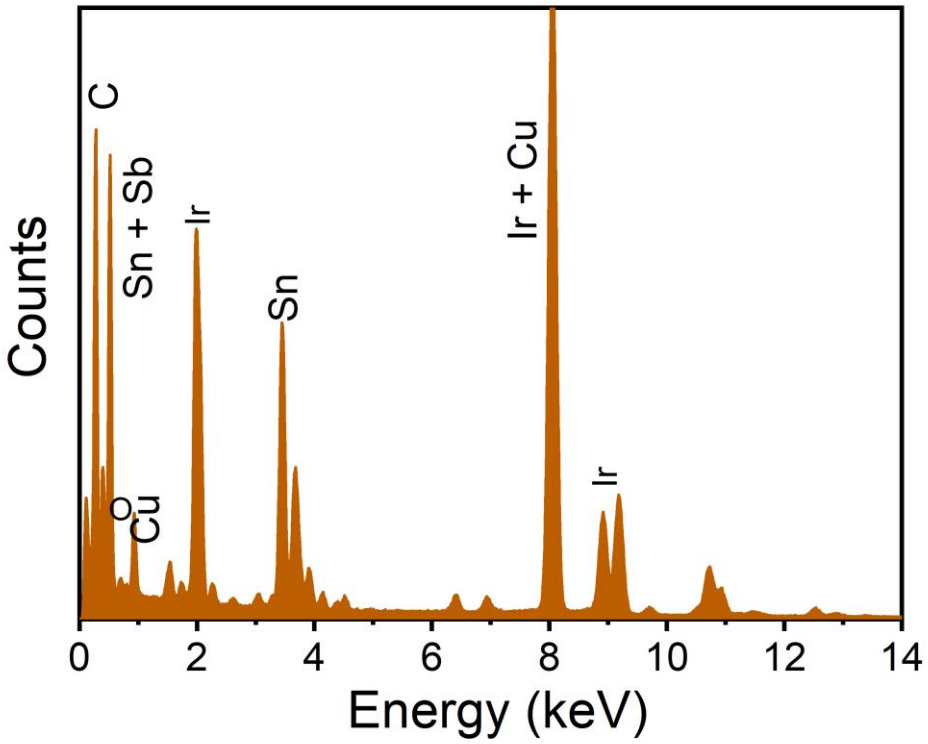

Fig. S61. EDS spectrum of Ir-Sn PSC_OER.

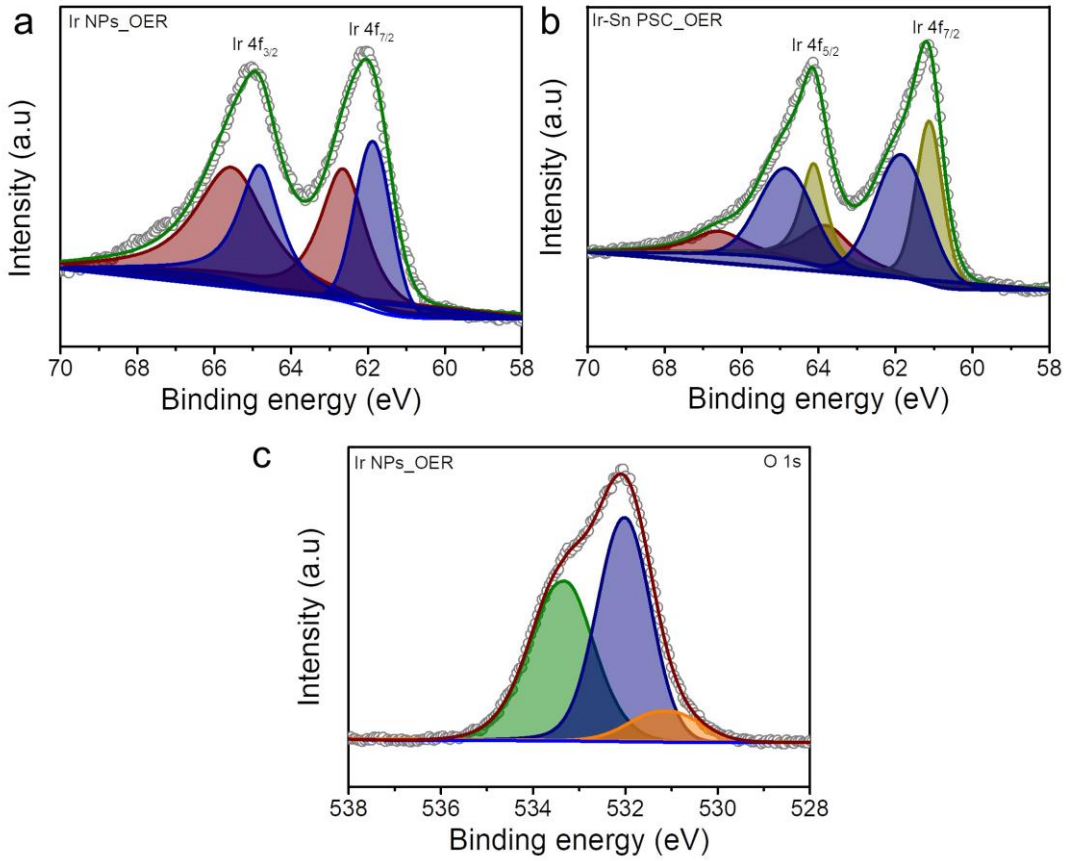

Fig. S62. High-resolution Ir 4f and O1s XPS spectra. (a) Ir 4f for NPs_OER. (b) Ir 4f for Ir-Sn PSC_OER. (c) O 1s for Ir NPs_OER.

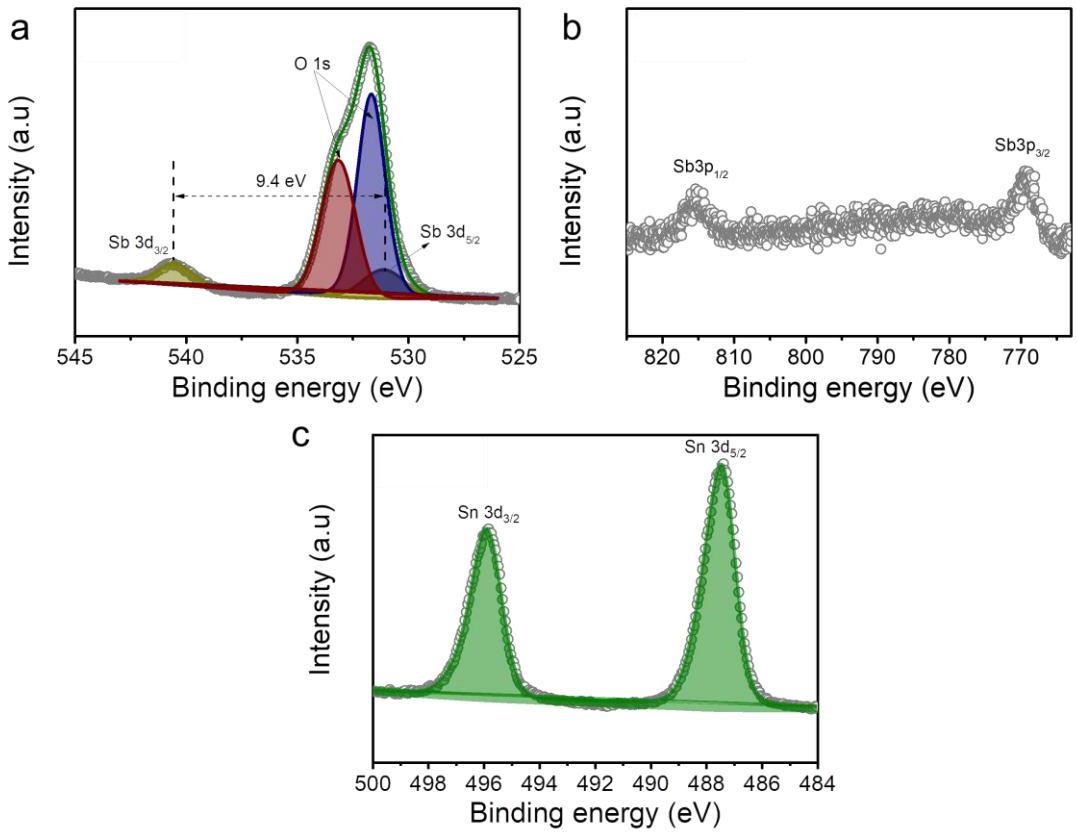

Fig. S63. High-resolution XPS spectra of Ir-Sn PSC_OER. (a) Sb 3d + O1s. (b) Sb 3p and (c) Sn 3d in Ir-Sn PSC_OER.

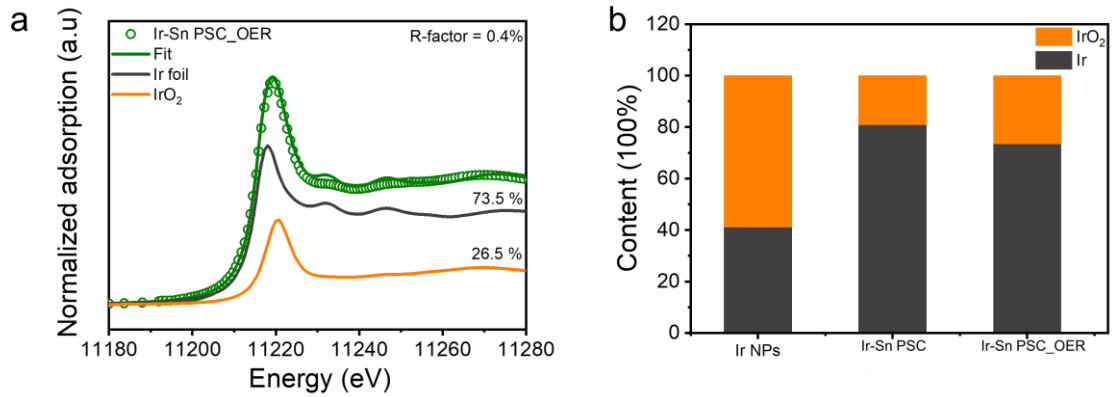

Fig. S64. Ir L_3-edge XANES spectra fitting result. (a) The L_3-edge XANES spectra fitting result of Ir-Sn PSC-OER. (b) Fitting content of Ir and IrO_2 in the Ir NPs, Ir-Sn PSC and Ir-Sn PSC_OER.

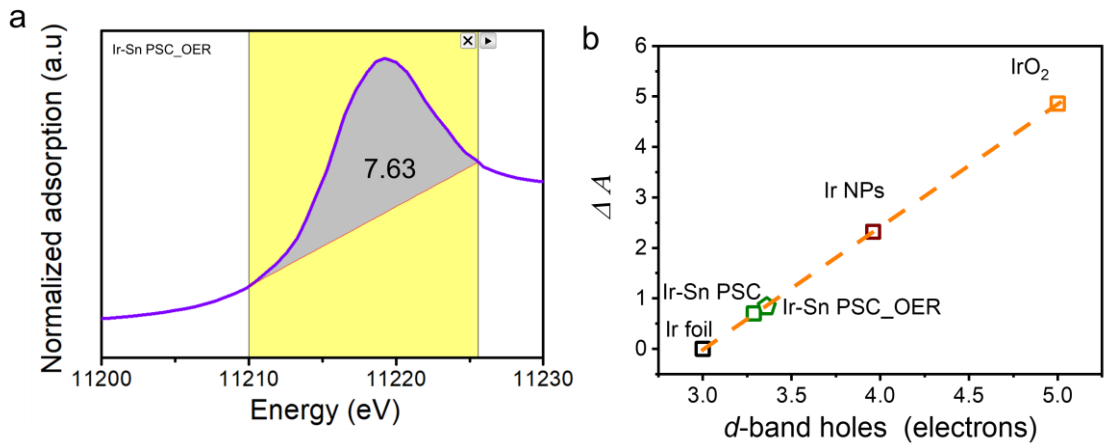

Fig. S65. Electronic structure of Ir-Sn PSC_OER. (a) White line peak area of Ir L_3-edge XANES for Ir-Sn PSC_OER. The peak area was calculated based on the integral area from the data range of 11210 to 11252.2 eV. (b) White line peak area difference as a function of the formal d-band hole count.

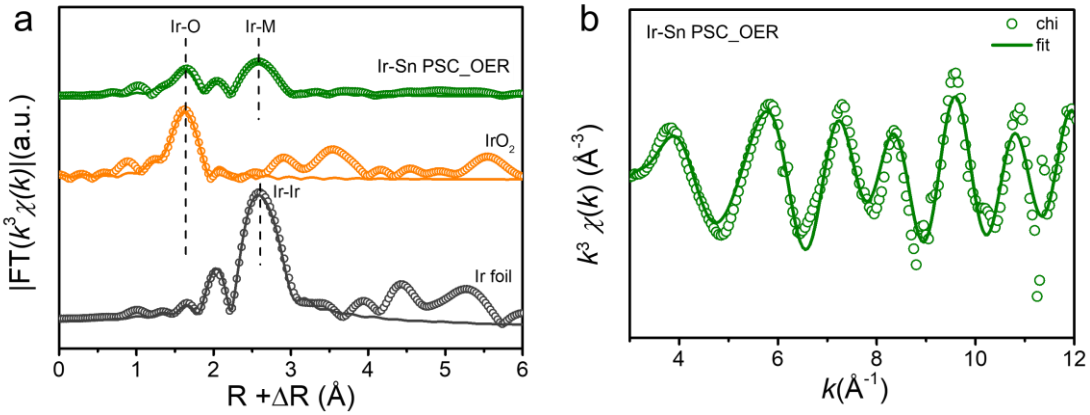

Fig. S66. Ir L_3-edge FT-EXAFS spectra of Ir foil, IrO_2, and Ir-Sn PSC_OER. (a) Ir L_3-edge EXAFS spectra (points) and curve-fits (lines) for Ir foil, IrO_2, and Ir-Sn PSC_OER, shown in *R* space. The data are k^3-weighted and not phase-corrected. (b) Ir L_3-edge EXAFS spectrum (points) and curve-fit (line) for Ir-Sn PSC_OER, shown in k^3-weighted *k*-space.

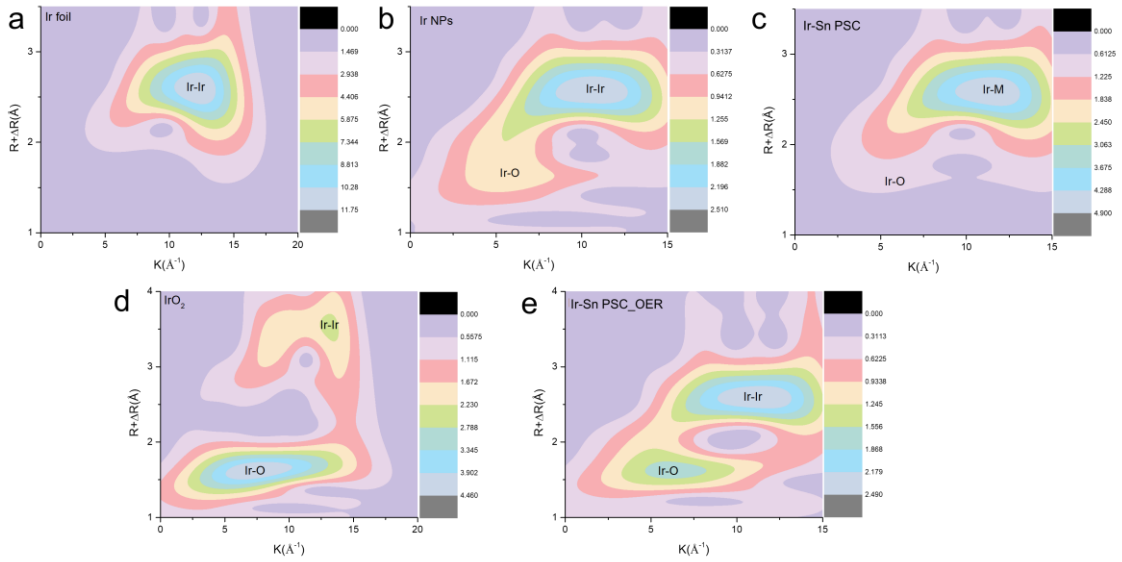

Fig. S67. WT-EXAFS plots of the Ir L_3-edge for different catalysts. (a) Ir foil, (b) Ir NPs, (c) Ir-Sn PSC, (d) IrO_2, (e) Ir-Sn PSC_OER.

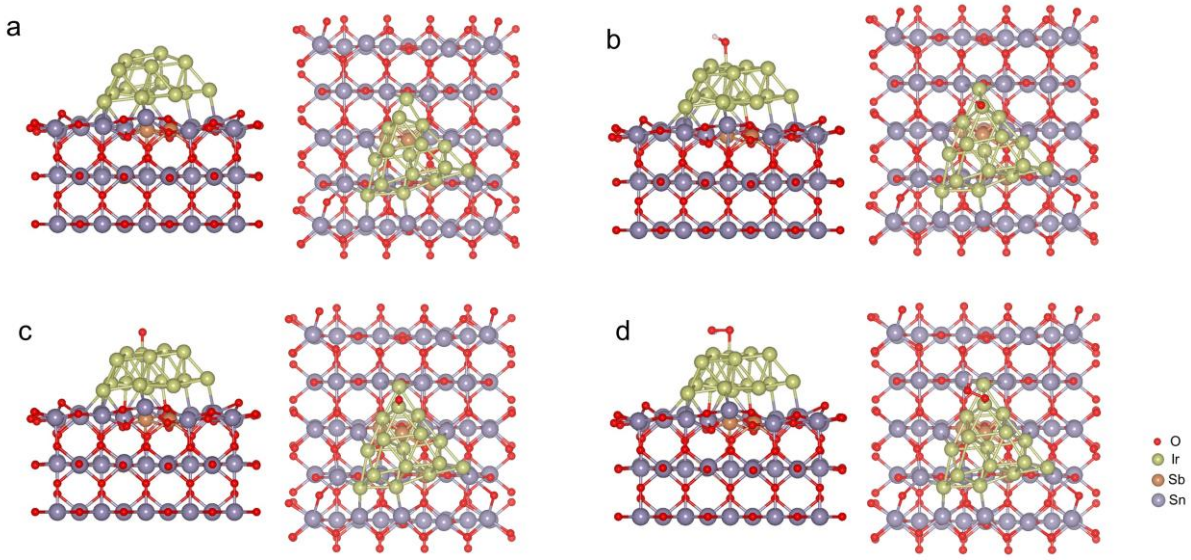

Fig. S68. Schematic illustration of Ir-Sn PSC after adsorbing different intermediates. Schematic illustration of (a) Ir-Sn PSC and Ir-Sn PSC with (b) OH*, (c) O*, and (d) OOH*.

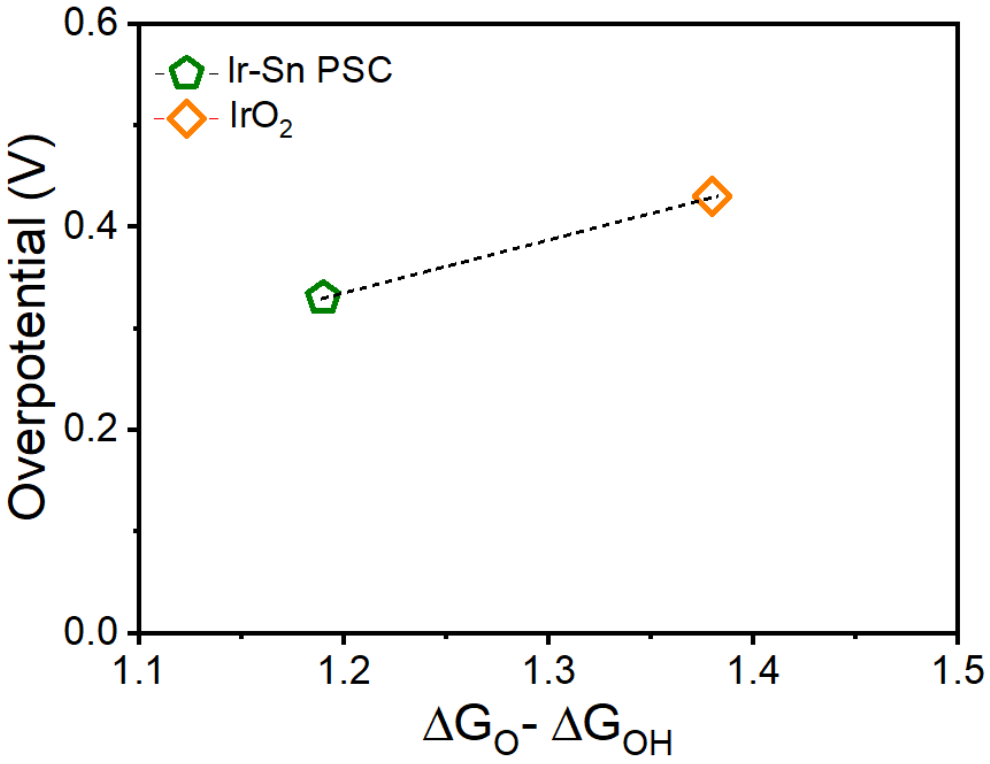

Fig. S69. Plot of the overpotential as a function of ΔG_O-ΔG_{OH} for IrO_2 and Ir-Sn PSC.

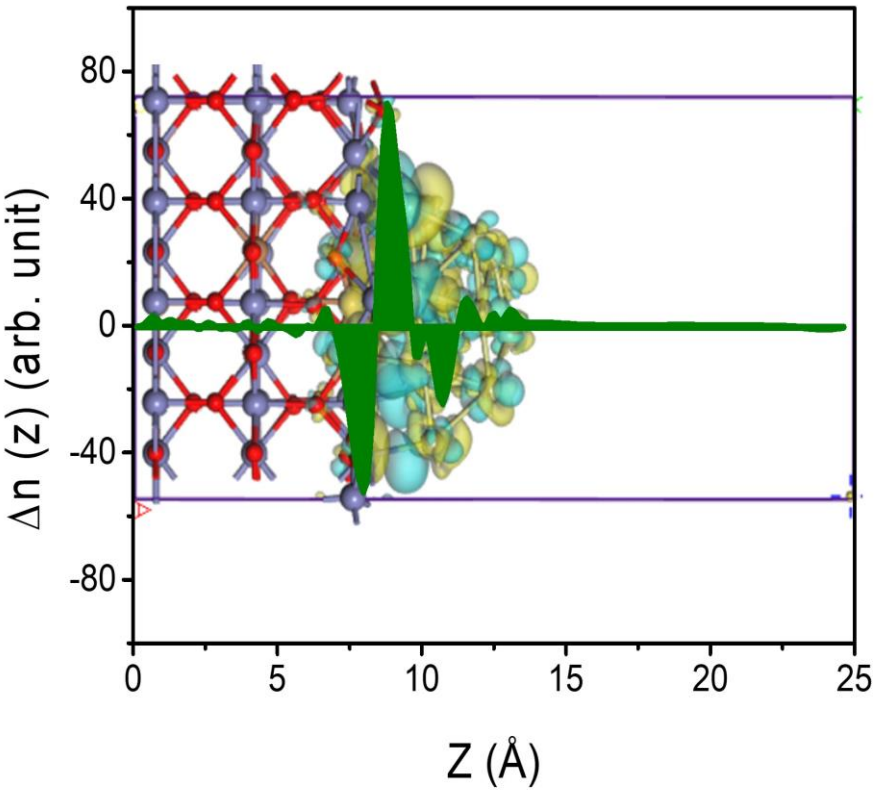

Fig. S70. Charge density difference of Ir-Sn PSC. The cyan and yellow isosurfaces show electron density accumulation and depletion, respectively. Variation in the averaged charge density difference in Ir-Sn PSC is shown along the direction perpendicular to the surface (along the z-axis).

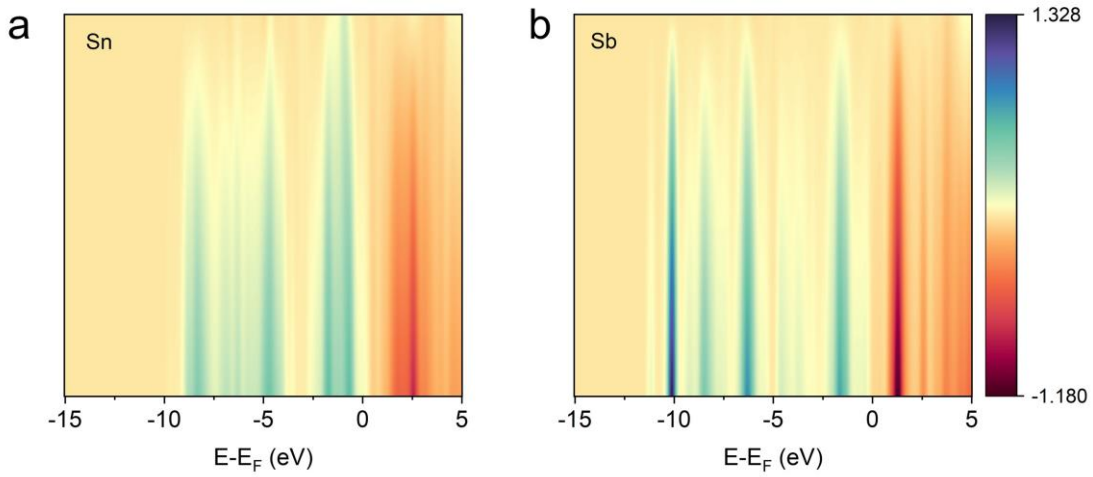

Fig. S71. The crystal orbital Hamilton population (COHP). COHP of the Ir atoms of different heights and both (a) the Sn atoms and (b) the Sb atoms on the surface of the Ir-Sn PSC.

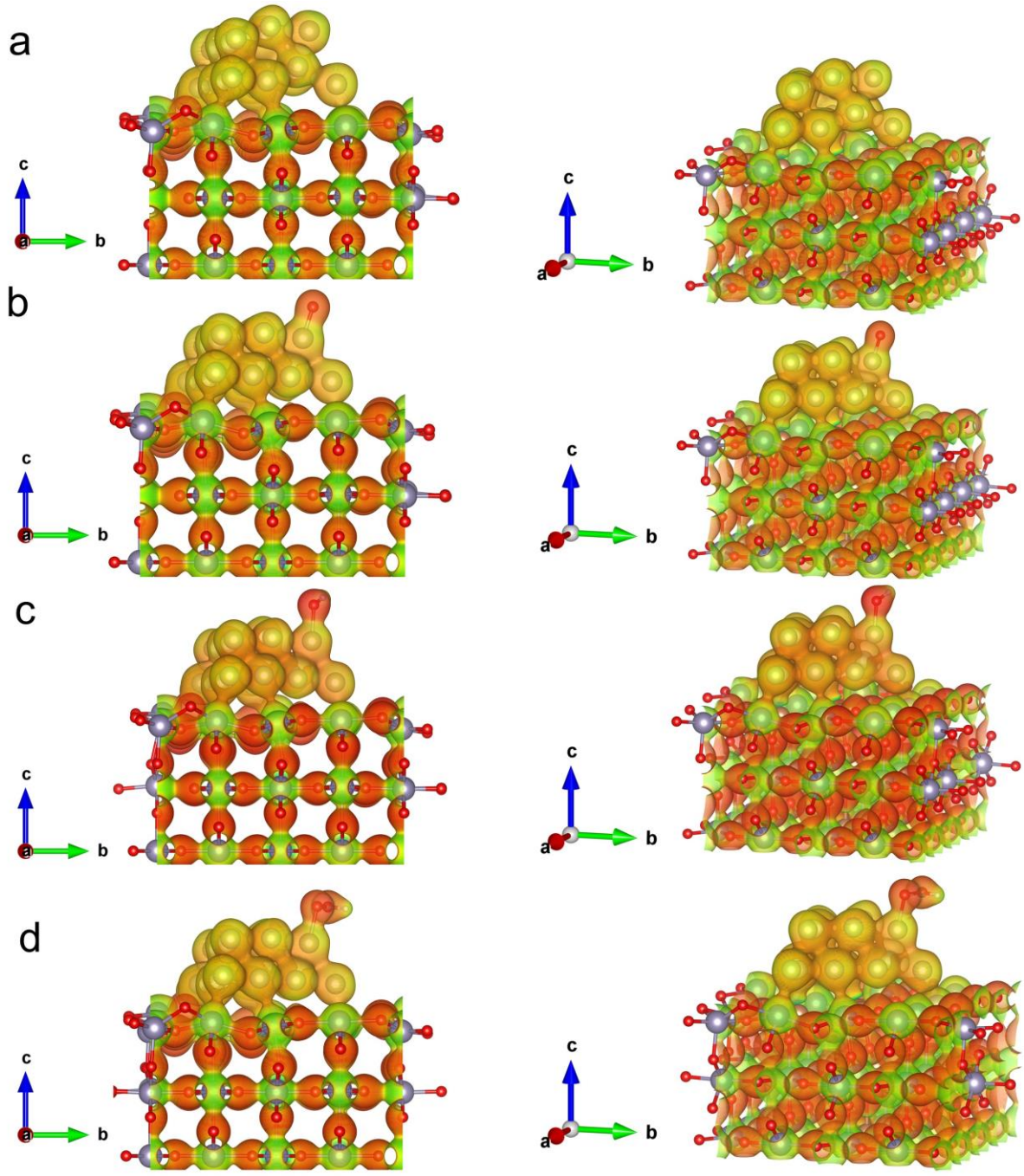

Fig. S72. Electrostatic potential. Electrostatic potential of (a) Ir-Sn PSC, (b) Ir-Sn PSC-O*, (c) Ir-Sn PSC-OH*, and (d) Ir-Sn PSC-OOH*.

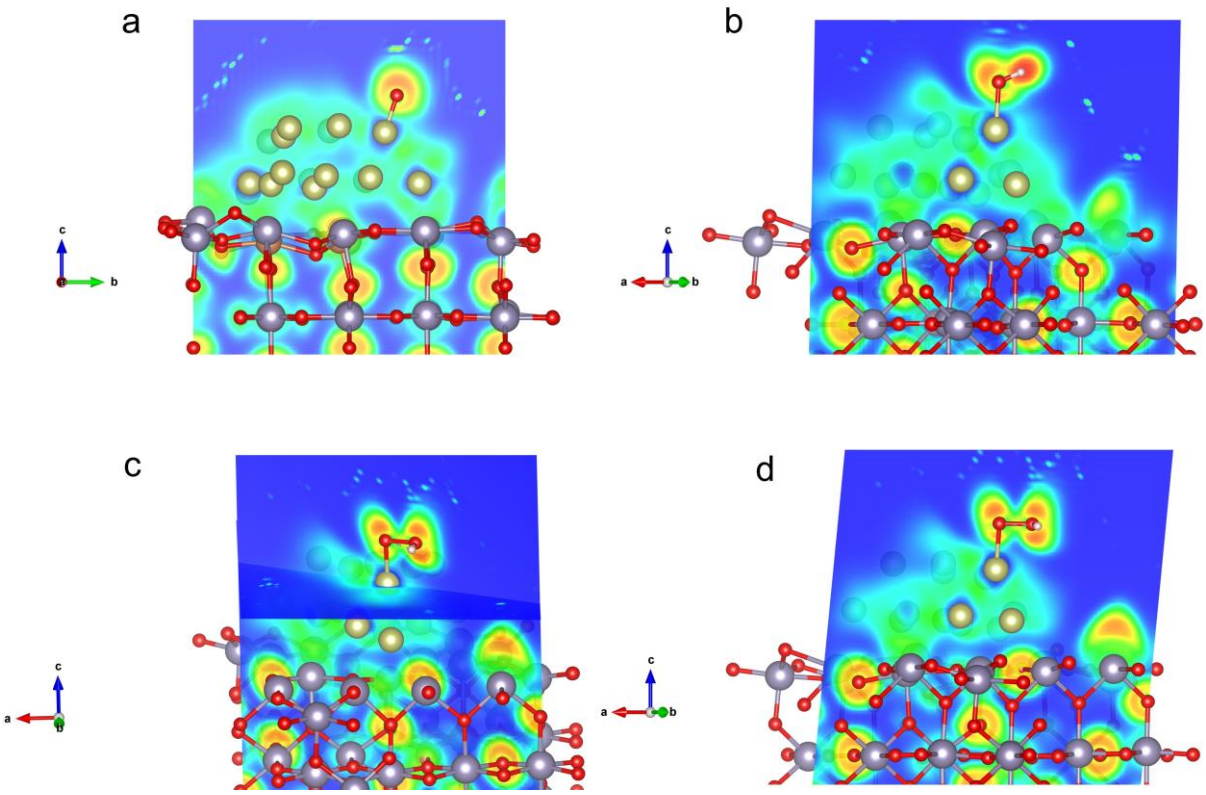

Fig. S73. The electron localization function (ELF). ELF of (a) Ir-Sn PSC-O*, (b) Ir-Sn PSC-OH*, and (c-d) Ir-Sn PSC-OOH*.

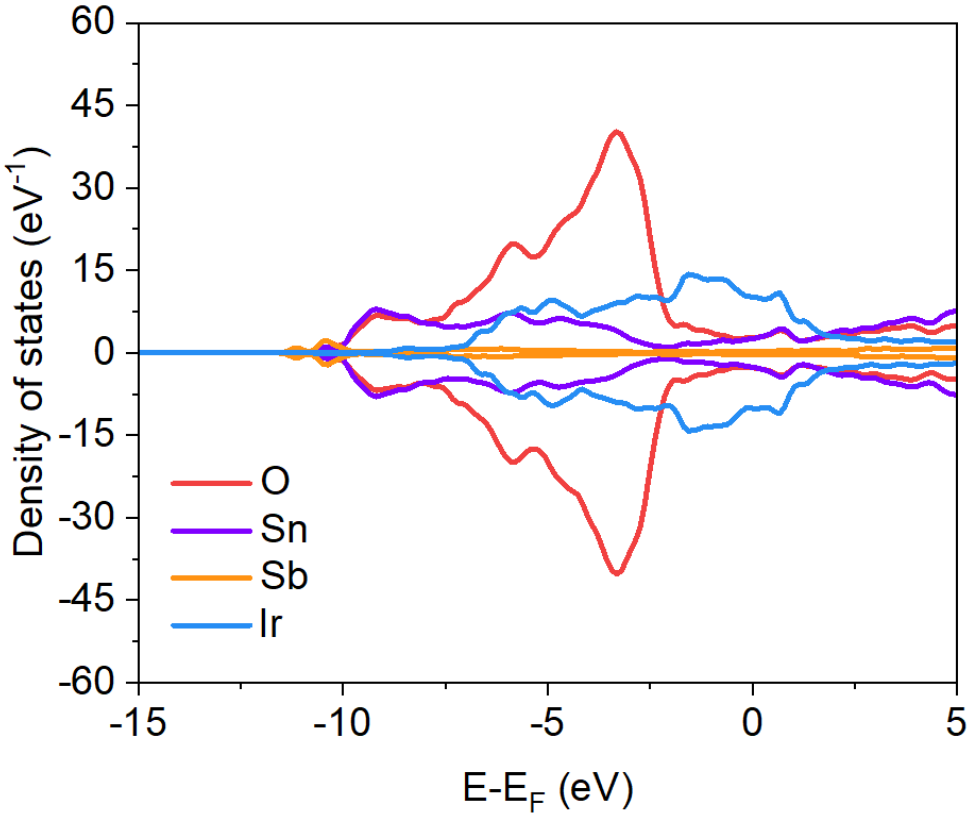

Fig. S74. DOS of Sn, Sb, Ir, and O in Ir-Sn PSC.

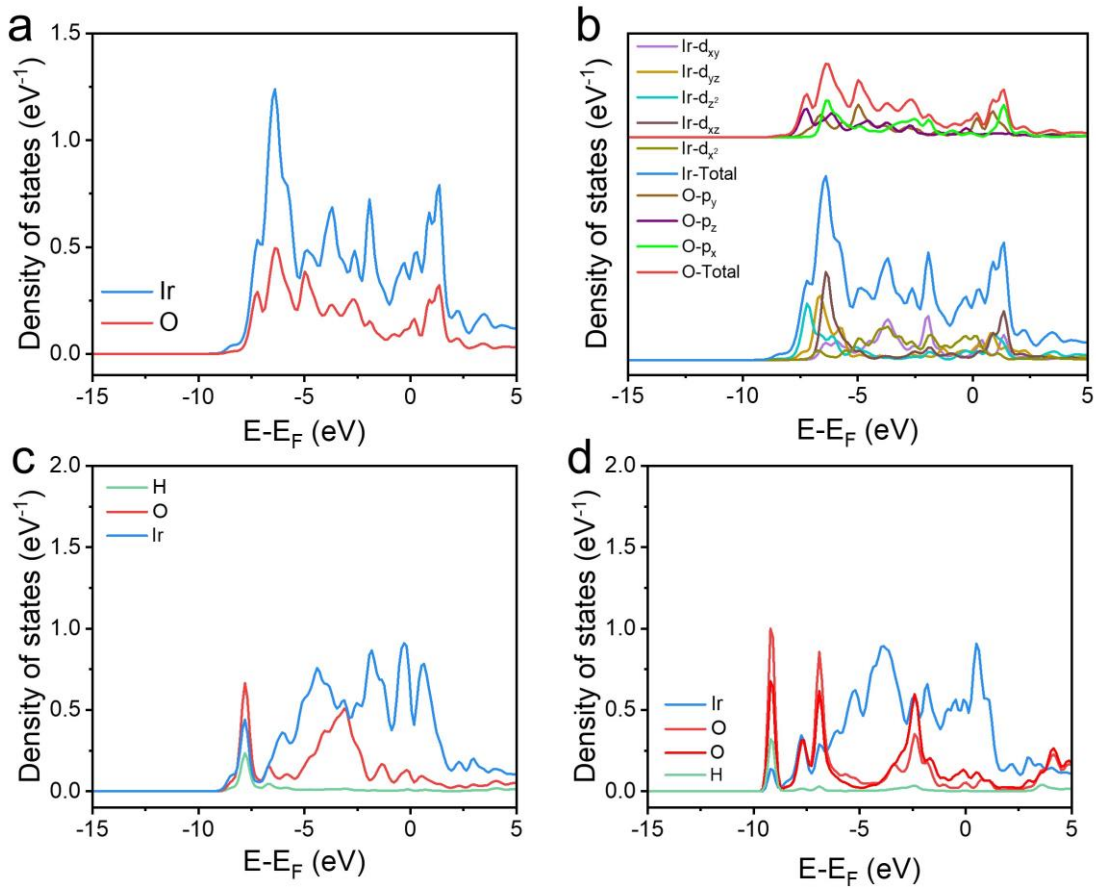

Fig. S75. DOS of Ir-Sn _PSC with different intermediates. (a) DOS of Ir orbitals and the adsorbed O orbitals. (b) The detailed projected density of states (PDOS) for the Ir *d* orbitals and O *p* orbitals. (c) DOS of Ir and the adsorbed OH intermediate. (d) DOS of Ir and the adsorbed OOH intermediate.

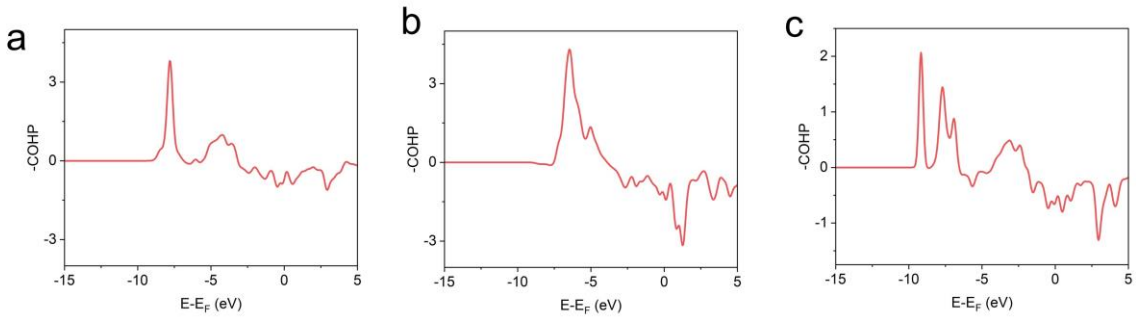

Fig. S76. The COHP between the active Ir site and O. (a) Ir-Sn PSC-O*, (b) Ir-Sn PSC-OH*, (c) Ir-Sn PSC-OOH*.

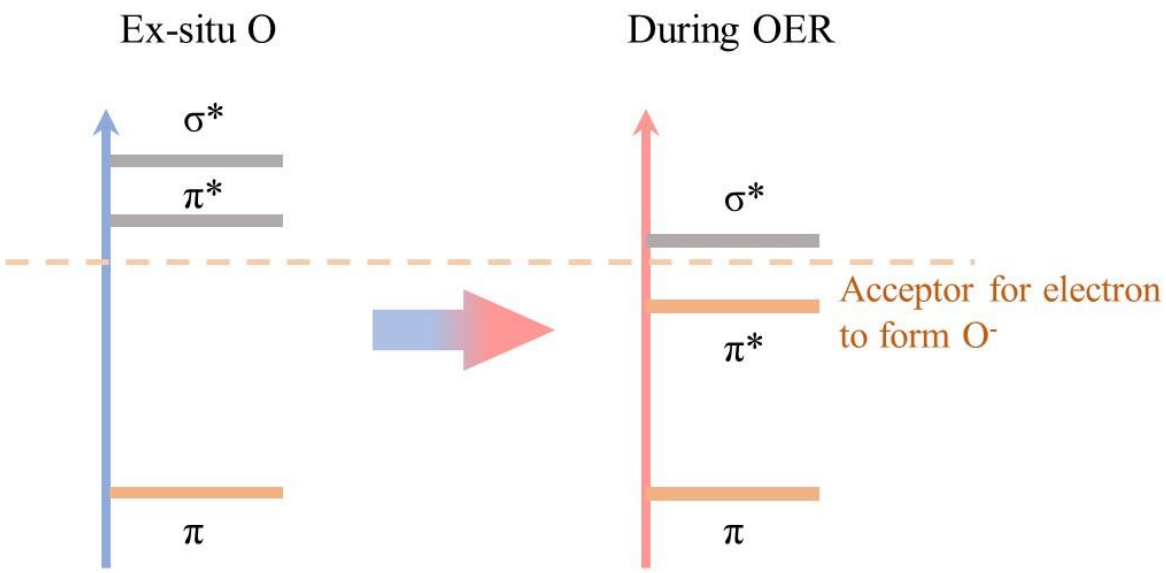

Fig. S77. Schematic illustration of the formation of an oxygen radical.

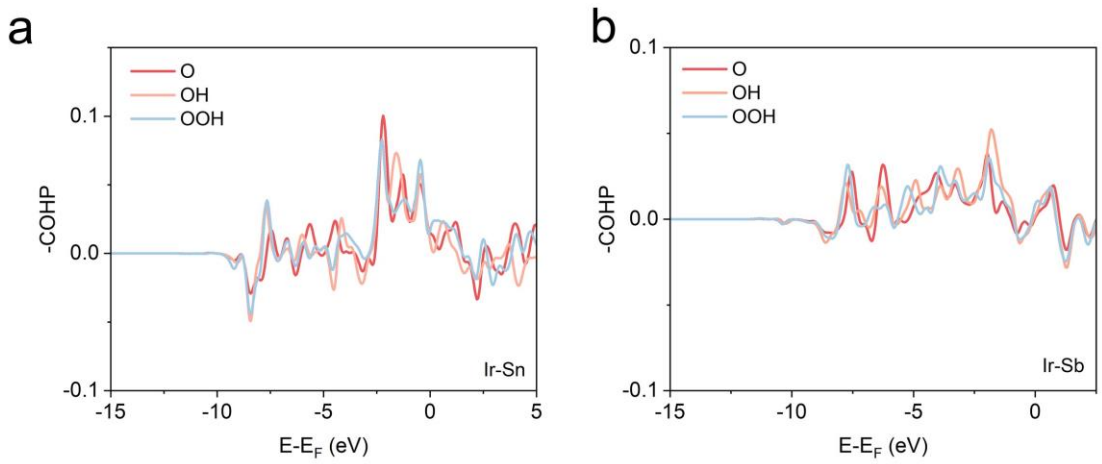

Fig. S78. The COHP evolution. The COHP evolution of (a) Ir-Sn and (b) Ir-Sb after the adsorption of O*, OH*, and OOH*.

Table S1. XPS fitting results for relative contents of valence states in the Ir NPs and Ir-Sn PSC catalyst.

Catalyst	Assignment	Position (eV)	Area	FWHM (eV)
Ir NPs	Ir(0) $4f_{7/2}$	61.1	3710.9	1.1
	Ir(0) $4f_{5/2}$	64.1	5454.1	1.1
	Ir(IV) $4f_{7/2}$	61.5	21215.5	0.8
	Ir(IV) $4f_{5/2}$	64.5	15911.6	0.8
	Ir(IV) $4f_{7/2}$ sat.	62.3	11985.4	1.3
	Ir(IV) $4f_{5/2}$ sat.	65.1	23432.3	1.9
Ir-Sn PSC	Ir(0) $4f_{7/2}$	61.1	11247.3	0.8
	Ir(0) $4f_{5/2}$	64.1	8435.5	0.8
	Ir(IV) $4f_{7/2}$	61.7	9061.4	1.7
	Ir(IV) $4f_{5/2}$	64.7	6796.1	1.7
	Ir(IV) $4f_{7/2}$ sat.	63.8	4696.7	1.4
	Ir(IV) $4f_{5/2}$ sat.	66.4	2128.5	1.6

Note: The Ir 4f XPS spectra were fitted with an energy splitting of 3.0 eV and the relative area ratio between Ir $4f_{7/2}$ and Ir $4f_{5/2}$ is 4:3. FWHM: full width at half maximum.

Table S2. The integrated white line area, average valence state, and the corresponding *d*-band holes of Ir in the various catalysts.

Catalyst	White line area	*d*-band holes
Ir foil	6.81	3
Ir NPs	9.12	3.96
Ir-Sn PSC	7.51	3.29
Ir-Sn PSC_OER	7.63	3.36
Cycled Ir-Sn PSC	10.1	4.32
IrO_2	11.66	5

Note: The white peak area was calculated based on the integral area from the data range of 11210 to 11252.2 eV of Ir L_3-edge XANES spectra.

Table S3. The linear combination fitting of Ir L_3-edge XANES spectra for the various catalysts based on the Ir foil and IrO_2 references.

Catalyst	Ir foil	IrO_2	Average valence state
Ir NPs	41.2	58.8	2.4
Ir-Sn PSC	80.9	19.1	0.8
Ir-Sn PSC_OER	73.5	36.5	1.1
Cycled Ir-Sn PSC	35.6	64.4	2.6

Table S4. EXAFS fitting parameters at the Ir L_3-edge for various samples.

	Shell	$N^{[a]}$	R (Å)$^{[b]}$	σ^2 (Å^2)$^{[c]}$	ΔE_0 (eV)$^{[d]}$	R factor
Ir foil	Ir-Ir	12	2.71 ± 0.002	0.003	8.9 ± 0.5	0.5%
IrO_2	Ir-O_1	2	1.90 ± 0.02	0.0 ± 0.002	9.9 ± 1.2	0.8%
	Ir-O_2	4	2.0 ± 0.01	0.0 ± 0.001		
Ir NPs	Ir-O	3.1 ± 0.5	1.98 ± 0.01	0.01 ± 0.003	8.0 ± 1.2	0.7%
	Ir-Ir	6.2 ± 0.6	2.69 ± 0.005	0.006 ± 0.0005		
Ir-Sn PSC	Ir-O	2.0 ± 0.6	1.99 ± 0.016	0.01 ± 0.006	8.3 ± 0.76	0.5%
	Ir-M	8.3 ± 0.6	2.70 ± 0.003	0.005 ± 0.0003		
Ir-Sn PSC_OER	Ir-O	2.3 ± 0.6	1.98 ± 0.012	0.003 ± 0.002	9.6	1.4%
	Ir-M	8.0 ± 1.5	2.70 ± 0.009	0.006 ± 0.001		
Cycled Ir-Sn PSC	Ir-O	4.3 ± 0.6	1.99 ± 0.006	0.005 ± 0.002	9.5	1.0%
	Ir-M	5.5 ± 1.4	2.69 ± 0.008	0.006 ± 0.002		

$^a N$: coordination numbers; $^b R$: bond distances; $^c \sigma^2$: Debye-Waller factors; $^d \Delta E_0$: the inner potential correction. R factor: goodness of fit. S_0^2 was set to 0.81 for Ir, according to the experimental EXAFS fit of Ir foil by fixing CN as the known crystallographic value. For Ir foil EXAFS fitting, the data ranges are presented as follows: $3.0 \leq k \leq 13.6$ Å^{-1}, $1.1 \leq R \leq 3.0$ Å. The independent point is 11.6 and the number of variables is 3. For IrO_2 foil EXAFS fitting, the data ranges are presented as follows: $3.0 \leq k \leq 13.6$ Å^{-1}, $1.0 \leq R \leq 2.4$ Å. The independent point is 9.3 and the number of variables is 5. For Ir NPs EXAFS fitting, the data ranges are presented as follows: $3.0 \leq k \leq 13.6$ Å^{-1}, $1.1 \leq R \leq 3.0$ Å. The independent point is 12.6 and the number of variables is 7. For the Ir-Sn PSC EXAFS fitting, the data ranges are presented as follows: $3.0 \leq k \leq 13.6$ Å^{-1}, $1.0 \leq R \leq 3.0$ Å. The independent point is 13.2, and the number of variables is 7. For the Ir-Sn PSC_OER EXAFS fitting, the data ranges are presented as follows: $2.3 \leq k \leq 14$ Å^{-1}, $1.2 \leq R \leq 3.0$ Å. The independent point is 13.0, and the number of variables is 8. For the cycled Ir-Sn PSC EXAFS fitting, the data ranges are presented as follows: $3.0 \leq k \leq 14$ Å^{-1}, $1.2 \leq R \leq 3.0$ Å. The independent point is 10.0, and the number of variables is 6.

Table S5. Detailed data on the acid OER performance of the Ir NPs, Ir-Sn PSC, and IrO_2 catalysts.

Catalyst	Mass activity at overpotential =320 mV (mA mg_{Ir}^{-1})	Overpotential at 10 mA cm^{-2} (mV)	Overpotential at 40 mA cm^{-2} (mV)	TOF at overpotential =300 mV (s^{-1})	Tafel slope (mV dec^{-1})
Ir NPs	254	235	303	0.09	79.5
Ir-Sn PSC	2913.8	200	250	1.06	64.1
IrO_2	28.5	372	584	0.01	142.4

Table S6. Comparison of Ir-Sn PSC catalyst with other reported representative OER catalysts under acidic conditions.

Catalyst	Electrolyte	Overpotential at 10 mA cm^{-2} (mV)	Mass activity (A mg_{Ir}^{-1})	Stability (h)	References
10.2% Ir-Sn PSC		225	4.427		
23.2% Ir-Sn PSC	0.5 M H_2SO_4	200	2.914	260	This work
38.3% Ir-Sn PSC		193	3.558		
$Rh_{22}Ir_{78}$	0.5 M H_2SO_4	292	1.17	2000 cycles	71
$IrO_x/SrIrO_3$	0.5 M H_2SO_4	270-290		20	5
$IrCo@IrO_x$	0.5 M H_2SO_4	247		8	72
Ir-STO	0.1 M $HClO_4$	247	0.82	20	24
$GB\text{-}Ta_{0.1}Tm_{0.1}Ir_{0.8}O_{2-\delta}$	0.5 M H_2SO_4	198	3.126	500	40
Ag_1/IrO_x	0.5 M H_2SO_4	224		3000 cycles	73
AD–HN–Ir	0.5 M H_2SO_4	216	2.860	100	56
$Ru_1\text{-}Pt_3Cu$	0.1 M $HClO_4$	220	0.779 mg^{-1}_{Ru+Pt}	28	23
$IrO_x/9R\text{-}BaIrO_3$	0.5 M H_2SO_4	230	0.168	48	53
$Ir_1@Fe@NCNT$	0.5 M H_2SO_4	250	13.7	12	74
$1T\text{-}IrO_2$	0.1 M $HClO_4$	197	0.2968	126	45
$Ir_1/NiCo_2O_4$	0.5 M H_2SO_4	240	10.0	70	50
La_2LiIrO_6	0.5 M H_2SO_4	350			33
Ba_2YIrO_6	0.1 M $HClO_4$	~390		1	75
IrO_2/GCN	0.5 M H_2SO_4	276	1.28	4	54
$W_{0.57}Ir_{0.43}O_{3-\delta}$	1 M H_2SO_4	370		0.6	76
Ir superstructures	0.1 M $HClO_4$	276		8	77
$Ir_{70}Ni_{15}Co_{15}$	0.1 M $HClO_4$	220		24	78
$Ru@IrO_x$	0.05 M H_2SO_4	282	0.645	24	49
IrO_2	1 M H_2SO_4	313	0.0516 mg^{-1}_{IrO2}	2	79
IrNiCu	0.1 M $HClO_4$	300	~0.46	2500 cycles	80
$6H\text{-}SrIrO_3$	0.5 M H_2SO_4	248	0.07	30	81
$IrHf_xO_y$	0.1 M $HClO_4$	330	6.95 mg^{-1}_{IrOx}	6	41
$Ir_{0.1}Ta_{0.9}O_{2.45}$	0.1 M $HClO_4$		1.2	24	20
$Ir\text{-}IrO_x/C\text{-}20$	0.5 M H_2SO_4	198		18	39

Table S7. Comparison of the PEMWE device performance using the Ir-Sn PSC with other OER catalysts.

Catalyst	Cell temperature	Cell voltage (V) at 1 A cm^{-2}	References
Ir-Sn PSC	80°C	1.548	This work
YBRO-0.15	60°C	1.64	82
$Ir_{0.7}Ru_{0.3}O_x$	80°C	1.7	83
$Ru_{0.7}Ir_{0.3}O_2$	80°C	1.586	84
$Ir_{0.6}Sn_{0.4}O_2$	80°C	1.7	85
$Ir_{0.6}Sn_{0.4}O_2$	80°C	1.665	86
$Ir_{0.2}Ru_{0.8}O_2$	80°C	1.622	87
Pt/IrO_2	60°C	1.81	88
GB-$Ta_{0.1}Tm_{0.1}Ir_{0.8}O_{2-\delta}$	50°C	1.766	40
IrO_2	80°C	1.65	89
Ir-ND	80°C	1.68	29

Table S8. XPS fitting results for relative contents of valence states in the Ir NPs and Ir-Sn PSC catalysts after OER cycling.

Catalyst	Assignment	Position (eV)	Area	FWHM (eV)
Ir NPs_OER	Ir(V) $4f_{7/2}$	61.8	876.2	1.1
	Ir(V) $4f_{5/2}$	64.8	1015.8	1.3
	Ir(V) $4f_{7/2}$ sat.	62.7	1229.4	1.4
	Ir(V) $4f_{5/2}$ sat.	64.5	1594.1	2.2
Ir-Sn PSC_OER	Ir(0) $4f_{7/2}$	61.1	2354.0	0.82
	Ir(0) $4f_{5/2}$	64.1	1765.5	0.8
	Ir(V) $4f_{7/2}$	61.8	3174.8	1.6
	Ir(V) $4f_{5/2}$	64.8	2381.1	1.7
	Ir(V) $4f_{7/2}$ sat.	63.8	1458.6	1.6
	Ir(V) $4f_{5/2}$ sat.	66.6	842.9	1.7
Cycled Ir-Sn	Ir(V) $4f_{7/2}$	62.5	3905.0	2.0
PSC	Ir(V) $4f_{5/2}$	65.5	2928.8	1.9
	Ir(V) $4f7_{/2}$ sat.	64.4	943.2	1.9
	Ir(V) $4f_{5/2}$ sat.	67.4	670.5	2.2

Note: The Ir 4f XPS spectra were fitted with an energy splitting of 3.0 eV, and the relative area ratio between Ir $4f_{7/2}$ and Ir $4f_{5/2}$ is 4:3.

Table S9. Calculated Gibbs free energy gaps for elementary steps in Ir-Sn PSC and IrO_2 catalysts at $U = 0$ and $U = 1.23$ V. U: potential under standard conditions vs. RHE.

Catalyst	ΔG_1 (eV)	ΔG_2 (eV)	ΔG_3 (eV)	ΔG_4 (eV)
Ir-Sn PSC (U = 0 V)	0.89	1.19	1.56	1.28
Ir-Sn PSC (U = 1.23 V)	-0.34	-0.04	0.33	0.05
IrO_2 (U = 0 V)	0.41	1.38	1.66	1.47
IrO_2 (U = 1.23 V)	-0.82	0.15	0.43	0.24

Table S10. Calculated Gibbs free energies of oxygen-related intermediates (*OH, *O, and *OOH) and theoretical overpotentials for Ir-Sn PSC and IrO_2 catalysts.

Catalyst	ΔG_{*OH} (eV)	ΔG_{*O} (eV)	ΔG_{*OOH} (eV)	Theoretical overpotential (V)
Ir-Sn PSC	0.89	2.08	3.64	0.33
IrO_2	0.41	1.79	3.45	0.43

REFERENCES AND NOTES

1. H. N. Nong, L. J. Falling, A. Bergmann, M. Klingenhof, H. P. Tran, C. Spori, R. Mom, J. Timoshenko, G. Zichittella, A. Knop-Gericke, S. Piccinin, J. Perez-Ramirez, B. R. Cuenya, R. Schlogl, P. Strasser, D. Teschner, T. E. Jones, Key role of chemistry versus bias in electrocatalytic oxygen evolution. *Nature* **587**, 408–413 (2020).

2. J. Hwang, R. R. Rao, L. Giordano, Y. Katayama, Y. Yu, Y. Shao-Horn, Perovskites in catalysis and electrocatalysis. *Science* **358**, 751–756 (2017).

3. J. Huang, H. Sheng, R. D. Ross, J. Han, X. Wang, B. Song, S. Jin, Modifying redox properties and local bonding of Co_3O_4 by CeO_2 enhances oxygen evolution catalysis in acid. *Nat. Commun.* **12**, 3036 (2021).

4. Y. Chen, H. Li, J. Wang, Y. Du, S. Xi, Y. Sun, M. Sherburne, J. W. Ager, III, A. C. Fisher, Z. J. Xu, Exceptionally active iridium evolved from a pseudo-cubic perovskite for oxygen evolution in acid. *Nat. Commun.* **10**, 572 (2019).

5. L. C. Seitz, C. F. Dickens, K. Nishio, Y. Hikita, J. Montoya, A. Doyle, C. Kirk, A. Vojvodic, H. Y. Hwang, J. K. Norskov, T. F. Jaramillo, A highly active and stable $IrO_x/SrIrO_3$ catalyst for the oxygen evolution reaction. *Science* **353**, 1011–1014 (2016).

6. X. Zheng, J. Yang, P. Li, Z. Jiang, P. Zhu, Q. Wang, J. Wu, E. Zhang, W. Sun, S. Dou, D. Wang, Y. Li, Dual-atom support boosts nickel-catalyzed urea Electrooxidation. *Angew. Chem. Int. Ed.* **62**, e202217449 (2023).

7. J. Kibsgaard, I. Chorkendorff, Considerations for the scaling-up of water splitting catalysts. *Nat. Energy* **4**, 430–433 (2019).

8. D. G. Li, E. J. Park, W. L. Zhu, Q. R. Shi, Y. Zhou, H. Y. Tian, Y. H. Lin, A. Serov, B. Zulevi, E. D. Baca, C. Fujimoto, H. T. Chung, Y. S. Kim, Highly quaternized polystyrene ionomers for high performance anion exchange membrane water electrolysers. *Nat. Energy* **5**, 378–385 (2020).

9. C. Lin, J.-L. Li, X. Li, S. Yang, W. Luo, Y. Zhang, S.-H. Kim, D.-H. Kim, S. S. Shinde, Y.-F. Li, Z.-P. Liu, Z. Jiang, J.-H. Lee, In-situ reconstructed Ru atom array on α-MnO_2 with enhanced performance for acidic water oxidation. *Nat. Catal.* **4**, 1012–1023 (2021).

10. S. Pan, H. Li, D. Liu, R. Huang, X. Pan, D. Ren, J. Li, M. Shakouri, Q. Zhang, M. Wang, C. Wei, L. Mai, B. Zhang, Y. Zhao, Z. Wang, M. Graetzel, X. Zhang, Efficient and stable noble-metal-free catalyst for acidic water oxidation. *Nat. Commun.* **13**, 2294 (2022).

11. X. B. Zheng, B. B. Li, Q. S. Wang, D. S. Wang, Y. D. Li, Emerging low-nuclearity supported metal catalysts with atomic level precision for efficient heterogeneous catalysis. *Nano Res.* **15**, 7806–7839 (2022).

12. J. T. Mefford, A. R. Akbashev, M. Kang, C. L. Bentley, W. E. Gent, H. D. Deng, D. H. Alsem, Y. S. Yu, N. J. Salmon, D. A. Shapiro, P. R. Unwin, W. C. Chueh, Correlative operando microscopy of oxygen evolution electrocatalysts. *Nature* **593**, 67–73 (2021).

13. B. Zhang, X. Zheng, O. Voznyy, R. Comin, M. Bajdich, M. Garcia-Melchor, L. Han, J. Xu, M. Liu, L. Zheng, F. P. Garcia de Arquer, C. T. Dinh, F. Fan, M. Yuan, E. Yassitepe, N. Chen, T. Regier, P. Liu, Y. Li, P. De Luna, A. Janmohamed, H. L. Xin, H. Yang, A. Vojvodic, E. H. Sargent, Homogeneously dispersed multimetal oxygen-evolving catalysts. *Science* **352**, 333–337 (2016).

14. N. Danilovic, R. Subbaraman, K. C. Chang, S. H. Chang, Y. Kang, J. Snyder, A. P. Paulikas, D. Strmcnik, Y. T. Kim, D. Myers, V. R. Stamenkovic, N. M. Markovic, Using surface segregation to design stable Ru-Ir oxides for the oxygen evolution reaction in acidic environments. *Angew. Chem. Int. Ed.* **53**, 14016–14021 (2014).

15. X. Zheng, J. Yang, Z. Xu, Q. Wang, J. Wu, E. Zhang, S. Dou, W. Sun, D. Wang, Y. Li, Ru-Co pair sites catalyst boosts the energetics for the oxygen evolution reaction. *Angew. Chem. Int. Ed.* **61**, e202205946 (2022).

16. S. Li, B. Chen, Y. Wang, M. Y. Ye, P. A. van Aken, C. Cheng, A. Thomas, Oxygen-evolving catalytic atoms on metal carbides. *Nat. Mater.* **20**, 1240–1247 (2021).

17. Y. Lin, Z. Tian, L. Zhang, J. Ma, Z. Jiang, B. J. Deibert, R. Ge, L. Chen, Chromium-ruthenium oxide solid solution electrocatalyst for highly efficient oxygen evolution reaction in acidic media. *Nat. Commun.* **10**, 162 (2019).

18. A. Li, H. Ooka, N. Bonnet, T. Hayashi, Y. Sun, Q. Jiang, C. Li, H. Han, R. Nakamura, Stable potential windows for long-term electrocatalysis by manganese oxides under acidic conditions. *Angew. Chem. Int. Ed.* **58**, 5054–5058 (2019).

19. O. Kasian, J. P. Grote, S. Geiger, S. Cherevko, K. J. J. Mayrhofer, The common intermediates of oxygen evolution and dissolution reactions during water electrolysis on iridium. *Angew. Chem. Int. Ed.* **57**, 2488–2491 (2018).

20. Y.-R. Zheng, J. Vernieres, Z. Wang, K. Zhang, D. Hochfilzer, K. Krempl, T.-W. Liao, F. Presel, T. Altantzis, J. Fatermans, S. B. Scott, N. M. Secher, C. Moon, P. Liu, S. Bals, S. Van Aert, A. Cao, M. Anand, J. K. Nørskov, J. Kibsgaard, I. Chorkendorff, Monitoring oxygen production on mass-selected iridium–tantalum oxide electrocatalysts. *Nat. Energy* **7**, 55–64 (2022).

21. A. L. Li, S. Kong, C. X. Guo, H. Ooka, K. Adachi, D. Hashizume, Q. K. Jiang, H. X. Han, J. P. Xiao, R. Nakamura, Enhancing the stability of cobalt spinel oxide towards sustainable oxygen evolution in acid. *Nat. Catal.* **5**, 109–118 (2022).

22. X. Liu, S. Xi, H. Kim, A. Kumar, J. Lee, J. Wang, N. Q. Tran, T. Yang, X. Shao, M. Liang, M. G. Kim, H. Lee, Restructuring highly electron-deficient metal-metal oxides for boosting stability in acidic oxygen evolution reaction. *Nat. Commun.* **12**, 5676 (2021).

23. Y. Yao, S. Hu, W. Chen, Z.-Q. Huang, W. Wei, T. Yao, R. Liu, K. Zang, X. Wang, G. Wu, W. Yuan, T. Yuan, B. Zhu, W. Liu, Z. Li, D. He, Z. Xue, Y. Wang, X. Zheng, J. Dong, C.-R. Chang, Y. Chen, X. Hong, J. Luo, S. Wei, W.-X. Li, P. Strasser, Y. Wu, Y. Li, Engineering the electronic structure of single atom Ru sites via compressive strain boosts acidic water oxidation electrocatalysis. *Nat. Catal.* **2**, 304–313 (2019).

24. X. Liang, L. Shi, Y. Liu, H. Chen, R. Si, W. Yan, Q. Zhang, G. D. Li, L. Yang, X. Zou, Activating inert, nonprecious perovskites with iridium dopants for efficient oxygen evolution reaction under acidic conditions. *Angew. Chem. Int. Ed.* **58**, 7631–7635 (2019).

25. G. T. K. K. Gunasooriya, J. K. Nørskov, Analysis of acid-stable and active oxides for the oxygen evolution reaction. *ACS Energy Lett.*, **5**, 3778–3787 (2020).

26. Z. Wang, Y.-R. Zheng, I. Chorkendorff, J. K. Nørskov, Acid-stable oxides for oxygen electrocatalysis. *ACS Energy Lett.* **5**, 2905–2908 (2020).

27. H. S. Oh, H. N. Nong, T. Reier, A. Bergmann, M. Gliech, J. Ferreira de Araujo, E. Willinger, R. Schlogl, D. Teschner, P. Strasser, Electrochemical catalyst-support effects and their stabilizing role for IrO_x nanoparticle catalysts during the oxygen evolution reaction. *J. Am. Chem. Soc.* **138**, 12552–12563 (2016).

28. H. N. Nong, H. S. Oh, T. Reier, E. Willinger, M. G. Willinger, V. Petkov, D. Teschner, P. Strasser, Oxide-supported IrNiOxCore–Shell particles as efficient, cost-effective, and stable catalysts for electrochemical water splitting. *Angew. Chem. Int. Ed.* **54**, 2975–2979 (2015).

29. H. S. Oh, H. N. Nong, T. Reier, M. Gliech, P. Strasser, Oxide-supported Ir nanodendrites with high activity and durability for the oxygen evolution reaction in acid PEM water electrolyzers. *Chem. Sci.* **6**, 3321–3328 (2015).

30. D. Böhm, M. Beetz, M. Schuster, K. Peters, A. G. Hufnagel, M. Döblinger, B. Böller, T. Bein, D. Fattakhova-Rohlfing, Efficient OER catalyst with low Ir volume density obtained by homogeneous deposition of iridium oxide nanoparticles on macroporous antimony-doped Tin oxide support. *Adv. Funct. Mater.* **30**, 1906670 (2019).

31. R. Z. Li, D. S. Wang, Understanding the structure-performance relationship of active sites at atomic scale. *Nano Res.* **15**, 6888–6923 (2022).

32. C. Ling, L. Q. Zhou, H. F. Jia, First-principles study of crystalline $CoWO_4$ as oxygen evolution reaction catalyst. *RSC Adv.* **4**, 24692–24697 (2014).

33. A. Grimaud, A. Demortière, M. Saubanère, W. Dachraoui, M. Duchamp, M.-L. Doublet, J.-M. Tarascon, Activation of surface oxygen sites on an iridium-based model catalyst for the oxygen evolution reaction. *Nat. Energy* **2**, 16189 (2017).

34. F. T. Haase, A. Bergmann, T. E. Jones, J. Timoshenko, A. Herzog, H. S. Jeon, C. Rettenmaier, B. R. Cuenya, Size effects and active state formation of cobalt oxide nanoparticles during the oxygen evolution reaction. *Nat. Energy* **7**, 765–773 (2022).

35. A. Hartig-Weiss, M. Miller, H. Beyer, A. Schmitt, A. Siebel, A. T. S. Freiberg, H. A. Gasteiger, H. A. El-Sayed, Iridium oxide catalyst supported on antimony-doped Tin oxide for high oxygen evolution reaction activity in acidic media. *ACS Appl. Nano Mater.* **3**, 2185–2196 (2020).

36. G. Zhao, P. Li, N. Cheng, S. X. Dou, W. Sun, An Ir/$Ni(OH)_2$ heterostructured electrocatalyst for the oxygen evolution reaction: Breaking the scaling relation, stabilizing iridium(V), and beyond. *Adv. Mater.* **32**, e2000872 (2020).

37. H. Wang, Z. N. Chen, D. Wu, M. Cao, F. Sun, H. Zhang, H. You, W. Zhuang, R. Cao, Significantly enhanced overall water splitting performance by partial oxidation of Ir through Au modification in core-shell alloy structure. *J. Am. Chem. Soc.* **143**, 4639–4645 (2021).

38. R. Li, H. Wang, F. Hu, K. C. Chan, X. Liu, Z. Lu, J. Wang, Z. Li, L. Zeng, Y. Li, X. Wu, Y. Xiong, IrW nanochannel support enabling ultrastable electrocatalytic oxygen evolution at 2 A cm^{-2} in acidic media. *Nat. Commun.* **12**, 3540 (2021).

39. L. Zu, X. Qian, S. Zhao, Q. Liang, Y. E. Chen, M. Liu, B. J. Su, K. H. Wu, L. Qu, L. Duan, H. Zhan, J. Y. Zhang, C. Li, W. Li, J. Y. Juang, J. Zhu, D. Li, A. Yu, D. Zhao, Self-assembly of Ir-based nanosheets with ordered interlayer space for enhanced electrocatalytic water oxidation. *J. Am. Chem. Soc.* **144**, 2208–2217 (2022).

40. S. Hao, H. Sheng, M. Liu, J. Huang, G. Zheng, F. Zhang, X. Liu, Z. Su, J. Hu, Y. Qian, L. Zhou, Y. He, B. Song, L. Lei, X. Zhang, S. Jin, Torsion strained iridium oxide for efficient acidic water oxidation in proton exchange membrane electrolyzers. *Nat. Nanotechnol.* **16**, 1371–1377 (2021).

41. F. Zhao, B. Wen, W. Niu, Z. Chen, C. Yan, A. Selloni, C. G. Tully, X. Yang, B. E. Koel, Increasing iridium oxide activity for the oxygen evolution reaction with hafnium modification. *J. Am. Chem. Soc.* **143**, 15616–15623 (2021).

42. F. Luo, A. Roy, L. Silvioli, D. A. Cullen, A. Zitolo, M. T. Sougrati, I. C. Oguz, T. Mineva, D. Teschner, S. Wagner, J. Wen, F. Dionigi, U. I. Kramm, J. Rossmeisl, F. Jaouen, P. Strasser, P-block single-metal-site tin/nitrogen-doped carbon fuel cell cathode catalyst for oxygen reduction reaction. *Nat. Mater.* **19**, 1215–1223 (2020).

43. Z. Jiang, T. Wang, J. Pei, H. Shang, D. Zhou, H. Li, J. Dong, Y. Wang, R. Cao, Z. Zhuang, W. Chen, D. Wang, J. Zhang, Y. Li, Discovery of main group single Sb–N4active sites for CO_2 electroreduction to formate with high efficiency. *Energ. Environ. Sci.* **13**, 2856–2863 (2020).

44. Z. L. Fan, Y. J. Ji, Q. Shao, S. Z. Geng, W. X. Zhu, Y. Liu, F. Liao, Z. W. Hu, Y. C. Chang, C. W. Pao, Y. Y. Li, Z. H. Kang, M. W. Shao, Extraordinary acidic oxygen evolution on new phase 3R-iridium oxide. *Joule* **5**, 3221–3234 (2021).

45. Q. Dang, H. Lin, Z. Fan, L. Ma, Q. Shao, Y. Ji, F. Zheng, S. Geng, S. Z. Yang, N. Kong, W. Zhu, Y. Li, F. Liao, X. Huang, M. Shao, Iridium metallene oxide for acidic oxygen evolution catalysis. *Nat. Commun.* **12**, 6007 (2021).

46. Z. Shi, Y. Wang, J. Li, X. Wang, Y. Wang, Y. Li, W. Xu, Z. Jiang, C. Liu, W. Xing, J. Ge, Confined Ir single sites with triggered lattice oxygen redox: Toward boosted and sustained water oxidation catalysis. *Joule* **5**, 2164–2176 (2021).

47. W. H. Lee, Y. J. Ko, J. H. Kim, C. H. Choi, K. H. Chae, H. Kim, Y. J. Hwang, B. K. Min, P. Strasser, H. S. Oh, High crystallinity design of Ir-based catalysts drives catalytic reversibility for water electrolysis and fuel cells. *Nat. Commun.* **12**, 4271 (2021).

48. H. N. Nong, T. Reier, H.-S. Oh, M. Gliech, P. Paciok, T. H. T. Vu, D. Teschner, M. Heggen, V. Petkov, R. Schlögl, T. Jones, P. Strasser, A unique oxygen ligand environment facilitates water oxidation in hole-doped IrNiOx core–shell electrocatalysts. *Nat. Catal.* **1**, 841–851 (2018).

49. J. Shan, C. Guo, Y. Zhu, S. Chen, L. Song, M. Jaroniec, Y. Zheng, S.-Z. Qiao, Charge-redistribution-enhanced nanocrystalline Ru@IrO*x* electrocatalysts for oxygen evolution in acidic media. *Chem* **5**, 445–459 (2019).

50. J. Yin, J. Jin, M. Lu, B. Huang, H. Zhang, Y. Peng, P. Xi, C. H. Yan, Iridium single atoms coupling with oxygen vacancies boosts oxygen evolution reaction in acid media. *J. Am. Chem. Soc.* **142**, 18378–18386 (2020).

51. Q. Shi, Y. Ji, W. Chen, Y. Zhu, J. Li, H. Liu, Z. Li, S. Tian, L. Wang, Z. Zhong, L. Wang, J. Ma, Y. Li, F. Su, Single-atom Sn-Zn pairs in CuO catalyst promote dimethyldichlorosilane synthesis. *Natl. Sci. Rev.* **7**, 600–608 (2020).

52. A. Dutta, A. Kuzume, V. Kaliginedi, M. Rahaman, I. Sinev, M. Ahmadi, B. Roldán Cuenya, S. Vesztergom, P. Broekmann, Probing the chemical state of tin oxide NP catalysts during CO_2 electroreduction: A complementary operando approach. *Nano Energy* **53**, 828–840 (2018).

53. N. Li, L. Cai, C. Wang, Y. Lin, J. Huang, H. Sheng, H. Pan, W. Zhang, Q. Ji, H. Duan, W. Hu, W. Zhang, F. Hu, H. Tan, Z. Sun, B. Song, S. Jin, W. Yan, Identification of the active-layer structures for acidic oxygen evolution from 9R-$BaIrO_3$ electrocatalyst with enhanced iridium mass activity. *J. Am. Chem. Soc.* **143**, 18001–18009 (2021).

54. J. Chen, P. Cui, G. Zhao, K. Rui, M. Lao, Y. Chen, X. Zheng, Y. Jiang, H. Pan, S. X. Dou, W. Sun, Low-coordinate iridium oxide confined on graphitic carbon nitride for highly efficient oxygen evolution. *Angew. Chem. Int. Ed.* **58**, 12540–12544 (2019).

55. J. J. Velasco-Velez, E. A. Carbonio, C. H. Chuang, C. J. Hsu, J. F. Lee, R. Arrigo, M. Havecker, R. Wang, M. Plodinec, F. R. Wang, A. Centeno, A. Zurutuza, L. J. Falling, R. V. Mom, S. Hofmann, R. Schlogl, A. Knop-Gericke, T. E. Jones, Surface electron-hole rich species active in the electrocatalytic water oxidation. *J. Am. Chem. Soc.* **143**, 12524–12534 (2021).

56. H. Su, W. Zhou, W. Zhou, Y. Li, L. Zheng, H. Zhang, M. Liu, X. Zhang, X. Sun, Y. Xu, F. Hu, J. Zhang, T. Hu, Q. Liu, S. Wei, In-situ spectroscopic observation of dynamic-coupling oxygen on atomically dispersed iridium electrocatalyst for acidic water oxidation. *Nat. Commun.* **12**, 6118 (2021).

57. Z. Shi, J. Li, J. Jiang, Y. Wang, X. Wang, Y. Li, L. Yang, Y. Chu, J. Bai, J. Yang, J. Ni, Y. Wang, L. Zhang, Z. Jiang, C. Liu, J. Ge, W. Xing, Enhanced acidic water oxidation by dynamic migration of oxygen species at the Ir/Nb_2O_{5-x} catalyst/support interfaces. *Angew. Chem. Int. Ed.* **61**, e202212341 (2022).

58. J. Liu, D. Xie, X. Xu, L. Jiang, R. Si, W. Shi, P. Cheng, Reversible formation of coordination bonds in Sn-based metal-organic frameworks for high-performance lithium storage. *Nat. Commun.* **12**, 3131 (2021).

59. M. Desmau, M. A. Alsina, J.-F. Gaillard, XAS study of Sn speciation in toothpaste. *J. Anal. At. Spectrom* **36**, 407–415 (2021).

60. V. A. Saveleva, K. Ebner, L. Ni, G. Smolentsev, D. Klose, A. Zitolo, E. Marelli, J. Li, M. Medarde, O. V. Safonova, M. Nachtegaal, F. Jaouen, U. I. Kramm, T. J. Schmidt, J. Herranz, Potential-induced spin changes in Fe/N/C electrocatalysts assessed by in situ x-ray emission spectroscopy. *Angew. Chem. Int. Ed.* **60**, 11707–11712 (2021).

61. C. Liu, Y. Wu, K. Sun, J. Fang, A. Huang, Y. Pan, W.-C. Cheong, Z. Zhuang, Z. Zhuang, Q. Yuan, H. L. Xin, C. Zhang, J. Zhang, H. Xiao, C. Chen, Y. Li, Constructing FeN_4/graphitic nitrogen atomic interface for high-efficiency electrochemical CO_2 reduction over a broad potential window. *Chem* **7**, 1297–1307 (2021).

62. J. Chen, Y. Z. Finfrock, Z. Wang, T. K. Sham, Strain and ligand effects in Pt-Ni alloys studied by valence-to-core X-ray emission spectroscopy. *Sci Rep-Uk* **11**, 13698 (2021).

63. L. Chong, J. Wen, J. Kubal, F. G. Sen, J. Zou, J. Greeley, M. Chan, H. Barkholtz, W. Ding, D. J. Liu, Ultralow-loading platinum-cobalt fuel cell catalysts derived from imidazolate frameworks. *Science* **362**, 1276–1281 (2018).

64. B. Ravel, M. Newville, ATHENA, ARTEMIS, HEPHAESTUS: Data analysis for X-ray absorption spectroscopy using IFEFFIT. *J. Synchrotron Radiat.* **12**, 537–541 (2005).

65. G. Kresse, J. Furthmuller, Efficiency of ab-initio total energy calculations for metals and semiconductors using a plane-wave basis set. *Comp. Mater. Sci.* **6**, 15–50 (1996).

66. G. Kresse, J. Furthmuller, Efficient iterative schemes forab initiototal-energy calculations using a plane-wave basis set. *Phys. Rev. B* **54**, 11169–11186 (1996).

67. J. P. Perdew, K. Burke, M. Ernzerhof, Generalized gradient approximation made simple. *Phys. Rev. Lett.* **77**, 3865–3868 (1996).

68. H. J. Monkhorst, J. D. Pack, Special points for Brillouin-zone integrations. *Phys. Rev. B* **13**, 5188–5192 (1976).

69. P. E. Blochl, Projector augmented-wave method. *Phys. Rev., B Condens. Matter.* **50**, 17953–17979 (1994).

70. S. Grimme, J. Antony, S. Ehrlich, H. Krieg, A consistent and accurate ab initio parametrization of density functional dispersion correction (DFT-D) for the 94 elements H-Pu. *J. Chem. Phys.* **132**, 154104 (2010).

71. H. Guo, Z. Fang, H. Li, D. Fernandez, G. Henkelman, S. M. Humphrey, G. Yu, Rational design of rhodium-iridium alloy nanoparticles as highly active catalysts for acidic oxygen evolution. *ACS Nano* **13**, 13225–13234 (2019).

72. G. Meng, W. Sun, A. A. Mon, X. Wu, L. Xia, A. Han, Y. Wang, Z. Zhuang, J. Liu, D. Wang, Y. Li, Strain regulation to optimize the acidic water oxidation performance of atomic-layer IrO_x. *Adv. Mater.* **31**, e1903616 (2019).

73. F.-F. Zhang, C.-Q. Cheng, J.-Q. Wang, L. Shang, Y. Feng, Y. Zhang, J. Mao, Q.-J. Guo, Y.-M. Xie, C.-K. Dong, Y.-H. Cheng, H. Liu, X.-W. Du, Iridium oxide modified with silver single atom for boosting oxygen evolution reaction in acidic media. *ACS Energy Lett.* **6**, 1588–1595 (2021).

74. F. Luo, H. Hu, X. Zhao, Z. Yang, Q. Zhang, J. Xu, T. Kaneko, Y. Yoshida, C. Zhu, W. Cai, Robust and stable acidic overall water splitting on Ir single atoms. *Nano Lett.* **20**, 2120–2128 (2020).

75. O. Diaz-Morales, S. Raaijman, R. Kortlever, P. J. Kooyman, T. Wezendonk, J. Gascon, W. T. Fu, M. T. Koper, Iridium-based double perovskites for efficient water oxidation in acid media. *Nat. Commun.* **7**, 12363 (2016).

76. S. Kumari, B. P. Ajayi, B. Kumar, J. B. Jasinski, M. K. Sunkara, J. M. Spurgeon, A low-noble-metal $W_{1-x}Ir_xO_{3-\delta}$ water oxidation electrocatalyst for acidic media via rapid plasma synthesis. *Energ. Environ. Sci.* **10**, 2432–2440 (2017).

77. Y. Pi, N. Zhang, S. Guo, J. Guo, X. Huang, Ultrathin laminar Ir superstructure as highly efficient oxygen evolution electrocatalyst in broad pH range. *Nano Lett.* **16**, 4424–4430 (2016).

78. Y. Zhao, M. Luo, S. Chu, M. Peng, B. Liu, Q. Wu, P. Liu, F. M. F. de Groot, Y. Tan, 3D nanoporous iridium-based alloy microwires for efficient oxygen evolution in acidic media. *Nano Energy* **59**, 146–153 (2019).

79. J. Lim, D. Park, S. S. Jeon, C. W. Roh, J. Choi, D. Yoon, M. Park, H. Jung, H. Lee, Ultrathin IrO_2 nanoneedles for electrochemical water oxidation. *Adv. Funct. Mater.* **28**, 1704796 (2018).

80. J. Park, Y. J. Sa, H. Baik, T. Kwon, S. H. Joo, K. Lee, Iridium-based multimetallic nanoframe@nanoframe structure: An efficient and robust electrocatalyst toward oxygen evolution reaction. *ACS Nano* **11**, 5500–5509 (2017).

81. L. Yang, G. Yu, X. Ai, W. Yan, H. Duan, W. Chen, X. Li, T. Wang, C. Zhang, X. Huang, J. S. Chen, X. Zou, Efficient oxygen evolution electrocatalysis in acid by a perovskite with face-sharing IrO_6 octahedral dimers. *Nat. Commun.* **9**, 5236 (2018).

82. Q. Feng, J. Zou, Y. Wang, Z. Zhao, M. C. Williams, H. Li, H. Wang, Influence of surface oxygen vacancies and ruthenium valence state on the catalysis of pyrochlore oxides. *ACS Appl. Mater. Interfaces* **12**, 4520–4530 (2020).

83. L. Wang, V. A. Saveleva, S. Zafeiratos, E. R. Savinova, P. Lettenmeier, P. Gazdzicki, A. S. Gago, K. A. Friedrich, Highly active anode electrocatalysts derived from electrochemical leaching of Ru from metallic $_{Ir\ 0.7\ Ru\ 0.3}$ for proton exchange membrane electrolyzers. *Nano Energy* **34**, 385–391 (2017).

84. W. Xu, K. Scott, The effects of ionomer content on PEM water electrolyser membrane electrode assembly performance. *Int. J. Hydrogen Energy* **35**, 12029–12037 (2010).

85. G. Jiang, H. Yu, J. Hao, J. Chi, Z. Fan, D. Yao, B. Qin, Z. Shao, An effective oxygen electrode based on $Ir_{0.6}Sn_{0.4}O_2$ for PEM water electrolyzers. *J. Energy Chem.* **39**, 23–28 (2019).

86. A. Marshall, B. Børresen, G. Hagen, M. Tsypkin, R. Tunold, Electrochemical characterisation of $Ir_xSn_{1-x}O_2$ powders as oxygen evolution electrocatalysts. *Electrochim. Acta* **51**, 3161–3167 (2006).

87. J. Cheng, H. Zhang, G. Chen, Y. Zhang, Study of $Ir_xRu_{1-x}O_2$ oxides as anodic electrocatalysts for solid polymer electrolyte water electrolysis. *Electrochim. Acta* **54**, 6250–6256 (2009).

88. C. Xu, L. Ma, J. Li, W. Zhao, Z. Gan, Synthesis and characterization of novel high-performance composite electrocatalysts for the oxygen evolution in solid polymer electrolyte (SPE) water electrolysis. *Int. J. Hydrogen Energy* **37**, 2985–2992 (2012).

89. E. Rasten, G. Hagen, R. Tunold, Electrocatalysis in water electrolysis with solid polymer electrolyte. *Electrochim. Acta* **48**, 3945–3952 (2003).